DEVELOPMENT OF A MARKER-BASED DISPLACEMENT TRACKING TECHNIQUE FOR TENSILE TESTING OF GEOSYNTHETICS USING COMPUTER VISION

A THESIS SUBMITTED TO
THE GRADUATE SCHOOL OF NATURAL AND APPLIED SCIENCES
OF
MIDDLE EAST TECHNICAL UNIVERSITY

BY

MEHMET TÜRKEZER

IN PARTIAL FULFILLMENT OF THE REQUIREMENTS
FOR
THE DEGREE OF MASTER OF SCIENCE
IN
CIVIL ENGINEERING

JULY 2023

Approval of the thesis:

DEVELOPMENT OF A MARKER-BASED DISPLACEMENT TRACKING TECHNIQUE FOR TENSILE TESTING OF GEOSYNTHETICS USING COMPUTER VISION

submitted by **MEHMET TÜRKEZER** in partial fulfillment of the requirements for the degree of **Master of Science** i**n Civil Engineering, Middle East Technical University** by,

Prof. Dr. Halil Kalıpçılar
Dean, Graduate School of **Natural and Applied Sciences** _____

Prof. Dr. Erdem Canbay
Head of the Department, **Civil Engineering** _____

Assoc. Prof. Dr. Onur Pekcan
Supervisor, **Civil Engineering, METU** _____

Examining Committee Members:

Prof. Dr. Bahadır Sadık Bakır
Civil Engineering Dept., METU _____

Assoc. Prof. Dr. Onur Pekcan
Civil Engineering Dept., METU _____

Prof. Dr. Erdal Çokça
Civil Engineering Dept., METU _____

Prof. Dr. Sinan Kalkan
Computer Engineering Dept., METU _____

Assist. Prof. Dr. Seda Selçuk
Civil Engineering Dept., Çankaya University _____

Date: 05.07.2023

I hereby declare that all information in this document has been obtained and presented in accordance with academic rules and ethical conduct. I also declare that, as required by these rules and conduct, I have fully cited and referenced all material and results that are not original to this work.

Name Last name : Mehmet, Türkezer

Signature :

ABSTRACT

DEVELOPMENT OF A MARKER-BASED DISPLACEMENT TRACKING TECHNIQUE FOR TENSILE TESTING OF GEOSYNTHETICS USING COMPUTER VISION

Türkezer, Mehmet
Master of Science, Civil Engineering
Supervisor : Assoc. Prof. Dr. Onur Pekcan

July 2023, 131 pages

Geosynthetics are the manufactured products generally used within soils to improve their weak characteristics. Before using geosynthetics in the field, their tensile strength and deformation characteristics (i.e., strain capacity) should be tested in laboratory conditions. For this purpose, as part of tensile testing, various types of extensometers are used to measure the deformations accurately, which are generally expensive and take time to implement during testing. Therefore, there is a need to use new technologies, such as imaging, to replace extensometers to ease and accelerate testing without losing accuracy. In this sense, computer vision facilitates the quantification of strains based on markers drawn on specimens. This study presents a non-contact strain measurement technique called "Marker-Based Displacement Tracking (MBDT)" developed using Python programming, incorporating OpenCV, an open-source vision-based code platform. Markers designating a gauge length are drawn on specimens and identified using image segmentation techniques. The accuracy of MBDT is validated by comparing the strains calculated by Crosshead Displacement and Digital Image Correlation techniques on geomembrane, geotextile, and geosynthetic clay liner samples, tested by different Universal Testing Machines and conventional video cameras. The feasibility of using a camera with an ultra-wide-angle (fisheye) lens as the capturing

device is also assessed. The results obtained with 36 experiments proved the success of MBDT, implying its application to various other types of geosynthetics.

Keywords: Geosynthetics, Tensile Testing, Strain Measurement, Video Extensometer, Digital Image Correlation.

ÖZ

BİLGİSAYAR GÖRÜSÜ KULLANARAK GEOSENTETİKLERİN ÇEKME TESTİ İÇİN İŞARETÇİ TABANLI DEPLASMAN TAKİP YÖNTEMİNİN GELİŞTİRİLMESİ

Türkezer, Mehmet
Yüksek Lisans, İnşaat Mühendisliği
Tez Yöneticisi: Doç. Dr. Onur Pekcan

Temmuz 2023, 131 sayfa

Geosentetikler, zemin özelliklerini çeşitli yönlerden iyileştirmek amacı ile kullanılan ürünlerdir. Geosentetikler sahada kullanılmadan önce, yeterli çekme mukavemeti ve çekme altında gerinim kapasitelerine sahip oldukları test edilmelidir. Bu amaçla, çekme testinin bir parçası olarak, deformasyonları doğru bir şekilde ölçmek için genellikle test sırasında uygulanması zaman alabilen çeşitli ekstansometre türleri kullanılır. Doğruluktan ödün vermeden, bu süreci kolaylaştırmak ve hızlandırmak için ekstansometrelerin yerini alacak yeni teknolojilerin kullanılmasına ihtiyaç vardır. Bilgisayar görüsü bazlı çalışan teknikler, numuneler üzerine çizilen işaretçilerin takip edilmesi yolu ile numune üzerindeki uzamaların görsel olarak ölçülmesini sağlar. Bu tez kapsamında, OpenCV görüntü işleme kütüphanesi kullanılarak Python dilinde geliştirilen "İşaretçi Bazlı Deplasman İzleme (MBDT)" olarak adlandırılan temassız bir gerinim ölçüm tekniği sunulmaktadır. Yöntem, numune üzerine çizilen işaretçilerin görüntü işleme teknikleri kullanılarak algılanması ve bir test esnasında uzamaların sürekli olarak izlenmesine dayanmaktadır. Önerilen yöntemin doğruluğu, farklı Üniversal Test Makineleri (UTM) ve geleneksel video kameralar ile test edilen geomembran, geotekstil ve geosentetik kil örtü numuneleri üzerinde UTM hareketi ve Dijital Görüntü

Korelasyonu yöntemleri kullanılarak araştırılmıştır. Geniş açılı lense sahip bir kameranın laboratuvarda kullanımının fizibilitesi de çalışma kapsamında araştırılmıştır. Gerçekleştirilen 36 deneyde elde edilen sonuçlar, MBDT'nin başarısını kanıtlayarak diğer geosentetik türlerinde uygulanmasının yolunu açmıştır.

Anahtar Kelimeler: Geosentetikler, Çekme Testleri, Gerinim Ölçümü, Video Ekstansometre, Dijital Görüntü Korelasyonu.

Dedicated to My Family

ACKNOWLEDGMENTS

I am deeply grateful to Dr. Onur Pekcan, who introduced me to geotechnical engineering with enthusiasm and passion. His guidance and mentoring were beyond being an academician; more like an inspiring leader. I am indebted for his friendship, encouragement, and endless support. I loved learning to be different and innovative from him. It is a great privilege to have studied under his supervision. I am truly honored and privileged to have had the opportunity to work under his guidance. I would like to express my most profound appreciation for his time, patience, and insightful recommendations during the thesis writing process.

I extend my sincerest appreciation to the thesis jury professors, Dr. Bahadır Sadık Bakır, Dr. Erdal Çokça, Dr. Sinan Kalkan, and Dr. Seda Selçuk for their comments, feedback, and contributions to the study.

I am immensely grateful to professors Dr. Kemal Önder Çetin, Dr. N. Kartal Toker, Dr. Nejan Huvaj Sarıhan, Dr. Mahmut Yavuz Şengör, and Dr. Serdar Göktepe for the invaluable lectures and exceptional instructions and guidance in my graduate courses. Their expertise, engaging teaching style, and commitment to fostering critical thinking have challenged me to expand my knowledge and skills. Their encouragement and constructive feedback have played a vital role in my academic growth.

I would like to extend my thanks to my colleagues at the soil mechanics laboratory, Elife Çakır, Berkan Söylemez, Arda Şahin, Eray Caceoğlu, Satuk Buğrahan Sari, Hayri Güzel, Tuğçe Aktaş Engin, Sefa Yıldırım, Dr. Gizem Can, and Dr. Makbule Ilgaç for their invaluable friendship, mentorship, and encouragement during my studies. The collaborative and supportive environment we shared has been instrumental in shaping my academic and professional journey. I am also grateful to Yiğit Urhan who has been an outstanding friend and motivator and whose helpful criticism has made my study incalculably better. I would also like to thank Ulaş

Nacar and Kamber Bilgen for their expertise, support, and guidance during my graduate studies at the soil mechanics laboratory.

I owe further thanks to our research group, AI2LAB, members; Murat Altun, Yılmaz Emre Sarıçiçek, Emre Duman, Ahmet Bahaddin Ersöz, Türker Teke and Yağızer Yalçın, Ediz Karaali, and Furkan Aydoğan for providing me with the motivation and knowledge I needed during my studies. Our research group's innovative, interdisciplinary, kind, and helpful nature has shaped my research journey, and I am truly grateful to each member. I truly appreciate the help of Tanner Wambui Muturi for helping me with thesis writing, making invaluable recommendations, and reviewing my thesis. Moreover, I express my special thanks to Serhat Erinmez and Fikri Çağlar Gökdemir, who helped me with the experiments conducted in this study. Conducting the experiments would not be possible without the help of Fikri Çağlar Gökdemir, whose enthusiasm, friendship, and guidance are greatly appreciated.

I also greatly appreciate the financial support provided by The Scientific and Technological Research Council of Turkey (TÜBİTAK) in the scope of the National Master of Science Education Scholarship (2210-A).

I would like to acknowledge my family for their unconditional and endless support since I was born. I dedicate this work to my mother, Feray Türkezer; my father, Ali Türkezer; and my brother Egemen Türkezer, for their endless faith in me, which has given me the strength and courage to pursue my passions and embrace new challenges.

Finally, I want to dedicate a heartfelt expression of gratitude to my beloved wife, Ecem Çalı Türkezer, for her unwavering love, support, encouragement, and unconditional faith in me. Her understanding and flexibility have allowed me to fully immerse myself in my studies, knowing her support was always there. With all my love and appreciation, thank you for always being there for me.

TABLE OF CONTENTS

ABSTRACT v

ÖZ vii

ACKNOWLEDGMENTS x

TABLE OF CONTENTS xii

LIST OF TABLES xv

LIST OF FIGURES xvi

LIST OF ABBREVIATIONS xxiv

LIST OF SYMBOLS xxvi

CHAPTERS

1 INTRODUCTION 1

1.1 Overview 1

1.1.1 Tensile Deformations of Geosynthetics 4

1.1.2 Computer Vision 5

1.1.2.1 Software Development for the Geotechnical Laboratory 6

1.2 Aim of the Study 7

1.3 Research Questions 7

1.4 Scope and Method 7

1.5 Organization of the Thesis 8

2 LITERATURE REVIEW 9

2.1 Introduction 9

2.2 Strain Measurement in Tensile Testing 10

2.2.1 Image-Based Strain Measurement in Tensile Testing 13

2.3 Applications of Computer Vision in Geotechnical Testing 21
2.3.1 Open-Source Software Development in Geotechnical Engineering. 26
2.4 Summary 29
3 STRAIN MEASUREMENT USING COMPUTER VISION 31
3.1 Specimen Preparation..... 32
3.2 Capturing Images 35
3.2.1 Lens Distortions 36
3.3 Camera Calibration 38
3.4 Calculation of Strains by Image Segmentation: Marker-Based Displacement Tracking (MBDT) Technique 40
3.4.1 Overview..... 41
3.4.2 Program Flow..... 42
3.4.3 Color Thresholding 44
3.4.4 Edge Detection..... 49
3.4.5 Analysis of Contours..... 51
3.4.6 Calculation of Strains..... 55
3.5 Strain Measurement by Digital Image Correlation (DIC)..... 57
4 GEOSYNTHETIC TESTS WITH MBDT 63
4.1 Tensile Testing Setup 63
4.1.1 Universal Testing Machine (UTM)..... 63
4.1.2 Camera 65
4.1.3 Auxiliary Equipment..... 66
4.2 Validation of MBDT 68
4.2.1 Validation of Strains 69

4.2.1.1 Testing of Geomembranes 70
4.2.1.2 Testing of Geotextiles 79
4.2.1.3 Testing of Geosynthetic Clay Liners (GCL) 93
4.2.2 Validation of Camera Calibration 102
4.2.2.1 Normal Lens Calibration 103
4.2.2.2 Fisheye Lens Calibration 107
4.2.2.3 Concluding Remarks on Calibration 111
5 SUMMARY, RESULTS, CONCLUSIONS, AND FUTURE WORK 113
5.1 Summary 113
5.2 Results Overview 115
5.2.1 Geomembrane Tests 115
5.2.2 Geotextile Tests 116
5.2.3 GCL Tests 118
5.3 Conclusions 119
5.4 Future Work 121
REFERENCES 123
APPENDICES 129
A. Geomembrane Tests 129
B. Geotextile Tests 130
C. GCL Tests 131

LIST OF TABLES

TABLES

Table 2.1. Strain measurement techniques recommended by widely used tensile test standards. 12
Table 4.1. Key technical properties of the Universal Testing Machines. 64
Table 4.2. Key technical properties of the cameras used in this study. 65
Table 4.3. Summary of validation test plan, with equipment, materials, and validation techniques. 68
Table 4.4. Key physical and mechanical properties of the geomembrane samples. Technical specification limit values are indicated in square brackets. 71
Table 4.5. Geotextile mass per unit area and implemented test speeds. 79
Table 4.6. Key physical and mechanical properties of the geotextile samples. Technical specification limit values are indicated in square brackets. 81
Table 4.7. Key physical and mechanical properties of the GCL samples. Technical specification limit values are indicated in square brackets. 94

LIST OF FIGURES

FIGURES

Figure 1.1. A typical cross-section of an engineered waste landfill (Ikehata & Liu, 2011). 2
Figure 1.2. The funnel of the research plan. 4
Figure 2.1. Examples of strain measurement devices used for testing of geosynthetics. (a) Foil strain gauge. (b) Clip-on extensometer. (c) Roller extensometer. (d) Video extensometer (ASTM D4595, 2017). 11
Figure 2.2. Distribution of (a) computer vision techniques, (b) material types, (c) image acquisition devices among a set of reviewed papers on computer vision-based mechanical testing (Baldner et al., 2020). 14
Figure 2.3. (a) A capstan grip clamps a geotextile specimen. (b) The damage caused on by the attachment of contact extensometers causes the filaments in the machine direction to prematurely break (Jones, 2000). 15
Figure 2.4. (a) A clip-on extensometer and a strain gauge are attached to a geotextile specimen and clamped by testing grips. (b) Visible holes after the extensometer is attached (Aydilek et al., 2004). 16
Figure 2.5. (a) Change of the speckle pattern from the undeformed to the deformed shape. (b) The color map showing the vertical strain distribution on a specimen, as the result of DIC (Parsons et al., 2004), (c) Image correlation process by GeoPIV-RG is explained (Stanier et al., 2015). 17
Figure 2.6. A laser extensometer is used for the tensile testing of cement-based composites. (a) Schematic drawing of the experiment setup. (b) Laser beams mark the gauge length (Zhu et al., 2012). 19
Figure 2.7. In R, an image-based technique is created and used to measure the tensile strains of geotextiles. (a) The stress-strain graph is created using the suggested technique and the crosshead displacements. By using a heatmap, strains are shown. (b) Before testing, a dot grid is drawn on the geotextile sample (Poggiogalle et al., 2022). 20

Figure 2.8. The enlarged pore sizes of a geotextile specimen which is kept under tension. (a) The grayscale image. (b) The binary mask after being processed with morphological operations (Tang et al., 2013) 22
Figure 2.9. Strain distribution during a triaxial test, obtained by the optical flow algorithm (Uy & Boonyatee, 2016). 23
Figure 2.10. Two cameras are utilized for the deformation tracking methodology for the transparent soil reinforced with geogrids. (a) A schematic diagram of the test setup. (b) The correlation area on the transparent sand is formed by the refraction of laser beams from the grains (Peng & Zornberg, 2019). 24
Figure 2.11. (a) A speckle pattern is applied to the geogrid specimen (Ferreira & Zornberg, 2015). (b) The geogrid specimen inside the transparent sand is shown after the pore fluid is inserted (Peng & Zornberg, 2019). 24
Figure 2.12. (a) Grayscale image of the stabilized transparent sand. (b) The segmented image. (c) Grain probabilities are indicated by color densities, with edges of the actual grains (Marx et al., 2022). 25
Figure 2.13. Measurement of shear strains on an experimental study on slopes. (a) Four Raspberry Pi cameras are employed to capture the failure progressing on the slope. (b) DIC is utilized for the quantification of shear strains (Eichhorn et al., 2020). 26
Figure 2.14. The user interface of the soil deformation measurement software developed in C++ (Zhao et al., 2013). 27
Figure 2.15. Soil classification platform developed by Madrigal et al. (2021). 28
Figure 3.1. Preparation of test specimens. (a) Geomembrane with two color markers. (b) Geomembrane with multi group color markers and speckle pattern. (c) Geotextile with a single pair of color markers. (d) The same geotextile with a speckle pattern added. The color markers designate a predefined gauge length on all specimens.. 33
Figure 3.2. Speckle pattern application trials resulted in unsuccessful correlations. (a) Ink is applied on a spray-painted body, resulting in spalling of paint and unidentifiable speckles. (b) Correlation cannot be established due to few speckles. 35

Figure 3.3. A normal image frame and two types of radial distortions. 36
Figure 3.4. (a) Schematic view of the lens configuration that causes tangential distortion due to manufacturing errors (Bradski & Kaehler, 2008). (b) An example of the tangential distortion illustrated on an image frame. 37
Figure 3.5. A schematic representation of a fisheye lens configuration. Multiple lenses are used in combination (The MathWorks Inc., 2023). 37
Figure 3.6. Summary of the OpenCV camera calibration routine, with inputs and outputs. 38
Figure 3.7. Main Program Flow. 43
Figure 3.8. Schematic plots of (a) RGB, (b) HSV color models (Bradski, 2000)... 44
Figure 3.9. HSV color thresholding for the geotextile specimen. For avoiding light reflections from polished surfaces, the wedge grips are covered with matte black color, and a black cardboard is placed on the background. (a) Original RGB image. (b) The image is converted from RGB to HSV. (c) The masked image after setting the color threshold limits. 47
Figure 3.10. Color thresholding resulted in incomplete masking of color markers. A noisy image was obtained due to reflections of marker colors from the shiny surface of the wedge grips. (a) Original RGB image. (b) HSV image. (c) The masked image after the threshold limits are set. 48
Figure 3.11. Step-by-step color marker detection by image segmentation. (a) Original RGB image. (b) RGB is converted to HSV. (c) A binary mask is obtained after setting the color threshold limits. (d) Masked image, blurred to some extent. (e) Edges of the markers detected by the Canny algorithm. (f) Successfully detected markers shown on the original image by bounding boxes and their coordinates in pixels. 51
Figure 3.12. Flowchart of the Contour Analysis module. 54
Figure 3.13. (a) Users are prompted to draw a box to indicate the gauge length. (b) Marker location limits on the x-axis and the minimum marker size are set by drawing another bounding box. 56
Figure 3.14. The program flow of Ncorr software (Blaber & Antoniou, 2017)..... 58

Figure 3.15. Adjustment of DIC analysis parameters using Ncorr software. 58
Figure 3.16. Miscellaneous steps of the DIC analysis. (a) Location of seeds. (b) Fitting a plane to displacements for strain calculation..... 60
Figure 3.17. DIC analysis results of a geomembrane sample prior to yielding. (a) Displacements (mm). (b) Lagrangian-Green strains. (c) Eulerian-Almansi strains. 62
Figure 4.1. Universal Testing Machines used in this study. (a) Zwick Roell Z010, with pneumatic grips. (b) Pekon MTM-ProV10, with mechanical wedge grips. ... 64
Figure 4.2. Auxiliary equipment used in the test setup. (a) LED light sources behind the grips to provide sufficient illumination. (b) Black cardboard on the background to avoid noise in the images. 67
Figure 4.3. (a) GMB - Type 1 test sample with color markers designating the gauge lengths (L_0 = 33 mm and 50 mm) and speckles drawn for the DIC technique. (b) The pneumatic grips are testing the sample. A black cardboard is placed in the background to avoid undesired noise appearing in the scene. 72
Figure 4.4. Different image-based techniques are in use for the geomembrane sample (T-GMB_1). (a) DIC, displacement distribution heat map (mm). (b) DIC, strain distribution heat map (Lagrangian-Green). (c) MBDT..... 73
Figure 4.5. For each test, strains by MBDT are compared with DIC and Crosshead Displacement techniques. MAE and RMSE are calculated. 74
Figure 4.6. Strain – Time graphs for the tests (a) T-GMB_1, (b) T-GMB_2, (c) T-GMB_3. HDPE geomembrane samples are 1.5-mm-thick and smooth. The samples are cut in the machine direction. The test speed is set to 50 mm/min. 76
Figure 4.7. Strain – Time graphs for the tests (a) T-GMB_4, (b) T-GMB_5, (c) T-GMB_6. HDPE geomembrane samples are 1.5-mm-thick and smooth. The samples are cut in the cross-machine direction. The test speed is set to 50 mm/min. 76
Figure 4.8. Strain – Time graphs for the tests (a) T-GMB_7, (b) T-GMB_8, (c) T-GMB_9. HDPE geomembrane samples are 1.5-mm-thick and one-sided textured. The samples are cut in the machine direction. The test speed is set to 50 mm/min. 77

Figure 4.9. Strain – Time graphs for the tests (a) T-GMB_10, (b) T-GMB_11, (c) T-GMB_12. HDPE geomembrane samples are 1.5-mm-thick and one-sided textured. The samples are cut in the cross-machine direction. The test speed is set to 50 mm/min.....77
Figure 4.10. Strain distribution comparison of (a) 1.5-mm smooth, (b) 1.5-mm one-sided textured geomembrane at yielding, produced by DIC. 78
Figure 4.11. (a) Test sample with color markers designating the gauge length (L_0 = 60 mm) and speckles drawn for the DIC technique. (b) A mechanical wedge grip is testing the sample. The grips are covered with black cardboard to prevent any reflections of light.....82
Figure 4.12. Different image-based methods are in use for the geotextile sample (T-GTX_1). (a) DIC, displacement distribution heat map (mm). (b) DIC, strain distribution heat map (Lagrangian-Green). (c) MBDT, identification of color markers. 84
Figure 4.13. For each test, strains by MBDT are compared with DIC, DIC-Displacement Derived (L_0 = 60mm), and Crosshead Displacement techniques (L_0=100 mm). MAE and RMSE are calculated.....85
Figure 4.14. Strain – Time graphs for the tests (a) T-GTX_1, (b) T-GTX_2, (c) T-GTX_3. Geotextile samples have a mass per unit area of 400 g/m^2. The test speed is set to 10 mm/min. 87
Figure 4.15. Strain – Time graphs for the tests (a) T-GTX_4, (b) T-GTX_5, (c) T-GTX_6. Geotextile samples have a mass per unit area of 400 g/m^2. The test speed is set to 20 mm/min. 87
Figure 4.16. Load – Strain graphs for the tests (a) T-GTX_1, (b) T-GTX_2, (c) T-GTX_3. Geotextile samples have a mass per unit area of 400 g/m^2. The test speed is set to 10 mm/min. 88
Figure 4.17. Load – Strain graphs for the tests (a) T-GTX_4, (b) T-GTX_5, (c) T-GTX_6. Geotextile samples have a mass per unit area of 400 g/m^2. The test speed is set to 20 mm/min. 88

Figure 4.18. Strain – Time graphs for the tests (a) T-GTX_4, (b) T-GTX_5, (c) T-GTX_6. Geotextile samples have a mass per unit area of 400 g/m^2. The test speed is set to 20 mm/min. 90
Figure 4.19. Strain – Time graphs for the tests (a) T-GTX_7, (b) T-GTX_8, (c) T-GTX_9. Geotextile samples have a mass per unit area of 600 g/m^2. The test speed is set to 20 mm/min. 90
Figure 4.20. Strain – Time graphs for the tests (a) T-GTX_10, (b) T-GTX_11, (c) T-GTX_12. Geotextile samples have a mass per unit area of 300 g/m^2. The test speed is set to 20 mm/min. 91
Figure 4.21. Load – Strain graphs for the tests (a) T-GTX_4, (b) T-GTX_5, (c) T-GTX_6. Geotextile samples have a mass per unit area of 400 g/m^2. The test speed is set to 20 mm/min. 91
Figure 4.22. Load – Strain graphs for the tests (a) T-GTX_7, (b) T-GTX_8, (c) T-GTX_9. Geotextile samples have a mass per unit area of 600 g/m^2. The test speed is set to 20 mm/min. 92
Figure 4.23. Load – Strain graphs for the tests (a) T-GTX_10, (b) T-GTX_11, (c) T-GTX_12. Geotextile samples have a mass per unit area of 300 g/m^2. The test speed is set to 20 mm/min. 92
Figure 4.24. (a) GCL test sample with color markers designating the gauge length (L_0 = 60 mm) and speckles drawn for the DIC technique. (b) A mechanical wedge grip is testing the sample. The grips are covered with black cardboard to prevent any undesired reflections of light. 94
Figure 4.25. Different image-based methods are in use for the GCL sample (T-GCL_1). (a) DIC, displacement distribution heat map (mm). (b) DIC, strain distribution heat map (Lagrangian strains). (c) MBDT, identification of color markers. 96
Figure 4.26. For each test, strains by MBDT are compared with DIC, DIC-Displacement Derived (L_0 = 60mm), and Crosshead Displacement techniques (L_0=100 mm). MAE and RMSE are calculated. 97

Figure 4.27. Strain – Time graphs for the tests (a) T-GCL_1, (b) T-GCL_3, (c) T-GCL_4. The samples are cut in cross-machine direction. The test speed is set to 20 mm/min.....98
Figure 4.28. Strain – Time graphs for the tests (a) T-GCL_2, (b) T-GCL_5, (c) T-GCL_6. The samples are cut in the machine direction. The test speed is set to 20 mm/min.....99
Figure 4.29. Strain – Time graphs for the tests (a) T-GCL_7, (b) T-GCL_8, (c) T-GCL_9, (d) T-GCL_10. The samples are cut in the cross-machine direction. The test speed is set to 10 mm/min. 99
Figure 4.30. Strain – Time graphs for the tests (a) T-GCL_11, (b) T-GCL_12. The samples are cut in the machine direction. The test speed is set to 10 mm/min. 100
Figure 4.31. Load – Strain graphs for the tests (a) T-GCL_1, (b) T-GCL_3, (c) T-GCL_4. The samples are cut in the cross-machine direction. The test speed is set to 20 mm/min.....100
Figure 4.32. Load – Strain graphs for the tests (a) T-GCL_2, (b) T-GCL_5, (c) T-GCL_6. The samples are cut in the machine direction. The test speed is set to 20 mm/min.....101
Figure 4.33. Load – Strain graphs for the tests (a) T-GCL_7, (b) T-GCL_8, (c) T-GCL_9, (d) T-GCL_10. The samples are cut in the cross-machine direction. The test speed is set to 10 mm/min. 101
Figure 4.34. Load – Strain graphs for the tests (a) T-GCL_11, (b) T-GCL_12. The samples are cut in the machine direction. The test speed is set to 10 mm/min. 102
Figure 4.35. Calibration images taken by Nikon D5100 equipped with an 18-35mm normal lens (Cam-2).....104
Figure 4.36. Camera calibration results for Cam-2, generated by MATLAB Camera Calibrator App. (a) Schematic plot showing the calibration board locations for each calibration image in real-world units. (b) Mean reprojection error graph.....105
Figure 4.37. Calibration images taken by GoPro Hero 4 Session (Cam-1). 107
Figure 4.38. Images showing before and after calibration. (a) Automatic detection of the checkerboard pattern by OpenCV. (b) Corrected image produced by OpenCV.

(c) Automatic detection of the checkerboard pattern by MATLAB. (d) Corrected image by MATLAB. While the OpenCV image is cropped, MATLAB image is left uncropped. 108
Figure 4.39. Camera calibration results of Cam-1 by MATLAB Camera Calibrator App. (a) Schematic plot showing the calibration board locations for each calibration image in real-world units. (b) Mean reprojection error graph. 109
Figure 6.1. Load - Crosshead Displacement plot of the geomembrane tests. 129
Figure 6.2. Crosshead Displacement - Time plot of the geomembrane tests. 129
Figure 6.3. Load - Crosshead Displacement plot of the geotextile tests. 130
Figure 6.4. Crosshead Displacement - Time plot of the geotextile tests. 130
Figure 6.5. Load - Crosshead Displacement plot of the GCL tests. 131
Figure 6.6. Crosshead Displacement - Time plot of the GCL tests. 131

LIST OF ABBREVIATIONS

ABBREVIATIONS

CCD: Charge Coupled Device

CMD: Cross Machine Direction

CMYK: Cyan-Magenta-Yellow-Black

DIC: Digital Image Correlation

DSLR: Digital Single-Lens Reflex

FOS: Free and Open Source

GCL: Geosynthetic Clay Liner

GMB: Geomembrane

GTX: Geotextile

GUI: Graphical User Interface

HDPE: High-Density Polyethylene

HSV: Hue-Saturation-Value

LVDT: Linear Variable Differential Transformer

MAE: Mean Absolute Error

MD: Machine Direction

MBDT: Marker-Based Displacement Tracking

PIV: Particle Image Velocimetry

RGB: Red-Green-Blue

RMSE: Root Mean Square Error

SEM: Scanning Electron Microscope

UTM: Universal Testing Machine

LIST OF SYMBOLS

SYMBOLS

ε: Strain

ε_y: Yield Strain

ε_t: Rupture Strain

ϕ: Millimeters-to-Pixels Ratio

ΔL_{CT}: Crosshead Travel Distance

ΔL: Elongation in the Gauge Length

L_0: Initial Gauge Length

L_i: Instantaneous Gauge Length

CHAPTER 1

INTRODUCTION

1.1 Overview

Geosynthetics are manufactured products generally used within soils to enhance their insufficient engineering properties. While "geo" implies their use within soils, "synthetic" indicates manufactured production instead of natural materials. Geotextiles, geogrids, geomembranes, geocells, geosynthetic clay liners, geocomposites, geonets, geofoams, and geopipes can be listed as the main categories of geosynthetics. Raw geosynthetic materials are generally the same as those used in the plastics industry, such as polyester, polyethylene, polypropylene, and polyvinyl chloride (Koerner, 2005). At first, geosynthetics were used as fibrous materials in soil stabilization. Later, they were used in building materials. In addition to reinforcement adoption, application areas include stabilizing soft soils, preventing erosion, providing drainage, and reducing the diffusion of contaminants. Beyond traditional application areas such as foundations, retaining walls, and pavements, they are also commonly used in landfills, lagoons for contaminated fluids, dams, and mining applications such as tailings storage facilities and heap leach pads (Rowe, 2020). While most prevalent in geo-environmental and geotechnical applications, they have a broader usage area in the waterproofing of buildings, and their importance in engineering is ever-growing (Müller & Saathoff, 2015).

In geo-environmental applications, geomembranes, geosynthetic clay liners (GCL), and geotextiles are commonly used as essential components in most landfills. These components minimize the transport of contaminants to groundwater by acting as a barrier system. As can be seen in Figure 1.1, which depicts a typical cross-section of

an engineered landfill, geomembranes are used on the side slopes, at the bottom, and as a cover over the waste layers. A low permeability barrier system is formed with the compacted clay liner or a layer of GCL. The geotextile separates the barrier and the highly permeable leachate collection system and acts as a filter. As the waste settles, these geosynthetic materials are subjected to significant tensile stresses (Rowe & Yu, 2019).

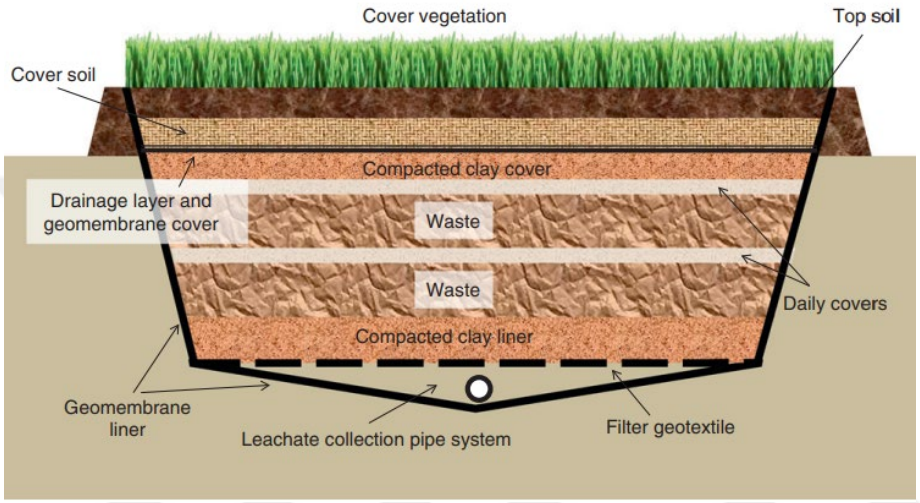

Figure 1.1. A typical cross-section of an engineered waste landfill (Ikehata & Liu, 2011).

The tensile strength becomes the primary design characteristic when geosynthetics are used for reinforcement and stiffening. Even for drainage and filtration, geosynthetics must satisfy specific sufficient tensile strength criteria (Zornberg & Gupta, 2010). Tensile tests can determine the tensile strength and the strain capacity. The geosynthetic specimen is placed in a constant rate extension testing machine (e.g., Universal Testing Machine, UTM) and subjected to a constant displacement rate until it fails according to a specific criterion. At the same time, load and deformation are measured to obtain the stress-strain curve at the end of the test. As a result, the following are generally reported: (i) maximum tensile force or stress at yielding and rupture, (ii) strain at yielding and rupture, and (iii) moduli of elasticity.

The accuracy in calculating the last two strongly depends on the technique employed to measure the strains.

Utilizing the travel of the UTM's crosshead for strain measurement is referred to as the Crosshead Displacement technique. It is based on the assumption that the specimen's elongation and UTM crosshead displacement are identical. However, the crosshead displacement may be inaccurate due to the possibility of slippage of the specimen within the grips, especially in the case of geotextiles, geosynthetic clay liners, and geogrids due to their significant tensile strength capacities. In addition, the crosshead displacement technique is unsuitable for all types of test grips, such as the capstan grips inside which specimens take up as the machine extends (Koerner, 2005).

Other strain measurement techniques, such as strain gauges and contact extensometers, quantify strains based on the changes in electrical resistance and elongation. These devices are either glued or placed by various means on the specimens. These techniques are listed in widely-employed test standards, such as the Test Methods for Tensile Properties of Geotextiles by the Wide-Width Strip Method (ASTM D4595, 2017), Determining Tensile Properties of Geogrids (ASTM D6637, 2015), and Geotextiles-Wide Width Tensile Test (ISO 10319, 2015).

On the other hand, non-contact extensometers quantify the strains by assessing the visual changes on a specimen as the test progresses. These devices use a camera, lighting sources, and data acquisition system to keep track of the specimen change, which have been more widely used as the technology progresses day by day. Without mechanical measurement, the specimen's elongation under tension is determined using images captured during the experiment. The usage of non-contact techniques in geosynthetics testing dates to the study of Leshchinsky & Fowler (1990). The study implements a photogrammetric displacement method and compares its results with strain gauge measurements. In their studies, Skochdopole et al. (2000) and Jones (2000) demonstrate the accuracy and advantages of using non-contact techniques over the traditional alternatives regarding lasers and video extensometers.

Undoubtedly, the advances in cameras, optical sensors, and computers nurture the development of image-based methods.

Although several commercial hardware and software for image-based strain measurement exist, most are expensive financially, especially for research and educational purposes. With the advances in open-source programming, the need for a cheaper, more straightforward, and still efficient method for determining strains during geosynthetic tensile tests is clear (Mishra et al., 2017; Poggiogalle et al., 2022). In line with these needs, the funnel of the research plan of this study is given in Figure 1.2, which expectantly leads to the practical measurement of strains during testing.

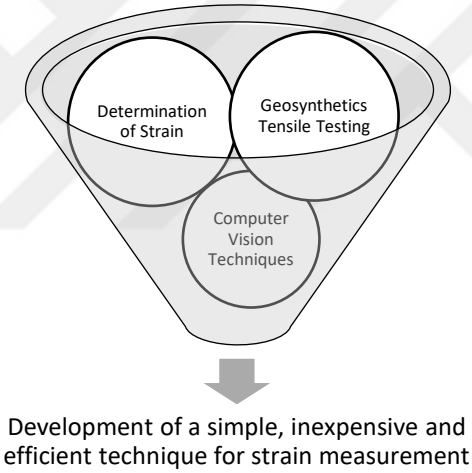

Figure 1.2. The funnel of the research plan.

1.1.1 Tensile Deformations of Geosynthetics

Geosynthetics are made of plastics, textiles, or a composition of both. In-plane strain measurement of geosynthetics is difficult in many aspects. Besides the obstacles in simulating the field conditions in the lab, practical issues such as clamping constraints, slippage of specimen in grips, and rate of strain, may skew the deformations from what is expected in the field.

From a material perspective, their behavior is rather complex. Lomov (2008) explains textiles' correct deformation state as a combination of tension and shear. Solid polymers also have a complex deformation nature with various co-occurring phenomena, such as yielding, strain hardening, and brittle fracture (Termonia & Smith, 1987). Thus, a simple yet correct and efficient strategy for strain measurement is needed.

1.1.2 Computer Vision

Computer vision grabs the attention of many researchers in various disciplines worldwide. It is being used as a valuable tool to analyze patterns and extract information from images. An understanding is thus developed through image processing, pattern recognition, and artificial intelligence (Wiley & Lucas, 2018).

Digital image processing is defined as the handling of images by computers. Images are digitized by being represented with a matrix of numbers. *Picture elements*, or in short *pixels*, are the small regions for this representation (Gonzalez & Woods, 2002). There are several processing techniques to extract information from the image. For instance, an image can be segmented based on color or texture. A binary mask can be created and improved by morphological operations such as opening and closing. Edges, corners, and shapes can be detected. Easy and fast application of all these tasks is made possible with the progress of digital image processing and made available for the use and benefit of engineers working in various disciplines.

Throughout history, the trend in engineering has been to combine computer vision with other related fields, such as photogrammetry. However, the difficulty of computer vision is inherent because the human eye is simply perfect for many tasks. Trying to mimic the eye and challenge the perception of humans is what makes computer vision a very demanding area of study. The computation time of a computer vision routine is often incapable of surpassing the performance of our visual system. Computer vision algorithms are generally reported as "brittle", as one

algorithm may not work for all cases (Huang, 1996). These features make computer vision attractive and open to further challenges in interdisciplinary research.

As part of developing a common working platform to solve the challenges above and enhance computer vision research, Intel Research created the open-source computer vision library OpenCV in 1999. The free and open-source library (FOS) supports business and educational use. Initially written in C and C++, the library is now also accessible in Python (Bradski & Kaehler, 2008). The library has been used in several commercial products and academic studies across many fields since its official release to the public in 2007.

1.1.2.1 Software Development for the Geotechnical Laboratory

Geotechnical engineers utilize software platforms such as Microsoft Excel, Mathcad, and MATLAB for specific tasks in practice and academia. Choosing the right platform requires many parameters, such as technical capabilities, usability, and affordability. Embracing different data acquisition platforms and connecting hardware is often desired from a simplicity point of view in the Geotechnical Engineering Laboratory (Adamo et al., 2018; Kaklamanos, 2016). At this point, the interoperability of engineering software with programming languages and the functionality of the selected language can be regarded as crucial. Moreover, the availability of well-defined and documented libraries makes an engineer's life easy while a program is being developed from scratch.

1.2 Aim of the Study

This study aims to develop an image-based strain measurement technique for geosynthetic tensile testing within the abovementioned perspective. The main objectives are given below:

- To develop a robust and reliable computer vision-based technique for measuring the strains during tensile testing of various types of geosynthetics, using free and open-source software libraries,
- To validate the proposed technique by testing different geosynthetics products and comparing the results obtained using traditional Crosshead Displacement and the widely used Digital Image Correlation (DIC) method.

1.3 Research Questions

In parallel with the main objectives given above, the following questions are expected to be answered in this study:

- Which digital image processing techniques may help develop the technique?
- How labor intensive is the technique in calculating strains of different geosynthetic types considering the efforts to prepare the laboratory experiments?
- How accurately can the method calculate the strains compared to existing ones such as DIC?

1.4 Scope and Method

The calculation of geosynthetic tensile strains by image-based techniques is a broad subject with many applications. The scope of the study is, therefore, limited to the followings:

- Among various geosynthetics used in the Geotechnical Engineering Industry, only tensile testing of geomembranes, geotextiles, and geosynthetic clay liners are studied in this thesis, and the rest of which is left for future studies.
- The developed MBDT technique calculates the strains by implementing OpenCV by measuring the elongations within a predefined gauge length (Bradski, 2000). With that, color markers are drawn on samples before the tensile test begins. The markers are first detected, then classified and continuously monitored, using the principles of image segmentation by color thresholding and edge detection. This study does not consider other techniques allowing us to keep track of objects, such as optical flow.
- This study includes the implementation of DIC as a reference image-based technique to validate the proposed one. Also, Crosshead Displacement strains are compared with MBDT. Finally, a comparison is provided by utilizing the conducted tests and reporting errors concerning these two techniques.
- Validation tests are conducted on different geosynthetic types, using different test speeds by following the guidelines of the most widely used test standards.

1.5 Organization of the Thesis

While this chapter provides an overview of the thesis with the objectives and scope, the rest of the chapters are organized as follows:

- Chapter 2 presents the literature on the applications of computer vision in geotechnical engineering, with a focus on the tensile testing of geosynthetics,
- Chapter 3 presents (i) the MBDT technique for the determination of strains during tensile testing of geosynthetics, and (ii) the implementation of DIC using open-source software,
- Chapter 4 includes the results of the validation tests and related discussions,
- Chapter 5 summarizes the thesis, draws conclusions, and emphasizes future work.

CHAPTER 2

LITERATURE REVIEW

2.1 Introduction

Geosynthetics, manufactured materials made of polymers and textiles, are very widely-used for (i) separation, (ii) reinforcement, (iii) filtration, (iv) drainage, and (v) containment purposes within soils (Koerner, 2005). Before being used in the field, geosynthetics must conform to required laboratory standards regarding their mechanical, hydraulic, and chemical properties. Tensile strength at yielding and rupture (i.e., break) and the maximum strain capacities are critical as geosynthetics often withstand significant tension force demands, whether due to gravity or induced by settlements (Giroud, 2005; Rowe & Yu, 2019).

Physical changes such as elongations, settlements, and cracks in geotechnical engineering must be carefully identified, and accurate measurements should be made. For this purpose, non-contact techniques can be used to continuously monitor and differentiate the changes in time and location domains successfully without inducing any physical damage to the specimens tested. Owing to the cameras' development, relatively low price, and the availability of computer vision software, the adoption of image-based methods in geotechnical engineering is expected to grow further (Thomas & Cantré, 2009). Accordingly, this chapter briefly presents the fundamental aspects and studies on (i) image-based strain measurement in tensile testing of geosynthetics, (ii) applications of computer vision in geotechnical testing, (iii) free and open-source software development for geotechnical engineering applications.

2.2 Strain Measurement in Tensile Testing

Widely used test standards for tensile strength measurement of geomembranes and plastics, ISO 527-3 (2018) and ASTM D638 (2014) recommend using an extensometer until specimen yields. However, after yielding, it is known that geomembranes exhibit necking, making the deformations highly inhomogeneous and localized. Therefore, contact extensometers become unsuitable after the yield point is reached. From then on, the standards recommend using the crosshead displacement for strain measurement. They define *nominal strain* as the ratio of the increase in distance between grips over the initial distance between the grips. In ASTM D6693 (2015), extensometers are not included in strain measurement due to their low popularity in the industry. Instead, the standard recommends two different gauge lengths for yielding (L_0=33 mm) and break (L_0=50 mm) for the specified Type IV specimens. Strains up to yielding and up to rupture are determined by dividing the crosshead travel by the corresponding gauge length.

ISO 10319 (2015) is a widely used index test standard for determining tensile strength and strain at the maximum load for geotextiles and related products. The standard defines the strain as the ratio of the change between two reference points 60 mm apart and located at the center of the specimen over the initial 60-mm distance. These reference points are to be tracked by contact or non-contact extensometers. Suppose the strains calculated by extensometers and crosshead displacement are compatible. In that case, measurements may be based on the nominal strain, defined as the ratio of the increase of grip-to-grip distance (e.g., crosshead travel) over the initial distance between the grips (L_0=100 mm). Its American counterfort ASTM D4595 (2017) also follows a similar methodology and presents the acceptable types of strain measurement devices, as shown in Figure 2.1.



(a)



(b)



(c)



(d)

Figure 2.1. Examples of strain measurement devices used for testing of geosynthetics. (a) Foil strain gauge. (b) Clip-on extensometer. (c) Roller extensometer. (d) Video extensometer (ASTM D4595, 2017).

Table 2.1 summarizes strain measurement techniques followed in some well-known tensile test standards. In the table, it is given that extensometers are widely referenced. However, their usage may be limited due to their constrained deformation capacity, and they can be broken when specimens rupture suddenly. In addition, attaching these gauges to specimens by creating holes may affect the material response (ASTM D4595, 2017; Leshchinsky & Fowler, 1990).

Table 2.1. Strain measurement techniques recommended by widely used tensile test standards.

Standard	Material Type	Strain Measurement Technique	Gauge Length For Yielding	Gauge Length For Break
ISO 527-3 (2018)	Plastic Films and Sheets	Extensometer / Crosshead Displacement	50 mm (Type 1B, 2, 4) 25 mm (Type 5)	115 mm (Type 1B) 100 mm (Type 2) 98 mm (Type 4) 80 mm (Type 5)
ASTM D6693 (2015)	Geomembranes	Crosshead Displacement	33 mm (Type IV)	50 mm (Type IV)
ASTM D638 (2014)	Plastics	Extensometer / Crosshead Displacement	50 mm (Type I, II, III) 25 mm (Type IV) 7.62 mm (Type V)	115 mm (Type I, III) 135 mm (Type II) 65 mm (Type IV) 25.4 mm (Type V)
ISO 10319 (2015)	Geotextiles, Geogrids, Geocomposites	Extensometer / Crosshead Displacement	-	60 mm (Extensometer) 100 mm (Crosshead Displacement)

2.2.1 Image-Based Strain Measurement in Tensile Testing

In Baldner et al. (2020) study, tensile testing is reported to significantly embrace computer vision practices, amongst other mechanical tests such as compression, impact, and hardness testing, constituting 73% of the reviewed papers.

As shown in Figure 2.2a, most studies (70%) on computer vision-based tensile testing benefited from the Digital Image Correlation (DIC) technique. The second most used technique is image segmentation using edge and shape detection. Only a small number of research have employed color analysis. When considering the material type, many studies are on metals and concrete, as indicated in Figure 2.2b. Only 10% of the reviewed papers investigated the tensile characteristics of geosynthetic fibers, composites, and polymers. Figure 2.2c shows that a considerable number of research papers have not disclosed their method for image acquisition. Nevertheless, the usage of CCD (charge-coupled device), SEM (scanning electron microscope), and DSLR (digital single-lens reflex) cameras was explicitly reported.

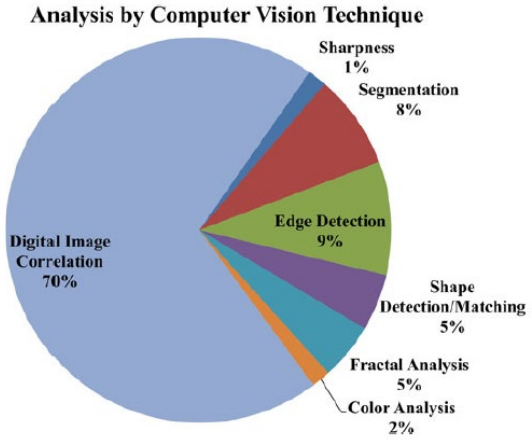

(a)

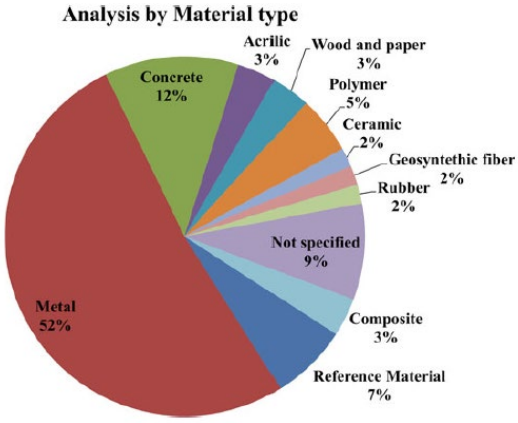

(b)

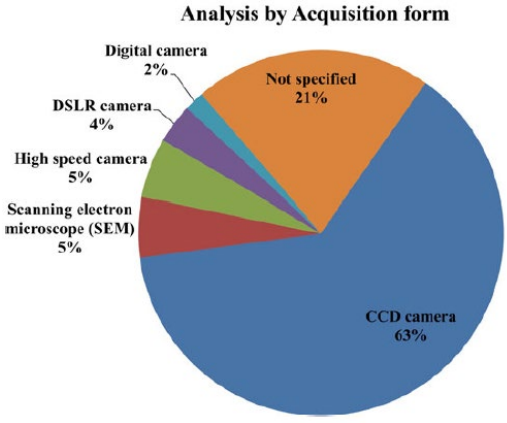

(c)

Figure 2.2. Distribution of (a) computer vision techniques, (b) material types, (c) image acquisition devices among a set of reviewed papers on computer vision-based mechanical testing (Baldner et al., 2020).

In the pioneering work of Jones (2000), "video extensometry", an image-based strain measurement technique, is presented. This new technique is compared to the contact extensometers for the wide-width tensile testing of geotextiles. Strain is quantified by keeping track of specimen elongation with respect to time. The elongation within a predefined gauge length is determined by tracking line markers, having sufficient contrast with the specimen, as shown in Figure 2.3. The study reports two crucial results: (i) the contact extensometers damage the textile fabrics while they are being attached to specimens, and (ii) calibration of contact extensometer takes considerable time when its compared to camera calibration efforts.

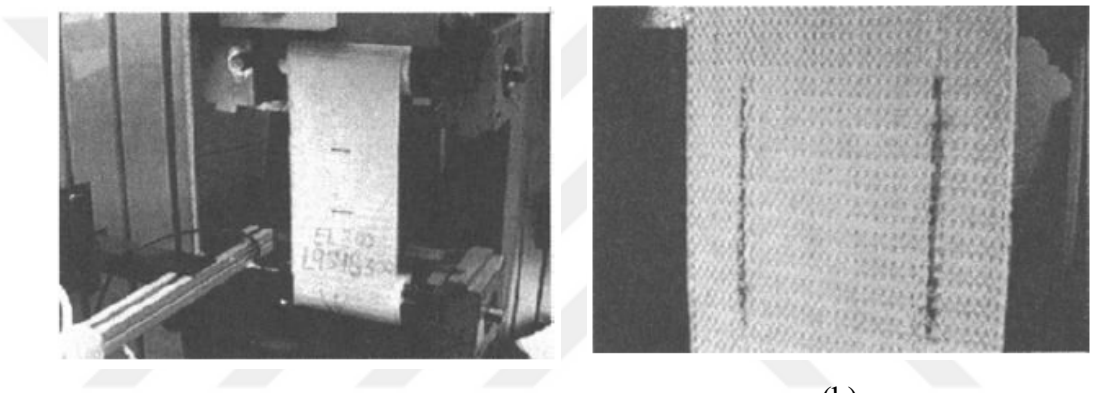

(a) (b)

Figure 2.3. (a) A capstan grip clamps a geotextile specimen. (b) The damage caused on by the attachment of contact extensometers causes the filaments in the machine direction to prematurely break (Jones, 2000).

Aydilek et al. (2004) used image analysis for geosynthetic tensile testing by investigating the tensile strains of geotextile, geogrid, and geocell materials. The study validates the technique used by strain gauge and extensometer measurements, as illustrated in Figure 2.4. The study points out that there is a need for continuous strain field quantification in order to achieve a better understanding of the material response. The study further criticizes the crosshead displacement technique as it provides no information about the local strains. Moreover, strain gauges and contact extensometers are evaluated as expensive, difficult to install, and incapable of measuring high strains. Instead, the study recommends image-based approaches.

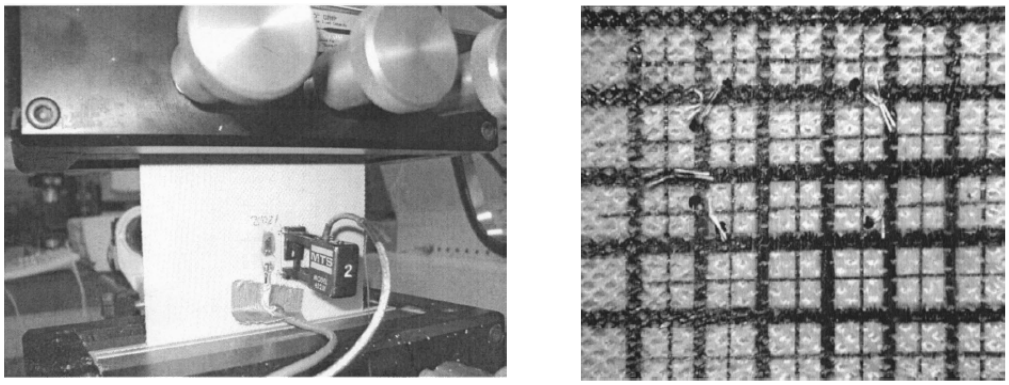

(a) (b)

Figure 2.4. (a) A clip-on extensometer and a strain gauge are attached to a geotextile specimen and clamped by testing grips. (b) Visible holes after the extensometer is attached (Aydilek et al., 2004).

As briefly described in Figure 2.5, Particle Image Velocimetry (PIV) technique, also known as Digital Image Correlation (DIC), operates by tracking a block set of pixels and comparing them at various deformation states. Speckle patterns often provide specimens with the random and distinctive texture needed for the technique to work successfully. The pattern is needed for defining a range of light intensity and contrast that identifies the block from other blocks on the image (McCormick & Lord, 2010). The use of this technique is possible with free and open-source software programs such as GeoPIV-RG (Stanier et al., 2015), Ncorr (Blaber et al., 2015), and commercial programs such as Aramis (GOM GmbH), Vic2D (Correlated Solutions Inc.), DynamicStudio (Dantec Dynamics). These software programs are extensively acknowledged in various research papers. For example, Qu (2007) and Diez (2010) utilize Aramis for the deformation analysis of glassy polymers under tension, and Albostan & Kurc (2016) employs Ncorr for the quantification of strains occurring during a flexure test of a reinforced concrete beam.

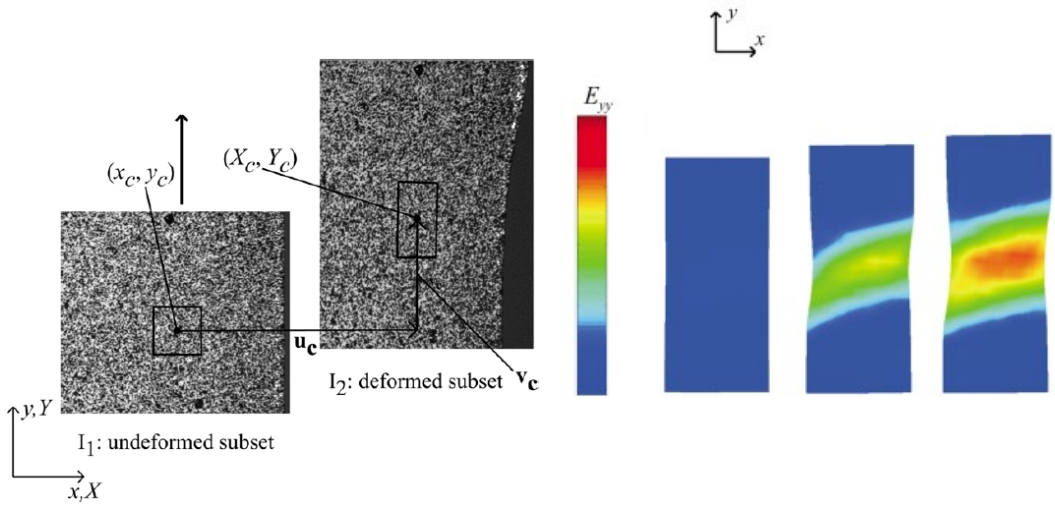

(a) (b)

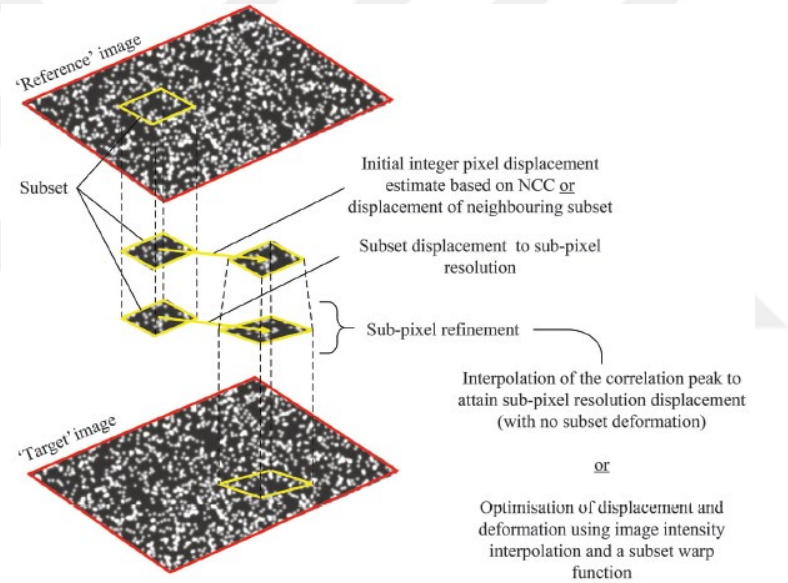

(c)

Figure 2.5. (a) Change of the speckle pattern from the undeformed to the deformed shape. (b) The color map showing the vertical strain distribution on a specimen, as the result of DIC (Parsons et al., 2004), (c) Image correlation process by GeoPIV-RG is explained (Stanier et al., 2015).

Parsons et al. (2005) investigate tensile deformation of high-density polyethylene (HDPE) materials in a three-dimensional analysis adopting Vic2D software by investigating local strain fields.

Mishra et al. (2017) present a low-cost yet accurate image-based strain measuring method for tensile testing of geotextiles using the DIC technique with GeoPIV-RG software. The study compares DSLR and smartphone cameras for image capture and delves into the advantages of recording a video during the testing rather than taking still photos. The tested geotextiles' vertical and horizontal strain distributions are shown in the conclusion.

Jayalath and Wimalasena (2020) reported that the strains by DIC and strain gauge measurements are compatible. However, for the tested geogrids according to ISO 10319 (2015), it is reported that the nominal strain approach by the crosshead displacement technique overestimates the strains and thus produces higher values than the strains calculated by DIC. The study reports that this may be owed to machine compliance, slippage of specimens inside grips, or boundary effects.

Lasers are also widely used as an image-based technique to calculate geosynthetic strain. Skochdopole et al. (2000) illuminated markers drawn on specimens designating the gauge length using laser beams in a study on high-strength textiles. Based on marker reflection by laser beams, the laser extensometer tracks the change in the gauge length. One limitation of the study is that the extensometer can measure a maximum elongation of 280 mm, which may not be sufficient for a specimen that exhibits high strain before rupture. Up to 2% strain, the crosshead displacement-based nominal strain is identical to laser extensometer strains. However, no information was found for high strains. Laraba-Abbes et al. (2003) use an optical laser extensometer for kinematic measurements of rubber-like materials. The technique is based on the illumination of the specimen's surface by a laser beam, resulting in the spatial variation of the light intensity. These variations are called optical signature patterns, much like the speckle patterns applied for the DIC technique. The authors note a significant advantage in that no sample preparation

(e.g., creating a speckle pattern or drawing paint markers) is needed due to the presence of the laser. Zhu et al. (2012) also employ a laser extensometer for the dynamic testing of cement-based composites. Figure 2.6 shows the methodology followed briefly. The study points out that (i) laser extensometer has no apparent advantages over using LVDT-based contact extensometers for a slow loading rate, and (ii) both laser extensometer and image analysis methods are effective for high strains.

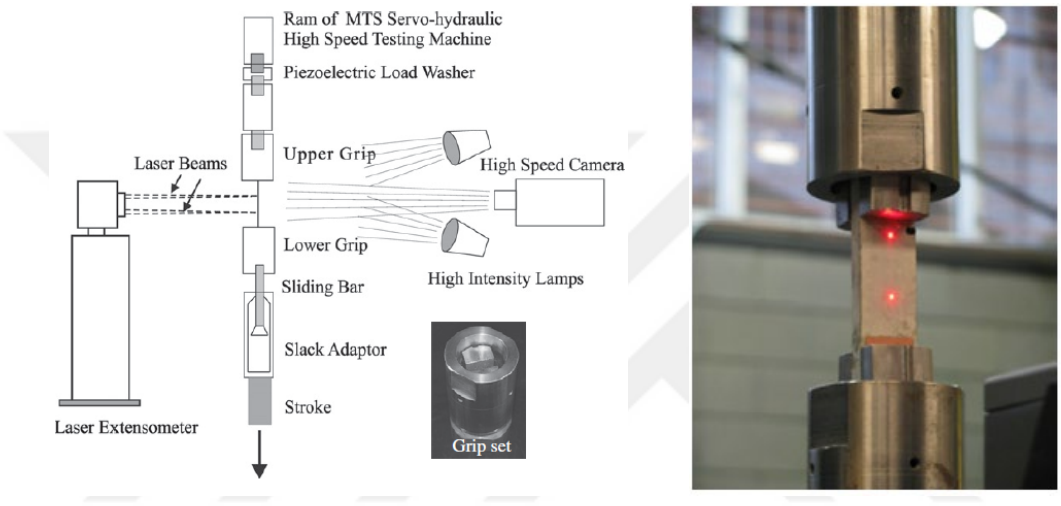

(a) (b)

Figure 2.6. A laser extensometer is used for the tensile testing of cement-based composites. (a) Schematic drawing of the experiment setup. (b) Laser beams mark the gauge length (Zhu et al., 2012).

A multi-camera photogrammetric technique is used in the recent study by Xia et al. (2021) to assess the dynamic 3D strain field of geosynthetics under tensile test. The study emphasizes how little information regarding camera calibration exists in the non-contact geosynthetic measurement literature. Instead of using photogrammetric 3D reconstruction approaches for static objects, the suggested multi-camera method is distinctive because it is employed for dynamic modeling. There is no information provided regarding the software development platform; however, it is reported that the computational demand is substantial.

A digital image analysis technique utilizing an open-source platform, R programming, is employed for the low-cost implementation of non-contact measurements in the study on tensile testing of geotextiles conducted by Poggiogalle et al. (2022). The technique segments the images a DSLR camera takes using the color markers indicated in Figure 2.7b. As shown in Figure 2.7, after reaching 50 kN/m, there is a significant difference between the load-strain behavior predicted by the suggested image analysis technique and the crosshead displacement (i.e., machine boundary)—problems with specimen slippage and tightening cause this. Laser extensometer measurement is used to validate the technique.

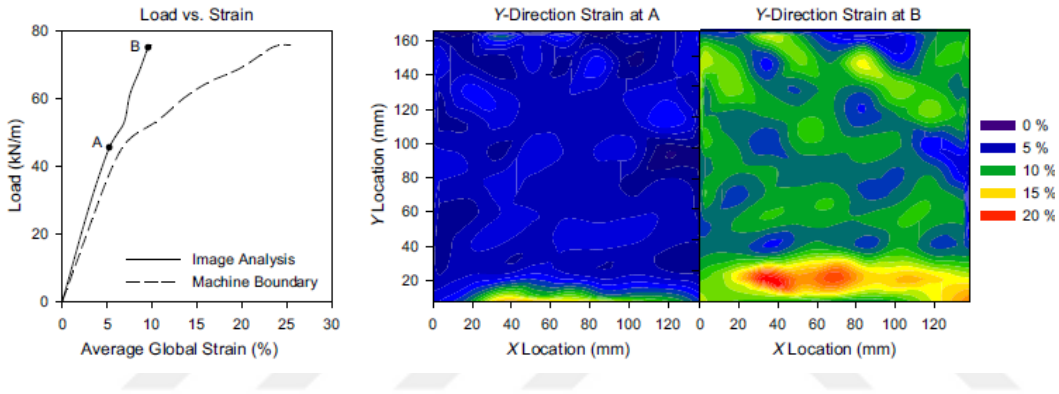

(a)



(b)

Figure 2.7. In R, an image-based technique is created and used to measure the tensile strains of geotextiles. (a) The stress-strain graph is created using the suggested technique and the crosshead displacements. By using a heatmap, strains are shown. (b) Before testing, a dot grid is drawn on the geotextile sample (Poggiogalle et al., 2022).

2.3 Applications of Computer Vision in Geotechnical Testing

In a broader sense, computer vision is utilized by both tensile testing and geotechnical laboratory testing. Unlike the previous section focusing on image-based strain measurement techniques for tensile testing, this section provides an incomplete summary of the studies utilizing computer vision for various fields of geotechnical testing, such as triaxial testing, transparent soils, and centrifuge modeling.

In Hryviw & Raschke (1996) study, soil images are segmented by applying a cut-off threshold separating the background and the soil grains. In order to better understand how geotextile structures reorganize in response to uniaxial tension stresses, Thorr et al. (1999) developed an optical sensor to assess the textural parameters of geotextiles. A light source illuminates the specimen, and the amount of transmitted light is then determined using grayscale pictures. After that, the macrostructure is examined, making it possible to characterize the fibers' structural pattern.

Guler et al. (1999) used video recordings of shear bands and local deformations of granular soils to comprehend the actual displacement field. In order to track particle movement, the authors use moving patterns on images and look for specific block sizes using a matching criterion.

The distribution of filaments at the geotextile and geomembrane interfaces is studied by Kim & Frost (2007). Using feature detection, the high-resolution images of specimens taken with optical microscopy are processed after binarization. Geotextile filament concentrations under different normal stresses are identified using the image analysis technique that is being described.

According to Tang et al. (2013), geotextile filters are typically under tension in the field; however, this circumstance is not replicated in the tests to ascertain their typical pore size. As seen in Figure 2.8, once photos are processed in the study with morphological procedures to reduce noise, the grayscale images are then used to segment the pores.

In a recent paper, E Silva et al. (2019) present an image-based technique for automatically producing non-woven geotextile pore size distribution curves. Support Vector Machines, a machine learning method, classifies pictures and recognizes pores from macroscopic images.

Zangl & Likos (2016) investigated the wet-dry cycling performance of geosynthetic clay liners (GCL). A color image scanner scans images of the bentonite layer after the geotextile layers have been eliminated. They are then transformed into an 8-bit grayscale image before going through the morphological closing operation. Finally, crack patterns and intensities are identified.

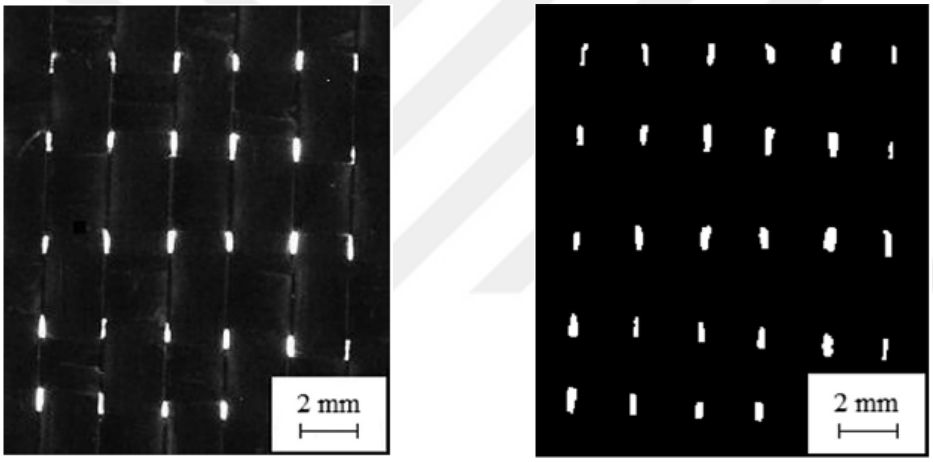

(a) (b)

Figure 2.8. The enlarged pore sizes of a geotextile specimen which is kept under tension. (a) The grayscale image. (b) The binary mask after being processed with morphological operations (Tang et al., 2013)

In the study by Uy & Boonyatee (2016), the LabVIEW environment is used to construct the Lucas-Kanade optical flow algorithm in order to track the 3D displacements of specimens during triaxial testing. The membrane is marked with grids, and two Canon 650D cameras are used to take pictures with a zoom lens that has an 18-55 mm focal length and an f/3.5-5.6 aperture. As seen in Figure 2.9, the computed strains are displayed on color maps.

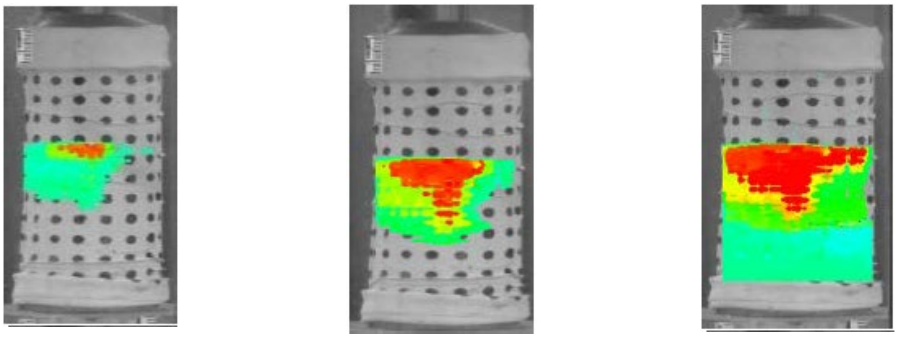

Figure 2.9. Strain distribution during a triaxial test, obtained by the optical flow algorithm (Uy & Boonyatee, 2016).

The transparent soil technique is based on immersing a translucent material as the soil in a liquid with a similar light refraction index that serves as the pore fluid. When the pore fluid is inserted, the translucent soil becomes transparent. Figure 2.11b illustrates this technique, making the geogrid inside the transparent soil visible.

In Ferriaga & Zornberg (2015) study, a transparent pullout test device is developed to obtain displacement fields for soil-geogrid interaction problems. Because the transparent soil makes the geogrid visible, the speckles drawn on the specimen are used to quantify the strains using DIC, as shown in Figure 2.11a.

Peng & Zornberg (2019) enhance the soil-geogrid interaction evaluation by incorporating lasers. Their setup, shown in Figure 2.10, includes two cameras; one for tracking the planar deformations of geogrid and the other for tracking the displacement field of transparent soil grains illuminated by a compact laser source. The fact that the grains refract the laser beams makes the deformation analysis within the soil possible by creating unique lighting intensity throughout the soil body (Figure 2.10b). An open-source DIC code has been used for image analysis.

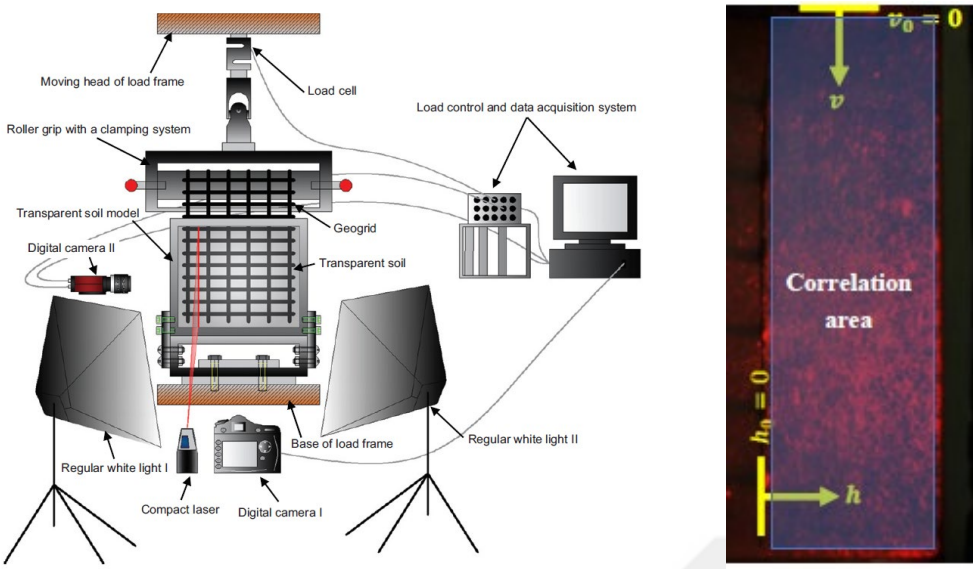

(a) (b)

Figure 2.10. Two cameras are utilized for the deformation tracking methodology for the transparent soil reinforced with geogrids. (a) A schematic diagram of the test setup. (b) The correlation area on the transparent sand is formed by the refraction of laser beams from the grains (Peng & Zornberg, 2019).

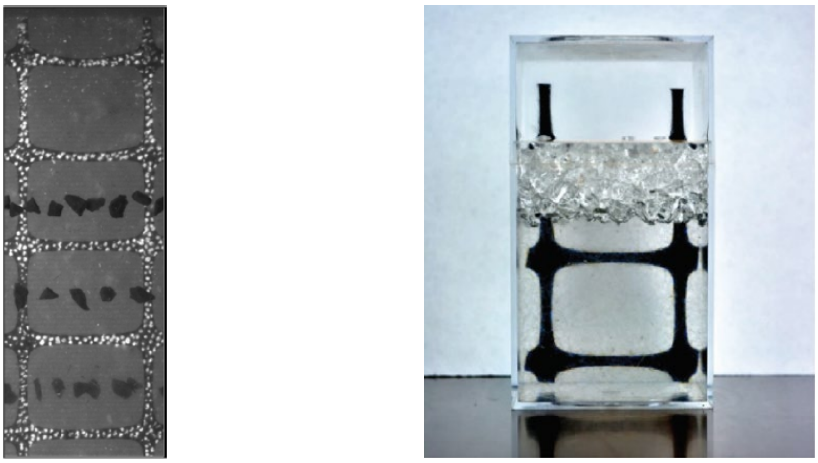

(a) (b)

Figure 2.11. (a) A speckle pattern is applied to the geogrid specimen (Ferreira & Zornberg, 2015). (b) The geogrid specimen inside the transparent sand is shown after the pore fluid is inserted (Peng & Zornberg, 2019).

Marx et al. (2022) quantify displacements in monotonic triaxial experiments with transparent sands stabilized by geogrids using lasers and the DIC technique. In variance with the other works, a deep learning algorithm is used to segment soil grains from the transparent soil illuminated by the laser. The movements of rotation and displacement are then determined by tracking individual grains. Figure 2.12 explains the followed procedure briefly.



(a) (b) (c)

Figure 2.12. (a) Grayscale image of the stabilized transparent sand. (b) The segmented image. (c) Grain probabilities are indicated by color densities, with edges of the actual grains (Marx et al., 2022).

Slopes and interface shear tests are also investigated in the context of computer vision applications for geotechnical testing. Vangla and Gali (2014) present the application of image segmentation techniques to quantify the deformations of sand-geosynthetic interface shear tests by utilizing MATLAB Computer Vision Toolbox (The MathWorks Inc., 2023). Zornberg & Arriaga (2003) assess the strain distribution on slopes soon before failure using a combination of centrifuge modeling and digital image analysis. The authors have analyzed images taken from video records of centrifuge tests to determine the displacement field of the reinforced soil slope. Eichhorn et al. (2020) employ Raspberry Pi single-board computers and their cameras in search of an inexpensive strain measurement for slopes, as shown in Figure 2.13a. An open-source camera calibration scheme, OpenCV ChArUco board,

is utilized. Four cameras are employed to capture the whole slope fully, and DIC is used to compute shear strains, as illustrated in Figure 2.13b.

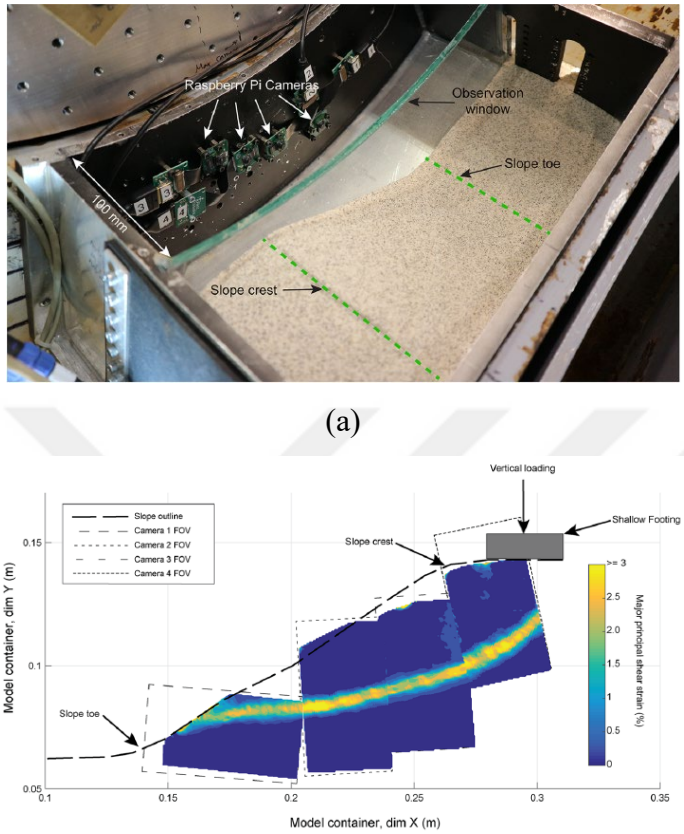

Figure 2.13. Measurement of shear strains on an experimental study on slopes. (a) Four Raspberry Pi cameras are employed to capture the failure progressing on the slope. (b) DIC is utilized for the quantification of shear strains (Eichhorn et al., 2020).

2.3.1 Open-Source Software Development in Geotechnical Engineering

The last section of Chapter 2 focuses on the studies in geotechnical engineering literature employing open-source software development. Engineers frequently use open-source programming languages because they are cost-free, widely used by developers, and include a variety of software libraries (Lenarduzzi et al., 2020).

A software package for geotechnical engineering utilizing the free and open-source programming language R is presented by Kaklamanos (2016). With the use of the program, routine practical activities like calculating bearing capacity, settlement, and generating grain size and effective stress plots can be completed rapidly.

Py2DIC is a free and open-source DIC program that is presented by Belloni et al. (2018). The application features a graphical user interface and makes use of OpenCV. The paper emphasizes that open-source MATLAB routines require a license to execute and underlines the costs associated with DIC software. The results of Py2DIC, according to the authors, are compatible with the commercial DIC program Vic2D.

As seen in Figure 2.14, Zhao et al. (2013) created DIC software in C++ that incorporates OpenCV to measure soil deformations. The authors highlight the importance of image-based testing techniques for geotechnical research. The study used a neural network-based camera calibration methodology from OpenCV.

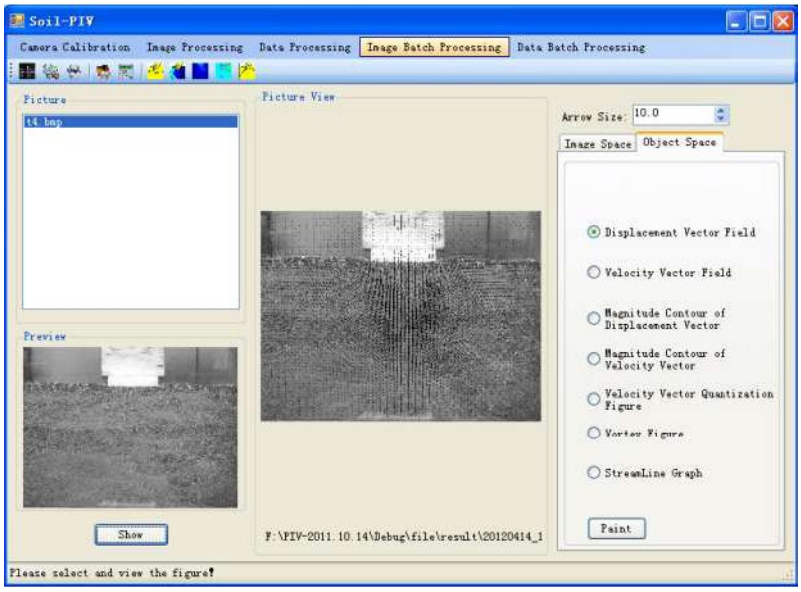

Figure 2.14. The user interface of the soil deformation measurement software developed in C++ (Zhao et al., 2013).

In their paper on geotechnical laboratory testing, Li et al. (2018) utilize OpenCV with Python to extract grain shape parameters of the Fujian standard sand. A threshold limit is set to segment the grains on grayscale images. In a recent study by Madrigal et al. (2021), a software program for soil classification was developed with Python, incorporating OpenCV for computer vision and the Tkinter library for GUI design. Their methodology includes segmentation, preprocessing, and feature extraction after capturing images with a Logitech HD C920 webcam at 30 frames per second and in 1080p image size. Color images are processed after resizing them to 300 x 400 pixels, and then object identification is carried out on the grayscale images. A convolutional neural network is used to classify the soils inside a jar, then placed in a black box where images are captured. The setup and software are shown in Figure 2.15.

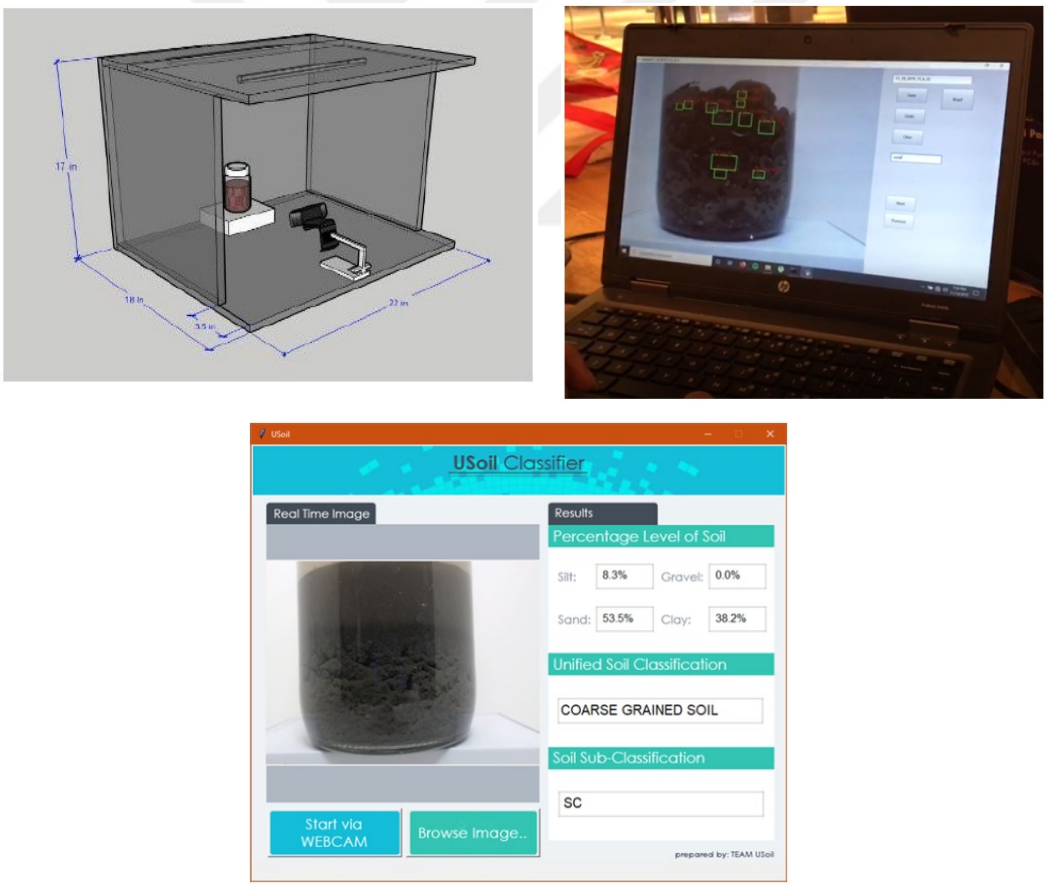

Figure 2.15. Soil classification platform developed by Madrigal et al. (2021).

2.4 Summary

Chapter 2 presents the most relevant studies and state-of-the-art image-based strain measurement techniques for geosynthetic tensile testing. The literature findings are as follows:

- As summarized in Table 2.1, test standards have different instructions on strain measurement techniques. Using an extensometer for strain measurement is often recommended. However, the nominal strain approach based on crosshead displacement is beneficial if necking is observed after yielding.
- According to Figure 2.2, tensile testing is suitable for computer vision applications; however, geosynthetics are not widely investigated. Also, no other camera types rather than CCD have been often employed.
- Among the non-contact strain measurement methods, DIC is the most utilized one, and many researchers have shown that open-source alternatives may implement this technique well.
- Although image-based techniques for geosynthetics testing have been shown to be accurate and applicable, there still exists a need for cost-efficient yet successful means to spread the use of image-based strain measurement. Thomas and Cantré (2009) owe the need for such solutions to the rapid development of cameras, their relatively low price, and inexpensive software packages.
- Computer vision is not only implemented for strain measurement in tensile testing but there are also innovative studies in which digital images are highly beneficial, such as the determination of pore opening size of geotextiles, finding out the strains during triaxial testing of soils and investigating shear bands in centrifuge modeling of slopes.

CHAPTER 3

STRAIN MEASUREMENT USING COMPUTER VISION

Accurate measurement of deformations is crucial to assess the tensile strain capacity of geosynthetic materials. Geosynthetics tensile testing standards have recently included non-contact measurement systems (ASTM D4595, 2017; ISO 10319, 2015). These systems eliminate the problems due to specimen slippage inside the grips, machine compliance, and damage caused by contact extensometers on specimens. Non-contact extensometers, the instruments that are used for remote strain measurement, track changes in a predefined length or boundary, identified by visual markers or patterns. Commercially available software packages and specific hardware setups serve this purpose. However, these products may pose financial constraints for research purposes or may only be compatible with particular machines or setups. Moreover, if sold as an attachment to a Universal Testing Machine (UTM), such products may be limited to testing specific materials.

Therefore, this study aims to find strains remotely during tensile testing by utilizing free and open-source software packages. Two different approaches have been followed: (i) the development of an image segmentation-based displacement tracking technique and (ii) the utilization of the well-known Digital Image Correlation (DIC) technique to determine strains, which will then be used to validate the developed technique. Both approaches involve the steps of specimen preparation, image capturing, and camera calibration. As a result, most of the sub-chapters cover both techniques.

The image segmentation-based technique developed in this thesis was implemented in Python v.3.9.5 and relies on the well-known computer vision library OpenCV v.4.6.0 (Bradski, 2000). This study utilizes the open source codes provided by

OpenCV, with some crucial improvements made to meet the objective of quantifying the strains during geosynthetics tensile testing. The technique also incorporates lens distortion corrections and digital image processing techniques to monitor changes in the gauge length throughout the test. As the technique revolves around identifying and tracking the drawn markers, it is called the *Marker-Based Displacement Tracking (MBDT)* technique.

DIC is one of the most applied non-contact strain measurement techniques. This technique relies on differences in light intensities on the surface of the specimen, typically achieved by applying unique patterns to the specimen. DIC calculates and provides continuous strain distribution on the specimen surface by partitioning the specimen into subsets and tracking their movement during the test. As part of developing a new approach, this study implements Ncorr software (Blaber et al., 2015), a free and open-source DIC tool within MATLAB, to validate the MBDT technique.

3.1 Specimen Preparation

This study employs a brand-new specimen marking technique using a hybrid marking scheme, as shown in Figure 3.1. Typically, designating the gauge length with two color markers is sufficient for the MBDT technique to perform strain analysis. Therefore, the preparation of the specimens can be as simple as those shown in Figure 3.1a and Figure 3.1c. Alternatively, speckles can be added, as depicted in Figure 3.1b and Figure 3.1d, to enable DIC to apply strain calculations in both techniques. The later chapters will elaborate on how this marking style benefited the validation tests. Since the MBDT technique relies on image segmentation using color thresholding and edge detection, it is crucial to use saturated colors and ensure adequate illumination in the testing environment.

Preparing geomembrane specimens is a two-step process: applying paint markers first, followed by a desired color of board marker. The paint marker, used in white

paint, provides sufficient integrity and serves as an undercoat for the color paint. The color paint, preferably with high contrast to the sample, is then applied to enable the segmentation algorithm based on color thresholding. This process is explained in detail in Section 3.4. Geotextile specimens do not need an undercoat paint, and the color can be directly applied via a board marker, as shown in Figure 3.1d.

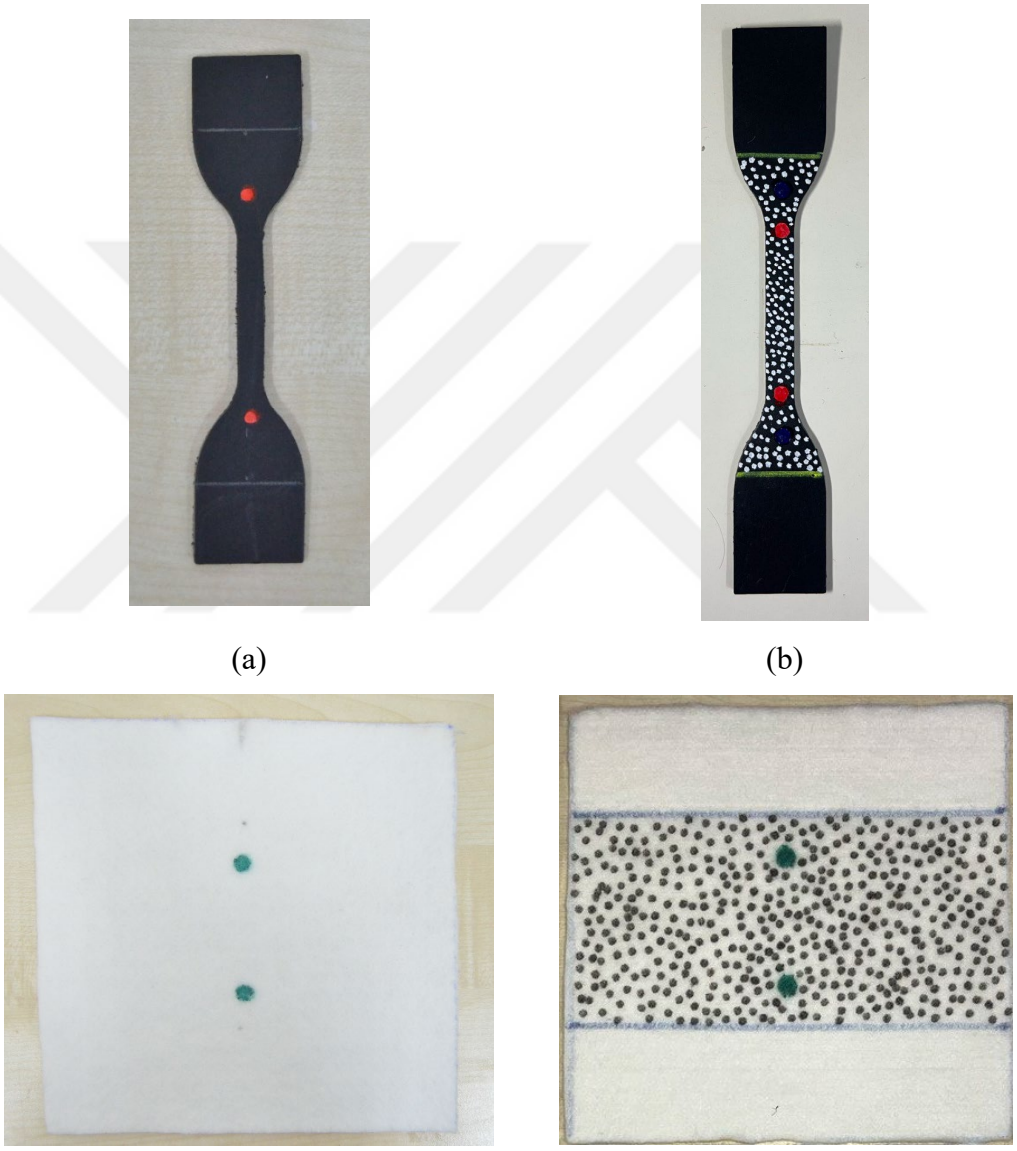

(a) (b)

(c) (d)

Figure 3.1. Preparation of test specimens. (a) Geomembrane with two color markers. (b) Geomembrane with multi group color markers and speckle pattern. (c) Geotextile with a single pair of color markers. (d) The same geotextile with a speckle pattern added. The color markers designate a predefined gauge length on all specimens.

Unless the specimen body already has recognizable, distinct optical patterns, DIC requires the introduction of speckle patterns. Speckle patterns can be applied to the specimen surface using various materials and techniques, as shown in Figure 3.1b and Figure 3.1d, which require a different technique for each geosynthetic type. It is important to note that the material's nature significantly influences the patterns' effectiveness and quality. Some DIC software programs have provided helpful guidelines on applying these patterns. In particular, the application notes on speckle patterns by Correlated Solutions Inc. (2021) were very useful and followed for this study. In summary, the following recommendations can be given for preparing specimens:

- The pattern can be spray painted, drawn with permanent markers, or printed and adhered to the specimen.
- High contrast is essential; it is preferred to have either white dots on a black background or vice versa.
- The pattern should include equal areas of white and black regions.
- The speckle pattern should maintain consistency in terms of speckle size and randomness in terms of the directions and locations of the speckles.

The application note recommends employing permanent markers (such as paint markers or board markers) rather than spray paint because the latter can become brittle after drying for materials that undergo considerable strain before break. This recommendation has been confirmed through the tests that were performed for this study. Through numerous tests, it became apparent that board markers used on geotextile samples and paint markers used on geomembrane samples produced speckles, which resulted in good correlations at the end. Ineffective tests with geomembrane samples are shown in Figure 3.2. The contrast between the ink and the spray paint was insufficient, and the spray paint disintegrated and spalled after drying, as seen in Figure 3.2a. The size and quantity of the speckles were also found to affect the success of the correlation. Figure 3.2b shows that establishing a correlation with only a few speckles was unsuccessful.



(a) (b)

Figure 3.2. Speckle pattern application trials resulted in unsuccessful correlations. (a) Ink is applied on a spray-painted body, resulting in spalling of paint and unidentifiable speckles. (b) Correlation cannot be established due to few speckles.

3.2 Capturing Images

It is essential to take a sufficient number of high-quality images during the test to measure strains during tensile testing accurately. The procedure covered in this chapter uses different methods for image acquisition. Among the image-based techniques used in this study, the Marker-Based Displacement Tracking (MBDT) technique utilizes video input, essentially a combination of multiple images. In contrast, the DIC technique relies on capturing still images. When capturing photos using DSLR cameras, there may be a slight vibration caused by the opening and closing of the camera aperture. On the other hand, capturing a video with most cameras does not cause any physical disturbance, providing an abundance of image frames for displacement analysis. Nevertheless, still images can easily be captured from a video record using OpenCV.

It is important to note that the captured images must be undistorted, which necessitates completing the camera calibration process beforehand. While a high-quality lens may introduce minimal distortion in the middle of the frame, distortion becomes more noticeable near the edges. Since most geosynthetics, particularly geotextiles tested in this study, experience high strain before rupture, the test specimens are likely to elongate until they reach the edges of the frame during testing. Accordingly, the sources of distortion are briefly explained below.

3.2.1 Lens Distortions

Almost all lenses have certain manufacturing imperfections which cause distortions across each image. These defects might result in *radial distortion*, caused by the lens' sphericity. Errors referred to as *tangential distortion* can also be a result of lens and image sensor misalignment. Distortions caused by lenses are shown in various forms in Figure 3.3 and Figure 3.4.

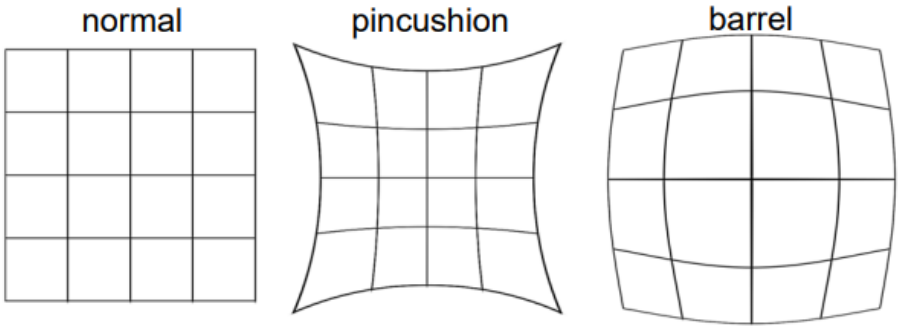

Figure 3.3. A normal image frame and two types of radial distortions.

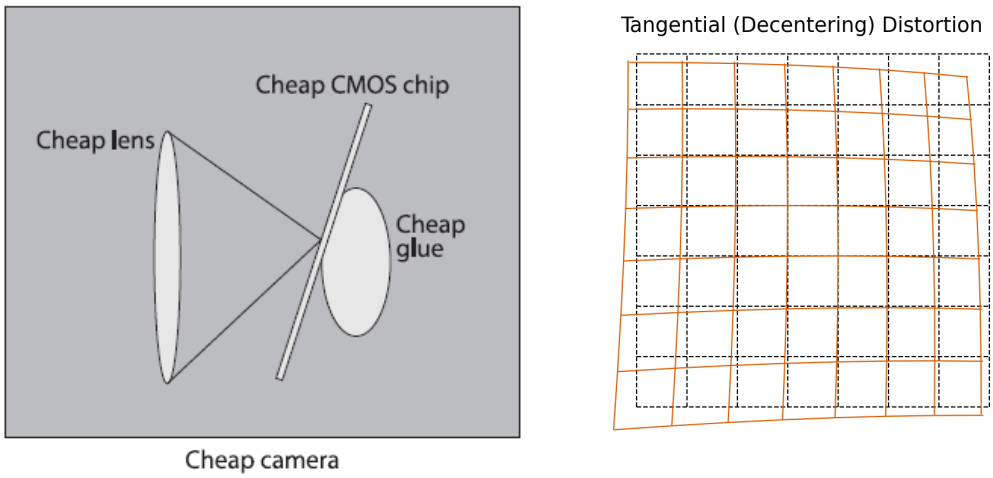

(a) (b)

Figure 3.4. (a) Schematic view of the lens configuration that causes tangential distortion due to manufacturing errors (Bradski & Kaehler, 2008). (b) An example of the tangential distortion illustrated on an image frame.

Although cameras use an intricate combination of different lenses to get the best image possible, distortions can still happen. For instance, outdoor action cameras frequently use ultra-wide-angle (i.e., fisheye) lenses. They are made to capture a broad field of view without sacrificing sharpness or adding blur. The lens configuration is carefully chosen to keep the image bright and sharp while including a variety of objects. Figure 3.5 illustrates a schematic structure of the fisheye lenses.

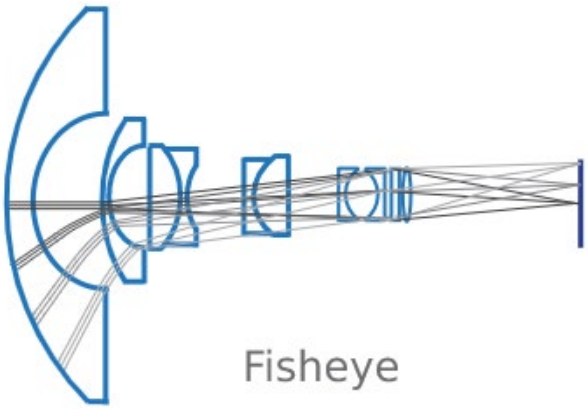

Figure 3.5. A schematic representation of a fisheye lens configuration. Multiple lenses are used in combination (The MathWorks Inc., 2023).

3.3 Camera Calibration

An essential step in lens distortion correction is camera calibration. Images cannot be correctly utilized for measurements without this correction since each pixel may have a different size. The intrinsic camera matrix (i.e., camera matrix) and lens distortion coefficients are back calculated during calibration. These parameters are then used to generate corrected versions of the images, removing the distortions. The calibration process can also provide extrinsic camera matrix, which defines the camera's position and orientation within the capturing environment.

This study utilizes the camera calibration routine provided by OpenCV, which employs Zhang's method (2000) in the background. A calibration board in the shape of a checkerboard with identically sized black and white squares is utilized in the image frames for calibration shots. Since the checkerboard is flat and has the same distances between each grid square in reality, the calibration algorithm finds the camera matrix and lens distortion coefficients by back calculations. The calibration board's position and rotation with respect to the camera's optical axis are thus established by determining the camera matrix and calculating the extrinsic camera matrix for each image, respectively. A schematic illustrating the inputs and outputs of the camera calibration process is presented in Figure 3.6.

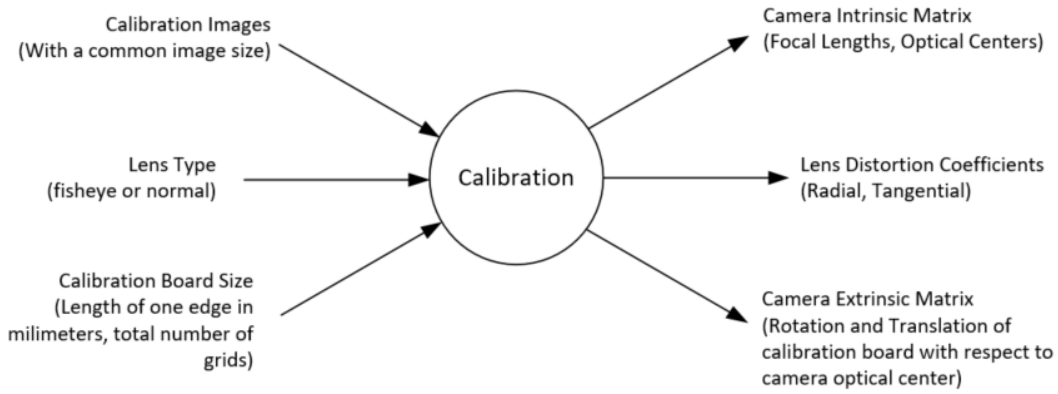

Figure 3.6. Summary of the OpenCV camera calibration routine, with inputs and outputs.

Mathematically, camera calibration involves the back calculation of the intrinsic camera matrix (K), the lens distortion coefficients (d), and the extrinsic camera matrix. In the case of OpenCV, the calibration process uses four intrinsic camera parameters and five lens distortion coefficients, which are defined as follows:

$$K = \begin{bmatrix} f_x & 0 & c_x \\ 0 & f_y & c_y \\ 0 & 0 & 1 \end{bmatrix}, \; d = \begin{bmatrix} k_1 & k_2 & p_1 & p_2 & k_3 \end{bmatrix}$$

Here, f_x and f_y denote the focal lengths, while c_x and c_y are the optical centers in pixels. k_1, k_2, and k_3 (only for fisheye lenses) correspond to radial distortions, while p_1 and p_2 are calculated only for tangential distortions. In addition, the camera extrinsic matrix includes the rotation and translation vectors that define the object's location with respect to the camera's optical axis. Finding this matrix makes it possible to project real-world points onto the image plane. Once the projection is performed, the image can be corrected by compensating for the distortions induced by the lens, resulting in an undistorted and accurate representation of the object.

Evaluating the accuracy of these parameters can assess the success of the calibration process. Additionally, visually examining the corrected images can provide a qualitative assessment of the calibration results. To quantify the calibration accuracy, *reprojection error* is commonly calculated. The reprojection error measures the difference between the coordinates of the initially identified grid points on the checkerboard and the corresponding reprojected grid points in the corrected images. After obtaining the extrinsic camera matrix, the grid coordinates are reprojected onto the image frame without relying on calibration board detection algorithms. The mean error is then calculated for each grid point on the checkerboard and each image. In Chapter 4 of this study, the validation of the calibration methodology is presented in

detail. The success of the calibration routine is examined for both normal and fisheye lenses, assessing its effectiveness and accuracy.

3.4 Calculation of Strains by Image Segmentation: Marker-Based Displacement Tracking (MBDT) Technique

Images that depict 3D objects on a 2D image plane frequently have more information than is necessary for a given computer vision task. Digital image processing techniques can be applied to the captured images to extract the most relevant information and reduce unnecessary details. By dividing an image into its subcomponents, image segmentation, a fundamental computer vision technique, enables the recognition of objects on images.

In the context of grayscale images, image segmentation algorithms commonly rely on two main characteristics: similarity and discontinuity of the light intensity levels. The algorithms based on similarity aim to partition the images by grouping the pixels that have similar intensity values. *Thresholding* is an example of similarity-based segmentation (Gonzalez & Woods, 2002). A threshold limit is selected to divide the pixels into two groups—those with intensity values above the limit (foreground) and those with intensity values below the limit (background). This procedure produces a binary mask, with the foreground represented by white pixels and the background by black pixels.

On the other hand, algorithms based on the discontinuity of pixel light intensities emphasized locating edges or boundaries between regions with different levels of light intensities. For example, edge detection algorithms locate the areas of significant light intensity changes in the image. These edges are connected lines or curves, highlighting the boundaries between objects or regions.

In the MBDT technique, thresholding is used for image segmentation, generating a binary mask that distinguishes between the foreground and background regions. Edge detection is then used to examine the segmented image further and locate the

boundaries or edges of the objects or regions of interest. The resulting edge image helps accurately track markers' displacement and deformation during the geosynthetics tensile testing. The process is further explained and illustrated in Chapter 3.4.4.

3.4.1 Overview

This section presents the details of the MBDT technique developed in this study. The utilized image segmentation methods are described, and the flowcharts are given.

The MBDT technique presented in this study offers an alternative approach for accurately determining strains during the tensile testing of geosynthetic materials. This study applies color image processing, whereas previous studies have utilized other computer vision techniques, such as DIC and optical flow algorithms.

The developed Python program modules enable the continuous tracking of gauge length elongation during tensile testing. Before processing the captured test video, several inputs are required, including (i) the camera matrix, (ii) Hue-Saturation-Value (HSV) color threshold limits, (iii) millimeters-to-pixels ratio, and (iv) marker size and location information. These inputs can be provided by the user following simple and clear instructions. Once the necessary inputs are provided, the program processes the video using the specified parameters. The program applies the camera matrix to correct lens distortions, uses color thresholding techniques based on the HSV color space to segment the markers, and utilizes the millimeters-to-pixels ratio to convert elongation measurements from pixels to real-world units. The program modules also consider marker size and location information to accurately track the displacement of the gauge length throughout the test. The program calculates the elongation and corresponding strains by assuming uniformity along the gauge length. The detailed subchapters comprehensively explain the procedure, guiding users through the necessary steps to obtain accurate gauge length elongation and strain measurements using the developed Python program modules.

3.4.2 Program Flow

Figure 3.7 presents the main program flow for analyzing a video record of a tensile test. The program starts by gathering the necessary inputs, the test video, and some information such as the lens type, marker area and location limits, and the camera matrix.

Since a video consists of multiple image frames, the main program loop continues to run until all the frames in the video have been analyzed. The number of frames can vary depending on the frame rate of the video. For example, if the video has a frame rate of 30 frames per second and a duration of 100 seconds, there would be a total of 3000 image frames to be analyzed.

The program processes each frame individually, applying the necessary image processing techniques, such as lens distortion correction, color thresholding, and marker tracking. The displacement and strain calculations are performed based on the tracked marker positions. Looping through all the frames and performing the required analysis, the program comprehensively evaluates the gauge length elongation and corresponding strains throughout the test duration.

The main program flow depicted in Figure 3.7 ensures that each image frame in a video record is analyzed and contributes to accurately determining strains during the tensile testing process.

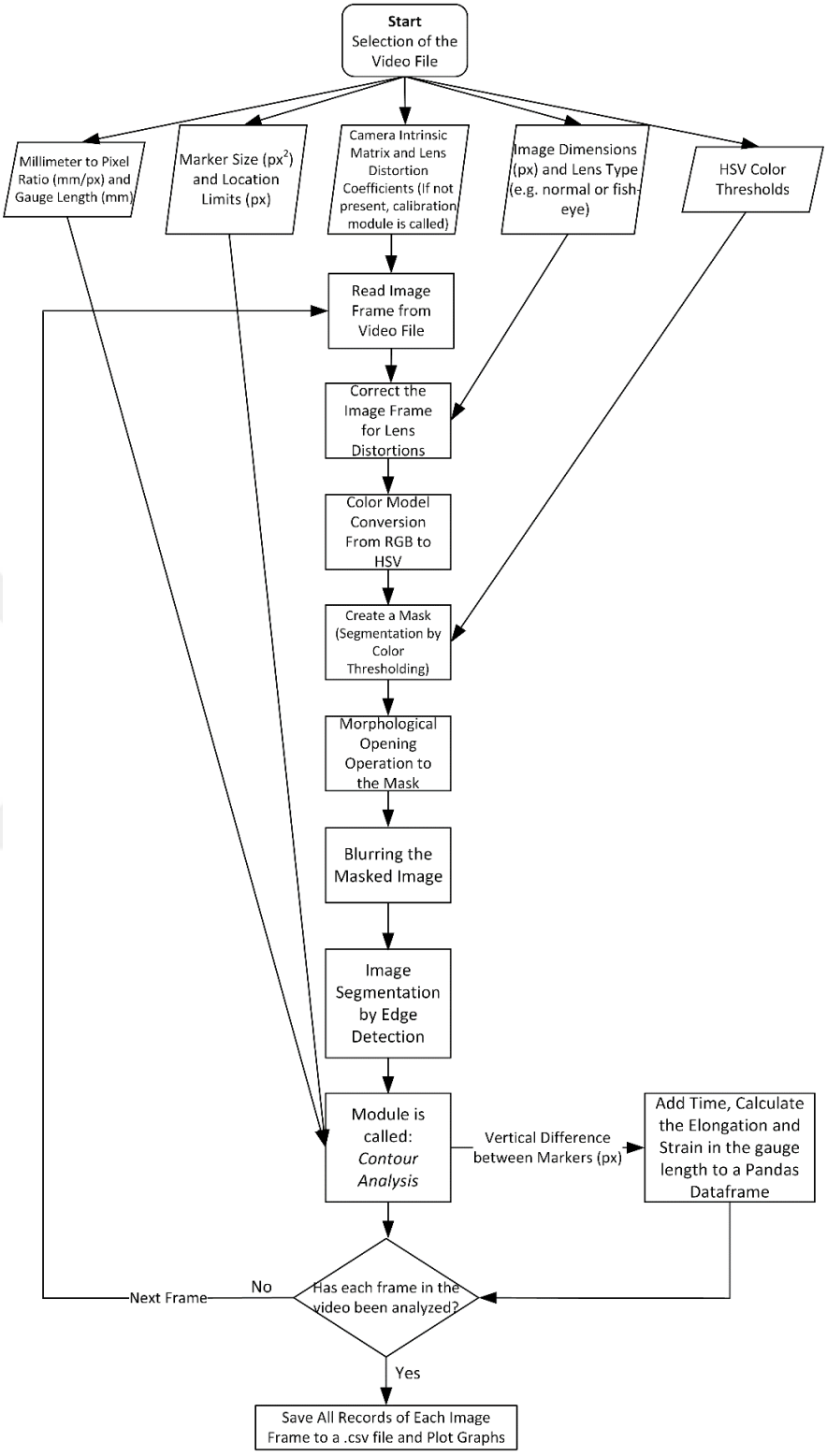

Figure 3.7. Main Program Flow.

3.4.3 Color Thresholding

A color can be represented in various color models. These models are coordinate systems in which a point represents each color. Some well-known models are the CMYK (cyan, magenta, yellow, black), used for printers, and the RGB (red, green, blue) for cameras, monitors, and displays. These models represent color images as proportions of primary colors. Therefore, they are ideal for use in machines.

However, humans do not perceive colors as proportions of the primary colors. When describing an object's color, we do not provide its red-green-blue proportions. On the other hand, the HSV model closely approximates how humans perceive color. As its name implies, the hue, saturation, and brightness of an object's color generally differentiate it from the surrounding environment in our perception. Additionally, separating color (hue) from intensity (saturation and value) makes it easier to use greyscale processing techniques, which are widely used in digital image processing (Gonzalez & Woods, 2002). Inspired by the applications in other research areas, this study employs the HSV color model to set color thresholds, enabling the identification of color markers drawn on specimens.

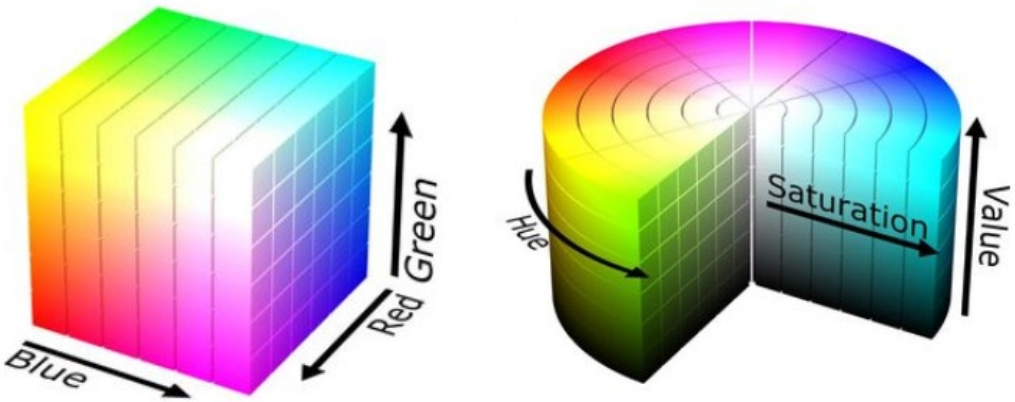

(a) (b)

Figure 3.8. Schematic plots of (a) RGB, (b) HSV color models (Bradski, 2000).

Since images are initially represented in the RGB model by cameras and computers, a conversion from RGB to HSV is required. In the HSV color model, the hue designates the spectral wavelength. Red, green, and blue have separate wavelengths found at 0°, 120°, and 240°, respectively, as shown in Figure 3.8b. Saturation reaches its maximum at the circle's periphery, indicating pure color. As white dilutes the pure color, the saturation decreases. On the other hand, the value represents pixel intensity (brightness) and is independent of hue and saturation. It can distinguish bright or high-intensity areas from dark or low-intensity regions (Castleman, 1996).

The proposed technique employs the HSV color conversion routine provided by OpenCV. It creates a binary mask by setting thresholds for the color markers' hue, saturation, and value properties. If the color's hue, saturation, and value fall within the specified thresholds, the corresponding mask value is set to True; otherwise, it is False. This mask is applied to the original image, resulting in an image containing only the color markers, as shown in Figure 3.9c.

In the current version of MBDT, determining the threshold limits requires user input. It is crucial to note that the limits directly impact the technique's robustness and should be selected to remain consistent throughout the tests. Since the position of the markers changes with specimen deformation, causing variations in illumination, it is recommended to set thresholds using multiple image frames from the beginning to the end of the test.

The HSV color model code used in the MBDT technique takes an input image and allows users to manually define the best thresholds by specifying the minimum and maximum limits for each hue, saturation, and value parameter. Figure 3.9 shows successful color thresholding, resulting in a nearly perfect mask. The ideal mask should effectively separate the paint markers from other objects in the frame. However, images may contain noise or other things with similar colors to the markers, which could be reflections caused by shiny or polished surfaces of laboratory equipment, as shown in Figure 3.10. Ensuring a black background and covering shiny surfaces contribute to the success of color thresholding, as depicted

in the figures. A compromise must be reached to cover an adequate field of view, eliminating environmental noise while maintaining the specimen's visibility when it experiences high strain before rupture.

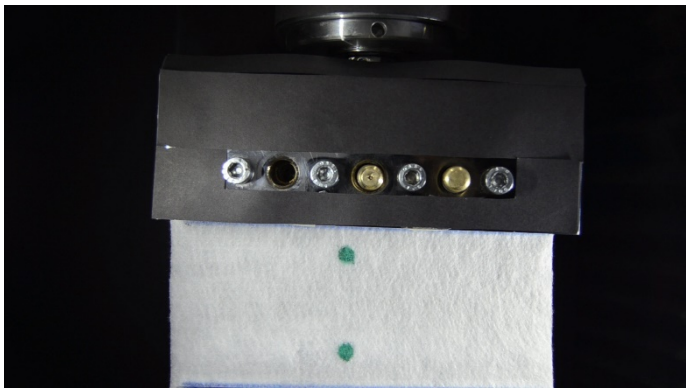

(a)

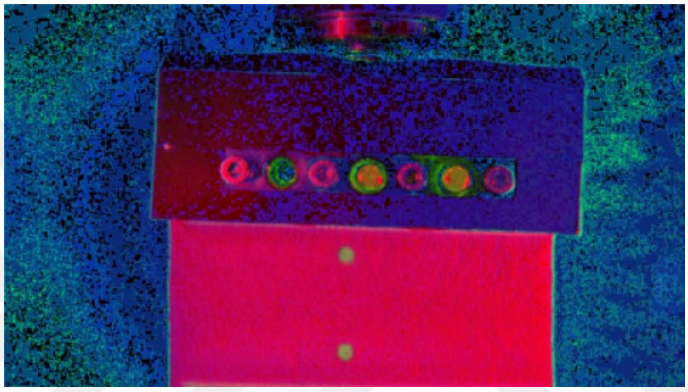

(b)

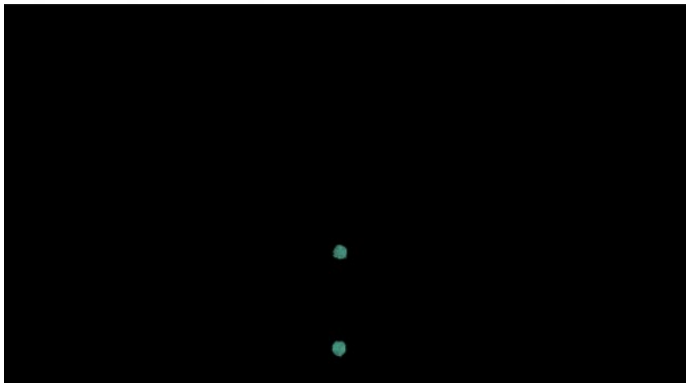

(c)

Figure 3.9. HSV color thresholding for the geotextile specimen. For avoiding light reflections from polished surfaces, the wedge grips are covered with matte black color, and a black cardboard is placed on the background. (a) Original RGB image. (b) The image is converted from RGB to HSV. (c) The masked image after setting the color threshold limits.

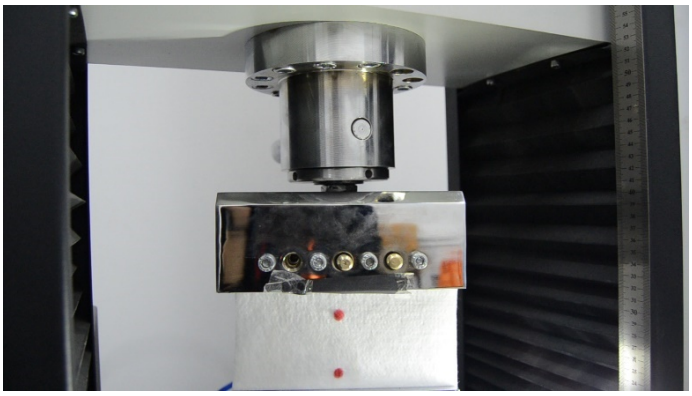

(a)

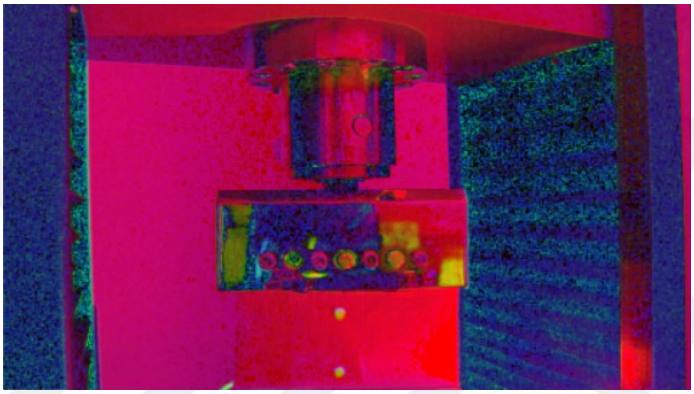

(b)



(c)

Figure 3.10. Color thresholding resulted in incomplete masking of color markers. A noisy image was obtained due to reflections of marker colors from the shiny surface of the wedge grips. (a) Original RGB image. (b) HSV image. (c) The masked image after the threshold limits are set.

3.4.4 Edge Detection

Edge detection is a process that aims to identify whether a pixel is located at the boundary of an object or not. Edge detection algorithms generally examine the pixels and their neighbors to measure the light intensity gradient and direction (Castleman, 1996).

Edge detection on masked images, such as those shown in Figure 3.9c and Figure 3.10c, is crucial in detecting the color markers drawn on specimens. This study utilizes the Canny Edge Detection algorithm (Canny, 1986), readily available in OpenCV. The algorithm takes a slightly blurred input image. The purpose of blurring is to avoid detecting sharp changes in pixel intensities caused by local variations in lighting. This blurring allows the algorithm to focus on identifying significant intensity changes corresponding to actual object boundaries rather than detecting minor fluctuations in lighting conditions.

Figure 3.11 illustrates the steps employed to achieve edge detection. Firstly, RGB colors are converted to HSV colors (Figure 3.11b). Then, a binary mask is created based on the HSV color thresholds set by the user (Figure 3.11c). The mask is then applied to the original image, resulting in the masked image (Figure 3.11d). The masked image is blurred to avoid detecting sharp changes in the color intensities. Finally, the Canny algorithm is used to detect the edges of the drawn paint markers (Figure 3.11e). The next step, the identification of the markers, will be explained in detail.

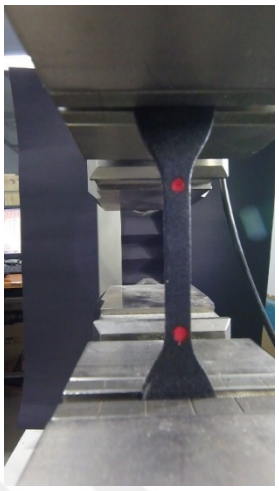

(a)

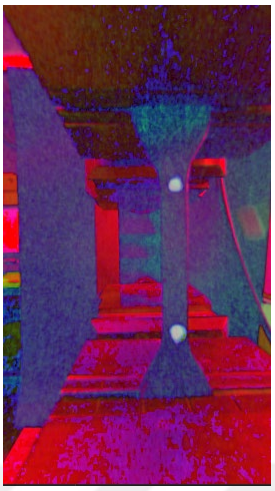

(b)

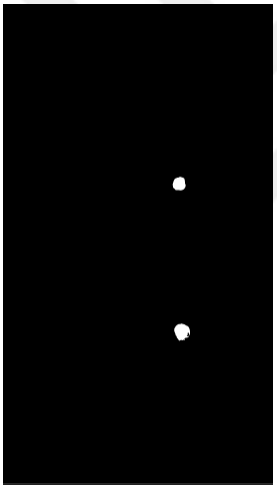

(c)

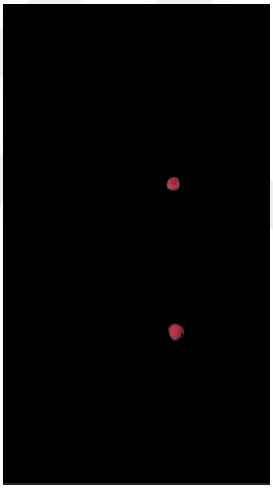

(d)

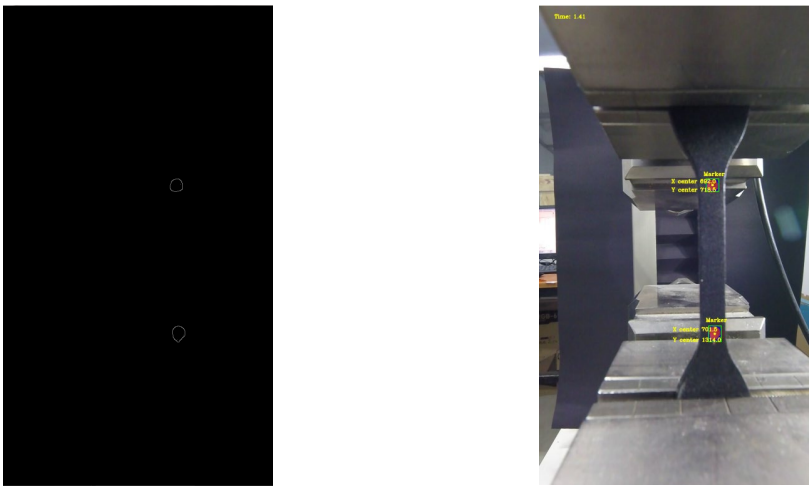

(e) (f)

Figure 3.11. Step-by-step color marker detection by image segmentation. (a) Original RGB image. (b) RGB is converted to HSV. (c) A binary mask is obtained after setting the color threshold limits. (d) Masked image, blurred to some extent. (e) Edges of the markers detected by the Canny algorithm. (f) Successfully detected markers shown on the original image by bounding boxes and their coordinates in pixels.

3.4.5 Analysis of Contours

A contour is defined as a closed loop of edges, and each contour is considered as a potential marker. However, specific criteria must be established to differentiate markers from other objects in the field of view. This section explains the followed classification criteria. The flowchart of contour analysis is depicted in Figure 3.12.

Even if markers are circle-like at the beginning of a test, their shape may deviate from a circle during the test and instead approach an ellipse. Therefore, the markers are approximated by polygons with a certain number of corners. A polygonal contour must have sufficient corners to be considered a marker. However, additional criteria are necessary to enhance the technique's robustness, as noise or other objects may also form closed loops with multiple corners. In addition to the contour analysis

routine provided by OpenCV, two additional criteria are established to qualify as accurate contours.

i. Marker Size

A bounding box is drawn around one of the markers on the image to prevent small noises from being falsely identified as markers, as demonstrated in Figure 3.13b. This bounding box acts as a size limit, ensuring only markers above a specific size are valid. As the tensile testing progresses, the size of the markers may change; thus, the minimum value of the initial marker size is utilized as the size limit criterion.

ii. Marker Location

The markers' location is considered in addition to their size to ensure accurate identification of markers and prevent noises from being mistakenly classified. This is achieved by utilizing the location information from the bounding box drawn to determine the marker size, as depicted in Figure 3.13b. Considering the box's corners, the horizontal coordinates of the top-left and bottom-right corners are used as the horizontal boundaries. Since the vertical alignment of the markers remains consistent throughout the test, the location limits are set to ensure that only the markers within the specified vertical range are correctly identified, even in the presence of noises in the image frame.

Figure 3.12 shows the flowchart of the Contour Analysis. Once an image frame is segmented using HSV color threshold limits and edge detection, the Contour Analysis program module is invoked. This module inputs a Canny image, showing only the visible edges (Figure 3.11e). All edges are analyzed, then the ones forming a closed loop are classified as contours. They are further examined based on their size (area) and location.

The set of criteria for marker detection can be summarized as follows:

- Since a straight vertical line represents the gauge length, the markers are expected to be aligned vertically. This implies that the horizontal coordinates of the markers should either coincide or be very close to each other. To ensure accurate identification of markers, users must provide location input, specifying the expected vertical alignment of the markers. This prevents any other contour from being mistakenly identified as a marker.
- The marker area in pixels can be provided as input to avoid mistakenly identifying noises as markers. This size, determined from the undeformed specimen image, is the minimum marker size. Since the marker size is expected to increase continuously as the specimen elongates during the test, any contour with an area smaller than the specified marker size will be disregarded as noise and not classified as a marker.
- The detection of only two markers on an image is necessary because they represent the start and end points of the gauge length, which should form a straight line (as shown in Figure 3.1). If more than two contours are classified as markers on the same image frame, it indicates an incorrect identification. In such cases, the frame is discarded to ensure accurate tracking of the gauge length.

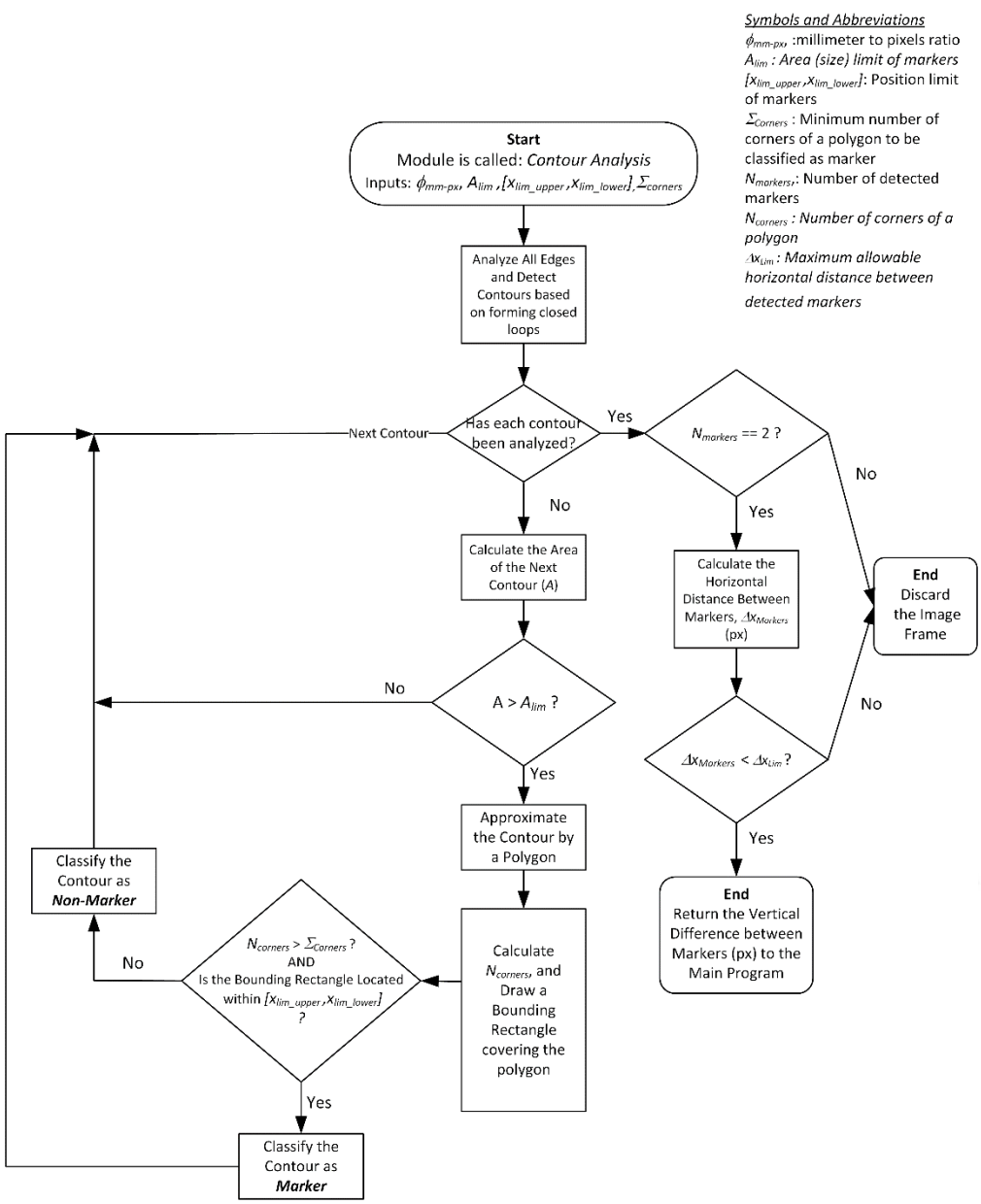

Figure 3.12. Flowchart of the Contour Analysis module.

3.4.6 Calculation of Strains

The MBDT technique tracks the displacement of color markers over time, allowing for continuous displacement monitoring. Under the assumption of a uniform strain distribution, valid unless the specimen undergoes yielding and experiences highly localized and inhomogeneous strains, the strains can be calculated using MBDT. The strains are determined by dividing the elongation of the gauge length by the initial distance between the markers. This provides a quantitative measure of the deformation or stretching experienced by the specimen during the testing process.

Once the markers have been successfully detected through image segmentation, their location change is tracked to monitor the elongation of the gauge length. The gauge length's elongation can be continuously monitored by measuring the markers' displacement throughout the testing process. The elongation is divided by the initial gauge length to quantify the strain, representing the specimen's deformation or stretching.

Using a conversion ratio, the image units (pixels) should be mapped to real-world units (millimeters). The user determines this ratio, known as the millimeters-to-pixels ratio. They can input this ratio by drawing a box that covers the gauge length on an image displaying the specimen's initial (undeformed) state (Figure 3.13a). The millimeters-to-pixels ratio can be calculated by establishing the correspondence between the known gauge length in millimeters and its representation in pixels. This ratio allows for converting pixel-based displacements to real-world units, enabling the determination of strains in millimeters per millimeter or any desired unit.

If the vertical coordinates of the markers are denoted by y_1 and y_2, and the millimeters-to-pixels ratio by ϕ.

$$L_i = |y_2 - y_1| * \varphi$$

$$\Delta L = L_i - L_0$$

$$\varepsilon = \frac{\Delta L}{L_0}$$

L_i is the instantaneous gauge length, L_0 is the initial gauge length, and ΔL is the elongation or the change in the gauge length. Finally, the strain, ε, is obtained.

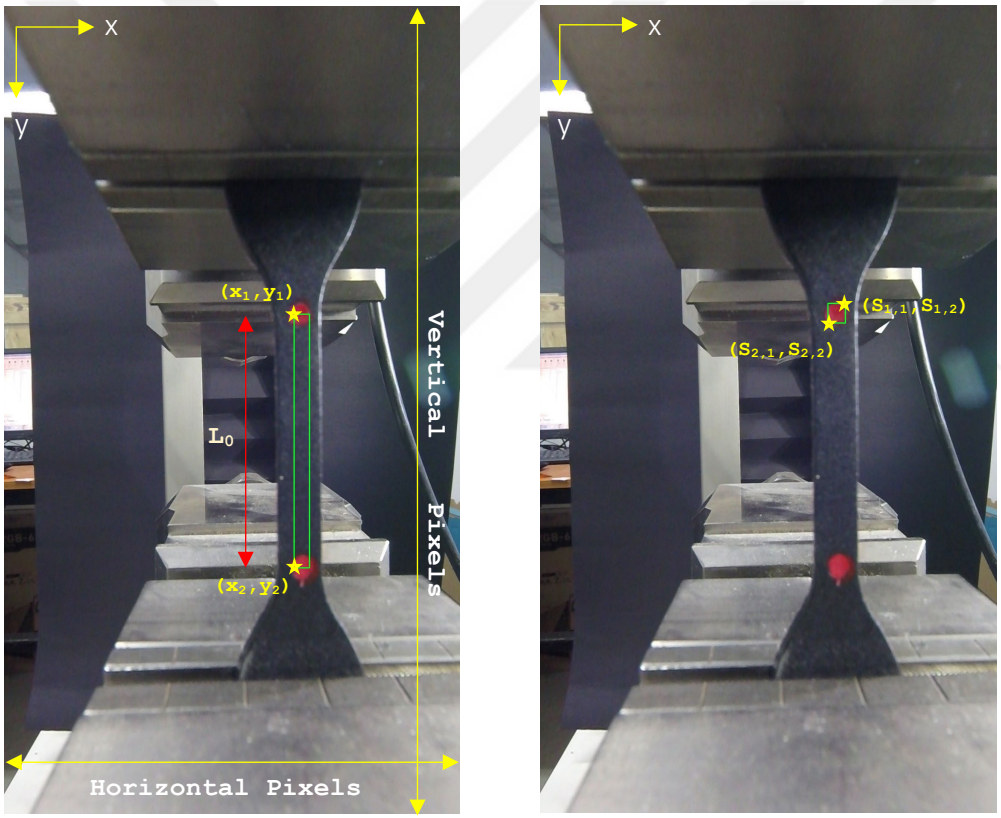

(a) (b)

Figure 3.13. (a) Users are prompted to draw a box to indicate the gauge length. (b) Marker location limits on the x-axis and the minimum marker size are set by drawing another bounding box.

3.5 Strain Measurement by Digital Image Correlation (DIC)

The Digital Image Correlation (DIC) technique is widely used in tensile testing. It is recognized as one of the most commonly employed image-based techniques, as depicted in Figure 2.2a (Baldner et al., 2020). DIC differs from the Marker-Based Displacement Tracking (MBDT) technique in providing a continuous displacement and strain distribution for the specimen's entire region of interest (RoI).

DIC relies on capturing and analyzing the variations in light intensity on the specimen's surface. A unique and identifiable pattern, such as random speckles, is applied to the RoI to create these variations. The pattern introduces distinct light-intensity features that serve as markers for tracking the deformation of subsets within the image. By tracking the displacements of these subsets, strains can be calculated by performing spatial differentiation of the subset displacements.

In contrast, the MBDT technique focuses on tracking the displacement of specific color markers placed on the specimen. It provides a continuous measurement of the elongation of the gauge length but does not offer the same level of spatial resolution and continuous strain distribution as DIC. MBDT is particularly suited for scenarios where a uniform strain distribution is assumed, and the focus is on monitoring the elongation of a specific gauge length.

Both techniques have their advantages and applications. DIC is more suitable for capturing detailed strain distributions over larger regions, while MBDT is effective for monitoring specific markers and the elongation of the gauge length. The choice between the two techniques depends on the experiment's requirements and the desired strain measurement level.

This study implements an open-source DIC software, Ncorr (Blaber et al., 2015), as a reference image-based technique to validate MBDT. Below, the workflow of Ncorr is summarized.

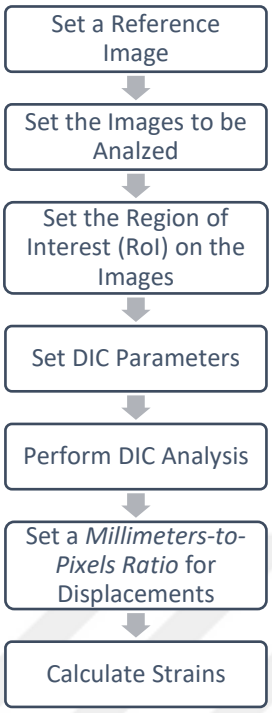

Figure 3.14. The program flow of Ncorr software (Blaber & Antoniou, 2017).

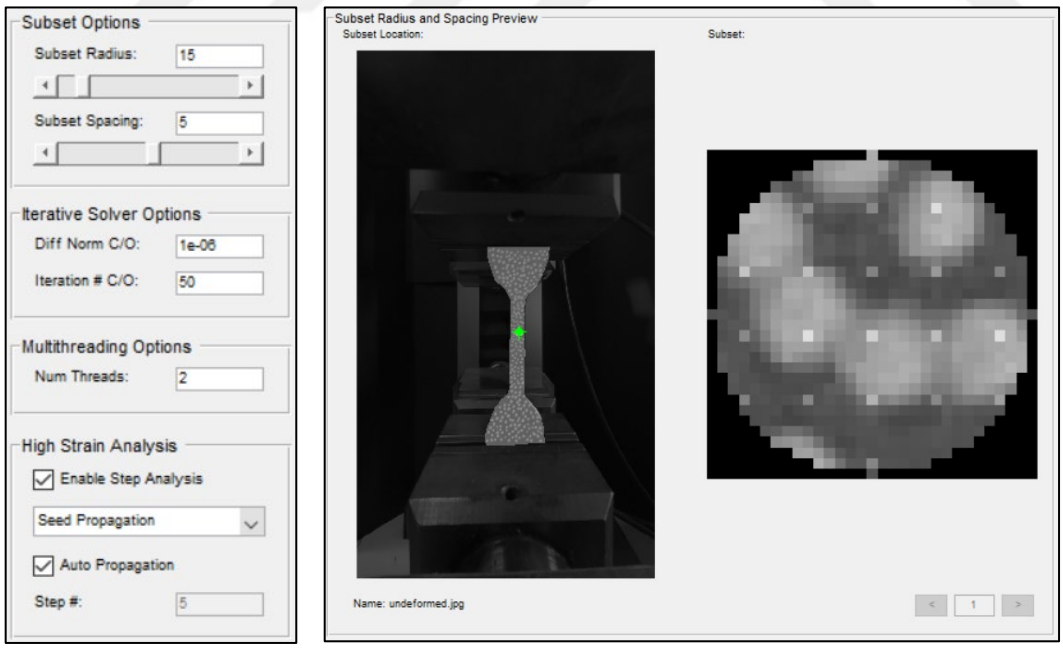

(a) (b)

Figure 3.15. Adjustment of DIC analysis parameters using Ncorr software.

The analysis in DIC is based on the gray-level light intensities of subsets, which are finite representative parts of the image, as shown in Figure 3.15b. The selection of an appropriate subset radius is crucial for achieving accurate correlations. The spacing between subsets also plays a role as it affects the number of calculations required, and using large spacing may decrease the precision of the calculations. Additionally, the parameters of the iterative solver can be adjusted. For example, the maximum number of iterations can be increased if the user wants to check if the solution converges in subsequent iterations.

In DIC analysis, there is an option to select the *high-strain analysis* function, which may be suitable for geosynthetics with a high strain capacity before rupture. Sometimes, if this option is not specified, the solutions may not converge after reaching certain strain limits. Hence, it is essential to consider this function when analyzing high-strain materials. However, it should be noted that accuracy may decrease as the reference image is constantly updated.

It should be noted that the speckles on the specimen must remain identifiable throughout the testing process. If the specimen undergoes necking after yielding, some speckles may become distorted, making it difficult for the DIC algorithm to converge to accurate solutions for those points. Therefore, DIC analyses on geomembranes were typically performed until yielding, ensuring reliable and consistent results.

The proper placement of *seeds* is crucial for successful correlations in DIC. Seeds serve as the initial guesses for displacement solutions and help partition the images during parallel computations. According to the recommendation Blaber & Antoniou (2017), the seeds should be located in areas where displacements are highest.

In Figure 3.16a, where two processor cores are used, two seeds are placed strategically to ensure accurate displacement calculations. The correlation algorithm can better capture the displacement field and provide more reliable results by placing the seeds in regions with high displacement gradients or areas prone to large deformations. This approach helps optimize the correlation process and enhances the

accuracy of the DIC analysis. Two seeds are placed when two processor cores are in use.

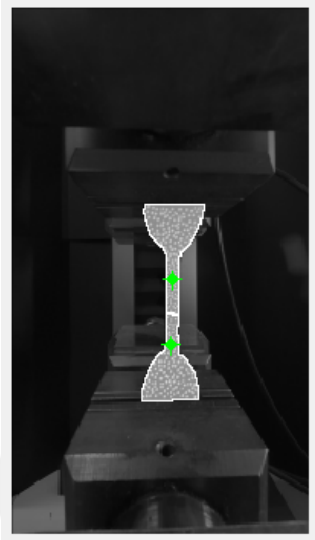

(a)

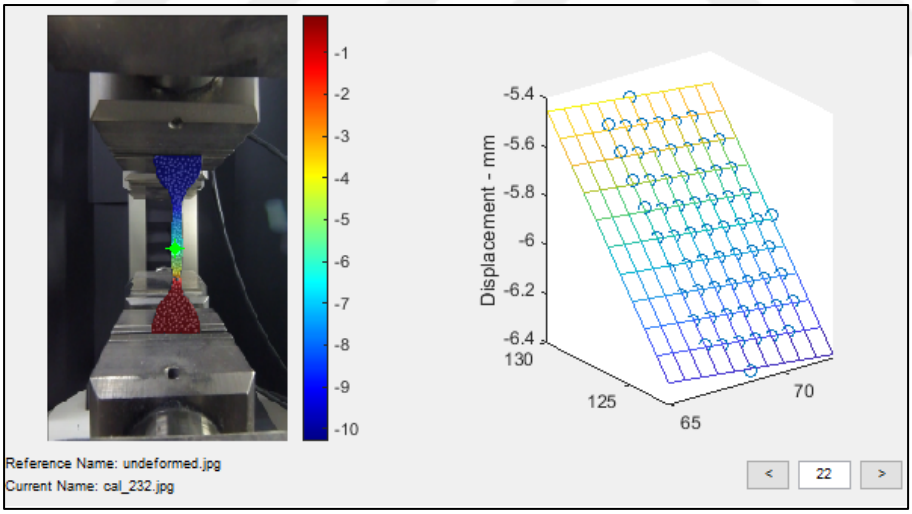

(b)

Figure 3.16. Miscellaneous steps of the DIC analysis. (a) Location of seeds. (b) Fitting a plane to displacements for strain calculation.

Like MBDT, the DIC technique requires a ratio to convert pixel units to real-world units such as millimeters. This ratio can be obtained by inputting a reference length measurement, typically achieved by drawing a line on the reference image.

To calculate strains using DIC, the user must input the strain radius. The strain radius represents the radius of a circle that fits a plane to a group of displacement values within a subset. It is recommended in the user manual to set the strain radius for areas of high deformation appropriately. It is generally preferable to use the smallest radius possible to minimize the introduction of noise in the strain calculations unless larger radii are necessary to capture the full extent of deformation in some areas of interest.

By accurately defining the strain radius and selecting appropriate areas of analysis, the DIC technique can provide reliable and meaningful strain measurements for the specimen under investigation.

After evaluating the results of DIC analysis, a more comprehensive understanding of geosynthetic deformation can be obtained. As illustrated in Figure 3.17, the DIC technique provides continuous displacement and strain measurements throughout the specimen.

In the subsequent chapter, the DIC technique will be utilized to validate the strains calculated by the newly proposed MBDT technique. By comparing the results obtained from both techniques, a comparative analysis can be conducted to assess the accuracy and reliability of the MBDT technique in capturing the deformation behavior of geosynthetics.

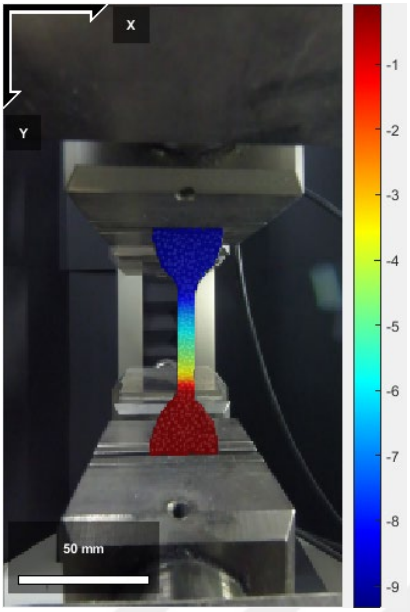

(a)

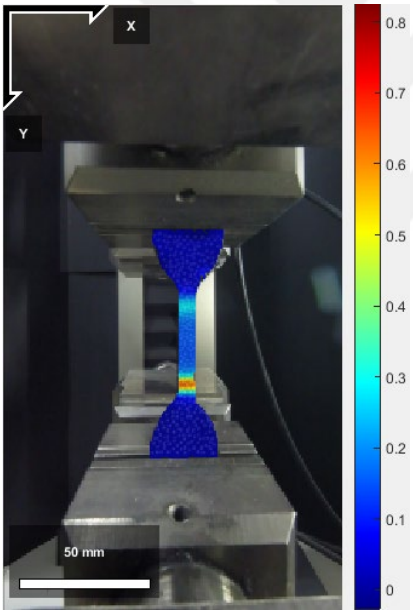

(b)

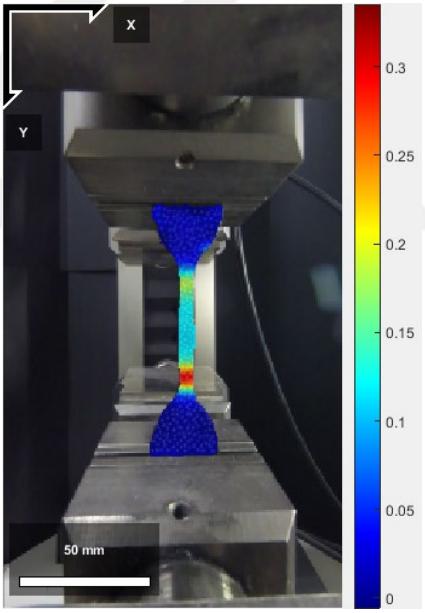

(c)

Figure 3.17. DIC analysis results of a geomembrane sample prior to yielding. (a) Displacements (mm). (b) Lagrangian-Green strains. (c) Eulerian-Almansi strains.

CHAPTER 4

GEOSYNTHETIC TESTS WITH MBDT

By performing tensile tests on geosynthetics, this chapter aims to provide strain results of the newly presented Marker-Based Displacement Tracking (MBDT) technique. The results are subsequently compared to strains inferred from Digital Image Correlation (DIC) and Crosshead Displacement to validate MBDT's adoption for research purposes. The tests followed the guidelines of corresponding ISO and ASTM standards. The technical properties of laboratory setup; including the camera and the testing machines, and material properties of the tested samples are briefly reported. Validation test results are visualized through related graphs, and error calculations are provided.

4.1 Tensile Testing Setup

The test setup consists of a universal testing machine (UTM), a video camera, LED light sources, and a tripod. Two UTMs were employed to test the technique's effectiveness and evaluate its reliability across different test machines and equipment.

4.1.1 Universal Testing Machine (UTM)

Two different testing machines used for the tests, are shown in Figure 4.1. The 10 kN-capacity machine (Zwick Roell Z010) was utilized for testing of geomembranes, while the 100 kN-capacity machine (Pekon MTM-ProV10) was utilized for testing of geotextiles and geosynthetic clay liners (GCL). Table 4.1 presents the key technical specifications of the machines.

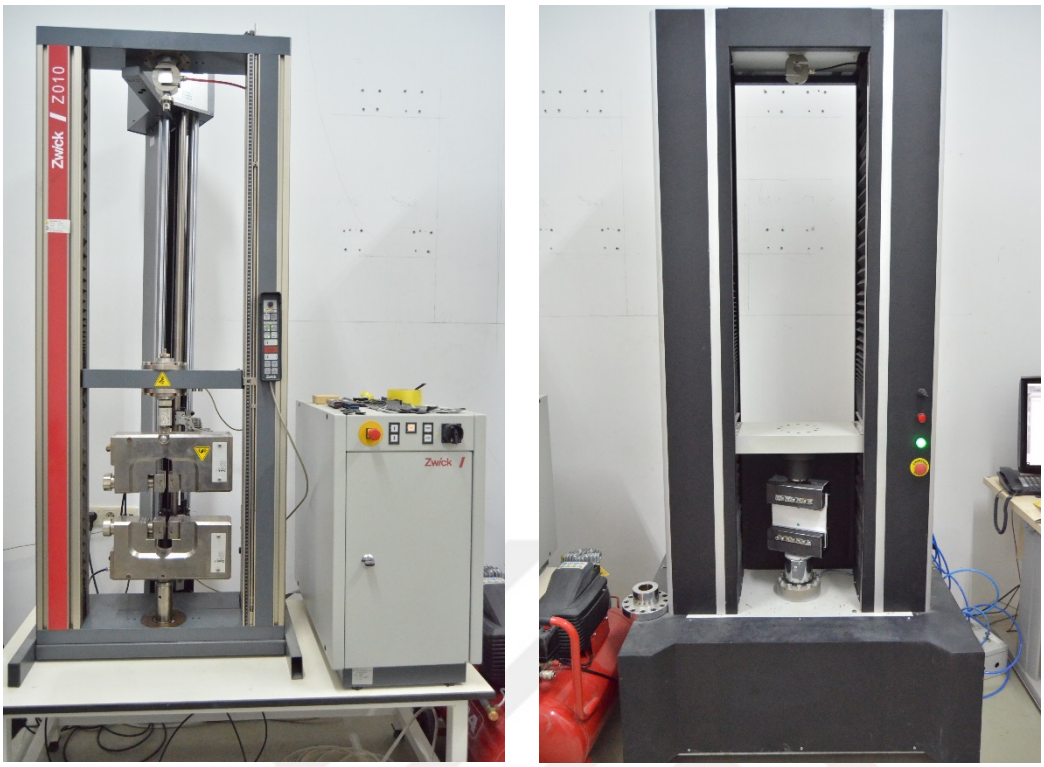

(a) (b)

Figure 4.1. Universal Testing Machines used in this study. (a) Zwick Roell Z010, with pneumatic grips. (b) Pekon MTM-ProV10, with mechanical wedge grips.

Table 4.1. Key technical properties of the Universal Testing Machines.

UTM ID	UTM-A	UTM-B
Brand & Model	Zwick Roell Z010	Pekon MTM-ProV10
Motor	AC Servo Motor	AC Servo Motor
Max. Load Cap. (kN)	10	100
Materials Tested	Geomembrane	Geotextile, GCL
Gripping Force	Pneumatic	Mechanical
Test Software	TestXpert v.12	Built-in Software
Year of Manufacture	1998	2022

4.1.2 Camera

Table 4.2. Key technical properties of the cameras used in this study.

Camera ID	Cam-1	Cam-2
Camera Brand & Model	GoPro Hero 4 Session	Nikon D5100
Focal Length (mm)	3	18-55*
Aperture Size (f-stop number)	f/2.8	f/5.6-3.5*
Maximum Frame Size (px) - Rate (fps)	2560 x 1440 - 30	1920 x 1080 - 30
AutoFocus	Not Available	Available

*The Nikon D5100 is equipped with a zoom lens, and the values represent the maximum and minimums (i.e., focal length can be adjusted to an intermediate value between 18 and 55 mm).

Table 4.2 presents the key technical properties of the video cameras used in this study. Cam-1 (GoPro Hero 4 Session) is known for its tiny size and fixed fisheye lens, allowing it to fit anywhere and capture a wide field of view without needing to adjust any lens configuration. On the other hand, Cam-2 (Nikon D5100) is a more professional camera that offers greater flexibility as nearly all adjustments can be made to capture the best image possible, making the imaging process more challenging yet flexible.

Following a review of the literature, little was found regarding the use of a fisheye (ultra-wide-angle) lens camera, such as Cam-1, for strain measurement based on images. These cameras introduce significant lens distortion to images, which must be corrected through calibration. However, their small size provides a notable advantage when measurements need to be taken in confined spaces where larger cameras cannot fit, such as the case shown in Figure 4.2a. Additionally, using a

fixed-lens camera, such as Cam-1, eliminates the need for calibration before each test session. This practically makes it highly suitable for conducting a series of tests without repeating the camera calibration process. Since the camera matrix and lens distortion coefficients are known in advance and remain unchanged from one test to another, distorted images can be directly corrected.

Moreover, an ideal camera for image-based strain measurement should capture a field of view, particularly considering the anticipated high strains. Merely covering a broad field of view is insufficient; and bright images are crucial as color image processing requires great lighting.

Due to fulfilling the requirements above, Cam-1 was employed for all tensile tests conducted in this study. However, Cam-2 was also utilized to validate the camera calibration process for normal (zoom) lenses.

4.1.3 Auxiliary Equipment

Figure 4.2 shows the auxiliary equipment used in the study, including a tripod, LED light sources, and black cardboard. The need for the light sources became apparent after a few trials, where natural lighting in the laboratory resulted in insufficient color balance for image segmentation through color thresholding. As a result, additional illumination was provided by two LED light sources. LED lights were preferred due to their strong illumination capability without generating significant heat on the specimens. A black cardboard was placed behind the test grips to enhance the light sources' illumination effectiveness and prevent any undesired noise appearing in the image frame.

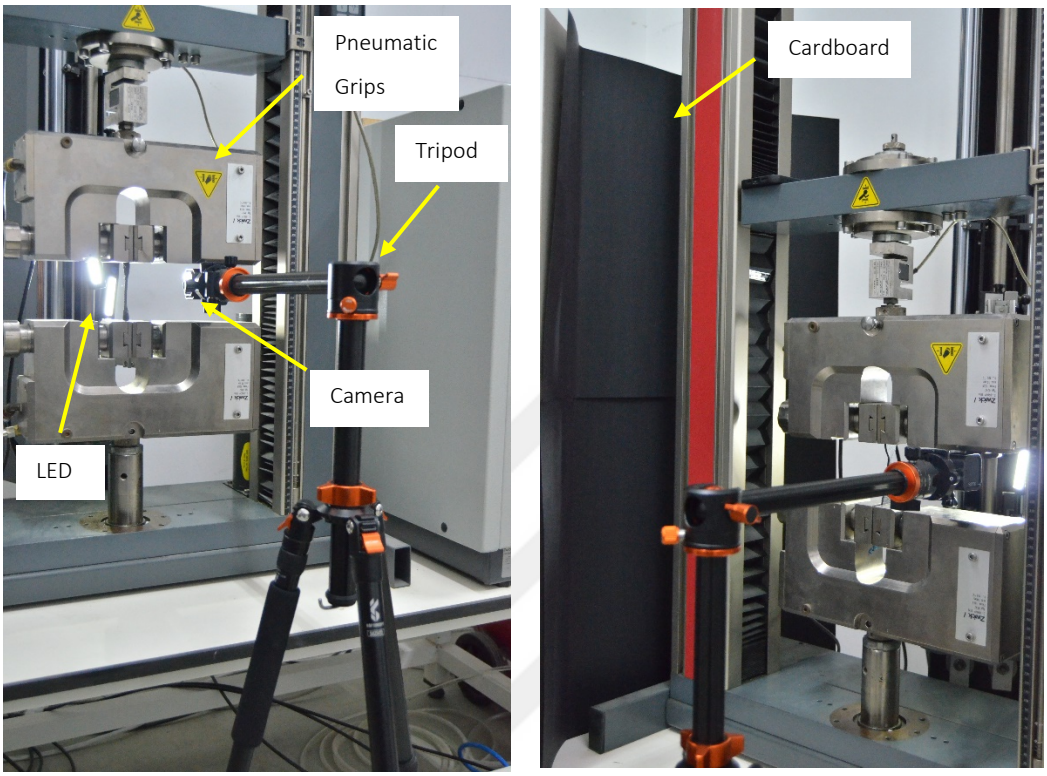

(a) (b)

Figure 4.2. Auxiliary equipment used in the test setup. (a) LED light sources behind the grips to provide sufficient illumination. (b) Black cardboard on the background to avoid noise in the images.

4.2 Validation of MBDT

Validation of the newly presented MBDT technique is crucial to verify its robustness and accuracy for geosynthetics testing. Table 4.3 summarizes the validation methodology and test plan.

Table 4.3. Summary of validation test plan, with equipment, materials, and validation techniques.

	Validation of Camera Calibration		Validation of Strain Calculation		
Test Group ID	CC-1	CC-2	T-GMB	T-GTX	T-GCL
Number of Tests	1	1	12	12	12
Material Type	-	-	HDPE Geomembrane	Non-Woven Geotextile	-
Camera	Cam-1	Cam-2	Cam-1	Cam-1	Cam-1
Image Size (h x v) (px)	1080 x 1920	1920 x 1080	1080 x 1920	1080 x 1920	1080 x 1920
UTM	-	-	UTM-A	UTM-B	UTM-B
Test Speed (mm/min)	-	-	50	20, 10	20, 10
Validation Technique	MATLAB Camera Calibrator App		DIC, Crosshead Displacement		

4.2.1 Validation of Strains

As inferred from Table 4.3, validation tests comprise three different types of geosynthetics: (i) geomembrane, (ii) geotextile, and (iii) GCL. The first test group consisted of smooth and one-sided textured HDPE geomembrane samples with a thickness of 1.5 mm, which were tested using UTM-A. The second test group includes non-woven geotextile samples with the masses per unit area of 300, 400, and 600 g/m^2, tested using UTM-B. The last group involves GCL samples cut from one material type. Due to its practical advantages, Cam-1 (GoPro Hero Session 4) was utilized as the capturing device for all test groups.

The MBDT technique developed in this study tracks the displacements of markers with time. These markers are placed at the start and end points of a desired gauge length, as described in Chapter 3.1. Elongation is quantified by the increase in the distance between the markers, while strain is calculated by dividing the elongation (i.e., the change in gauge length) by the initial gauge length.

The Crosshead Displacement technique assumes that the specimen elongates by the same amount as the UTM crosshead travel distance during a test. Strain is calculated by dividing the crosshead travel distance by the initial gauge length. The gauge length is typically defined by relevant standards or assumed to be the same as the initial distance between grips, which is called the nominal gauge length.

The DIC technique relies on comparing the current visual state of a sample, with the initial state. This is achieved through partitioning the image into subsets and establishing correlations between them, which are tracked based on their unique light intensity. With that, continuous strain distribution within a desired region of interest (RoI) can be found. Consequently, the gauge length becomes inconsequential as the entire RoI is inspected.

In this section, a comparison is made between the strains obtained using the MBDT technique and those calculated using the DIC and Crosshead Displacement

techniques. To provide a quantifiable approach to compare the techniques, Mean Absolute Error (MAE) and Root Mean Square Error (RMSE) are computed.

4.2.1.1 Testing of Geomembranes

Two geomembrane types were used to validate the MBDT technique for tensile testing of geomembranes: (i) 1.5-mm smooth and (ii) 1.5-mm one-sided textured HDPE geomembranes. A total of 12 samples were tested. The key material properties of the samples are provided in Table 4.4. It is important to note that the validation tests on geomembrane samples focused solely on strains up to yielding. Beyond yielding, the geomembrane strains become highly non-uniform, which contradicts the assumption of uniform strains within the gauge length made by the MBDT technique. Furthermore, determining strains after yielding was not possible using the DIC technique employed in this study, as the optical correlation between image subsets was lost due to the disruption of speckles.

The tests were carried out following ASTM D6693 guidelines. The test speed was set to 50 mm/min, and the grip-to-grip distance was 65 mm. Strain calculations are performed using the Crosshead Displacement technique. Strain measurements at yielding and the point of breakage are based on different gauge lengths. In summary,

a) Strain at yielding, $\varepsilon_y = \frac{\Delta L_{CT}}{L_0}$, where L_0 is the gauge length prior to yielding (L_0 = 33 mm), and ΔL_{CT} is the crosshead travel distance.

b) Strain at break, $\varepsilon_t = \frac{\Delta L_{CT}}{L_0}$, where L_0 is the gauge length after yielding until rupture (L_0 = 50 mm), and ΔL_{CT} is the crosshead travel distance.

The strain measurement techniques employed to validate the MBDT technique for testing of geomembranes are explained in detail below.

i. *MBDT:* Two color markers are placed on geomembrane samples to indicate the start and end points of the gauge length for yielding (L_0=33 mm. The elongation in the gauge length is found by measuring the increase in vertical distance between these markers. The elongation is divided by the yielding gauge length (L_0) to calculate the strain.

ii. *DIC:* The strains computed for the whole region of interest (e.g., Figure 4.4b) are utilized by taking the average strains within the center of the specimen covering the gauge length (L_0 = 33 mm). If the strains localize to a point before reaching yielding, then the sample is discarded, and strains are not compared to those obtained from the MBDT technique.

iii. *Crosshead Displacement:* As explained, it is assumed that the sample elongates uniformly within the gauge length, corresponding to the same amount of crosshead travel until yielding occurs. This assumption allows for calculating strains by dividing the crosshead travel distance by the initial gauge length.

Table 4.4. Key physical and mechanical properties of the geomembrane samples. Technical specification limit values are indicated in square brackets.

	GMB-Type 1	GMB-Type 2
Material	HDPE	HDPE
Number of Samples	3 (MD) + 3 (CMD)	3 (MD) + 3 (CMD)
Thickness (mm) - Texture	1.5 - Smooth	1.5 - One-Sided Textured
Density (g/m^3)	0.941 [0.940 – 0.970]	0.941 [0.940 – 0.970]
Yield Strength, MD/CMD (kN/m)	27.8 / 26.6 [>23.0 / >23.0]	26.4 / 26.6 [>23.0 / >23.0]
Static Puncture Strength, CBR (kN)	4.4 [>3.8]	5.4 [>3.8]

Figure 4.3a displays one of the test samples featuring color markers and speckles. Following ASTM D6693, red and blue markers are placed, designating the gauge length for yielding and break, respectively. Figure 4.3b shows the sample while it is being tested within pneumatic grips. The displacement and strain fields prior to yielding are depicted in Figure 4.4a and Figure 4.4b, produced using DIC. Especially, Figure 4.4b illustrates the uniform distribution of strain within the yielding gauge length (L_0=33mm). Figure 4.4c demonstrates the utilization of red markers when employing the MBDT technique.

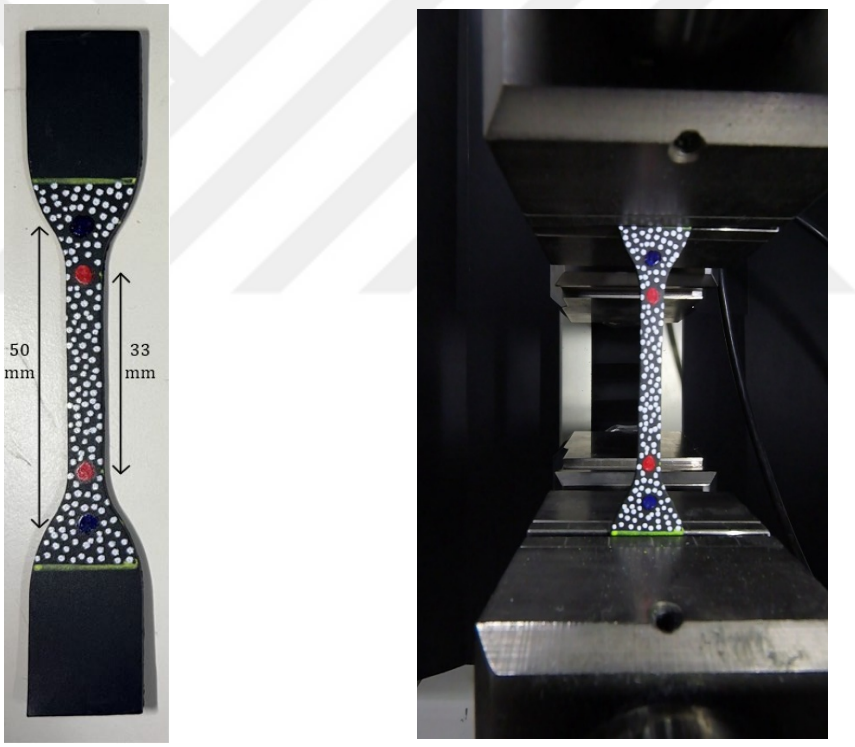

(a) (b)

Figure 4.3. (a) GMB - Type 1 test sample with color markers designating the gauge lengths (L_0 = 33 mm and 50 mm) and speckles drawn for the DIC technique. (b) The pneumatic grips are testing the sample. A black cardboard is placed in the background to avoid undesired noise appearing in the scene.

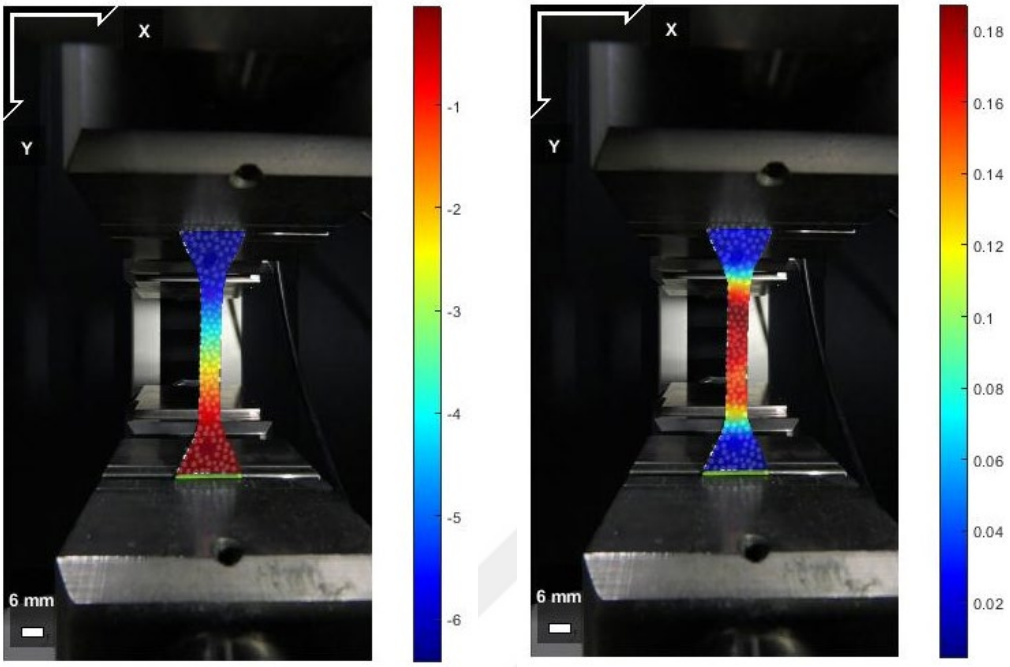

(a) (b)

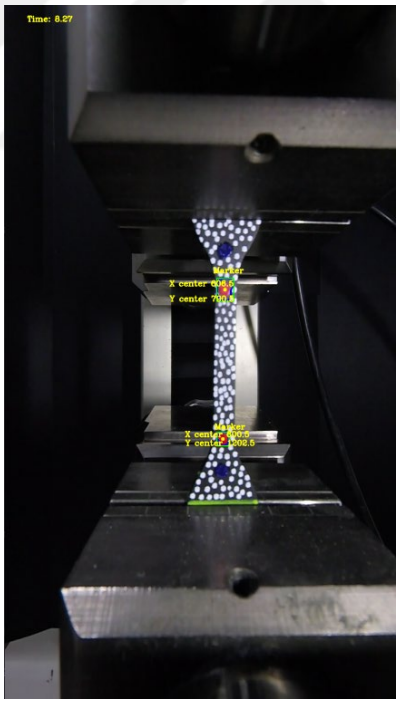

(c)

Figure 4.4. Different image-based techniques are in use for the geomembrane sample (T-GMB_1). (a) DIC, displacement distribution heat map (mm). (b) DIC, strain distribution heat map (Lagrangian-Green). (c) MBDT.

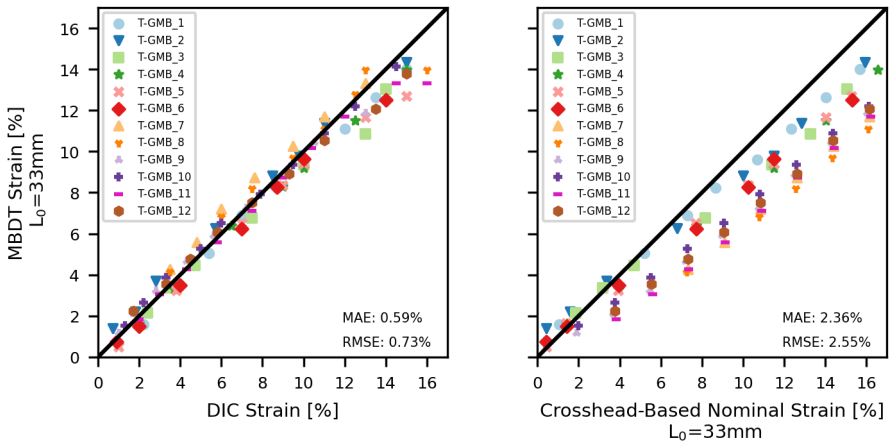

Figure 4.5. For each test, strains by MBDT are compared with DIC and Crosshead Displacement techniques. MAE and RMSE are calculated.

At the end of testing, 1-1 error graphs, shown in Figure 4.5, are generated to visualize the differences in strains obtained through the MBDT, DIC, and Crosshead Displacement techniques. Compared to DIC, the MBDT technique demonstrates MAE and RMSE values of 0.6% and 0.7%, respectively. Compared to the strains calculated using the Crosshead Displacement technique, the MBDT technique exhibits MAE and RMSE values of 2.4% and 2.5%, respectively.

4.2.1.1.1 Effect of Surface Texture on Geomembrane Strains

The reason for using geomembrane test samples with different surface roughness was to observe how MBDT strains differ from other techniques in testing materials with varying textures. The samples were die-cut in the machine direction (MD) and cross-machine direction (CMD).

When comparing the test results shown in Figure 4.6 to Figure 4.9, it can be observed that for the used geomembrane types, the sample cut direction (MD or CMD) does not have a major effect on the strength and strain capacities at yielding. Furthermore, as depicted in Figure 4.6 and Figure 4.7, MBDT strains are not substantially distinct from the DIC or Crosshead Displacement strains when testing the smooth geomembrane samples (GMB Type-1).

Before discussing the notable difference between Crosshead Displacement strains and MBDT/DIC strains in Figure 4.8 and Figure 4.9, it is essential to highlight the reasons for the observed slope changes in these graphs. These slope changes occur because the image-based techniques used in this study could not detect small deformations during these particular tests. Consequently, linear interpolation between the available measurement points resulted in these graphs.

What becomes evident from the graphs presented in Figure 4.8 and Figure 4.9 is the compatibility between MBDT strains and DIC strains, whereas the Crosshead Displacement technique yields higher strain values than the other two techniques. Considering the observation that the sample does not slip between the pneumatic grips during the test, it can be inferred that the reason for this discrepancy lies in the non-uniform distribution of strains within the gauge length for yielding on the one-sided textured geomembrane, as shown in Figure 4.10b. In contrast, strains on the smooth geomembrane, as shown in Figure 4.10a, exhibit a more uniform distribution. Consequently, the average strains calculated within the yielding gauge length (L_0=33mm) are lower for the one-sided textured geomembrane, making MBDT and DIC strains lower than the Crosshead Displacement strains.

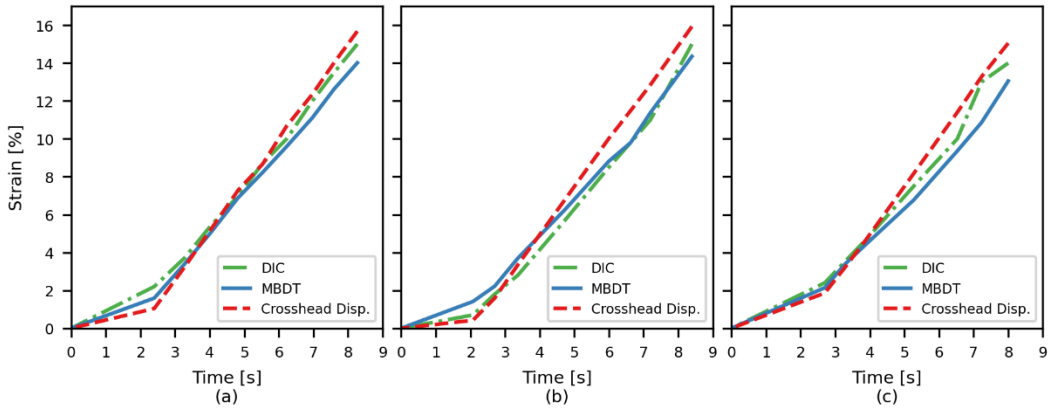

Figure 4.6. Strain – Time graphs for the tests (a) T-GMB_1, (b) T-GMB_2, (c) T-GMB_3. HDPE geomembrane samples are 1.5-mm-thick and smooth. The samples are cut in the machine direction. The test speed is set to 50 mm/min.

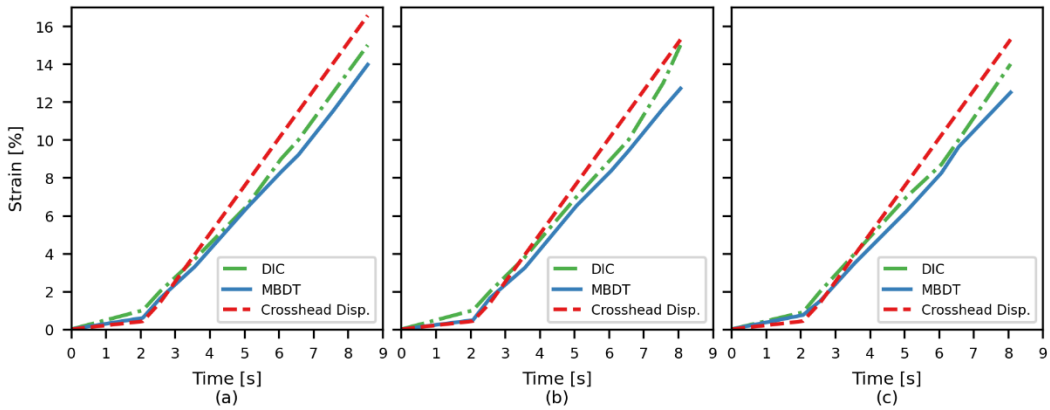

Figure 4.7. Strain – Time graphs for the tests (a) T-GMB_4, (b) T-GMB_5, (c) T-GMB_6. HDPE geomembrane samples are 1.5-mm-thick and smooth. The samples are cut in the cross-machine direction. The test speed is set to 50 mm/min.

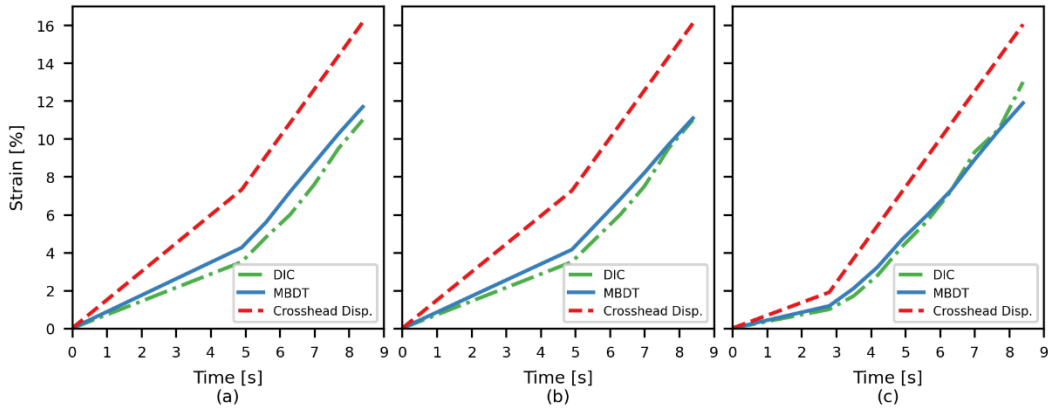

Figure 4.8. Strain – Time graphs for the tests (a) T-GMB_7, (b) T-GMB_8, (c) T-GMB_9. HDPE geomembrane samples are 1.5-mm-thick and one-sided textured. The samples are cut in the machine direction. The test speed is set to 50 mm/min.

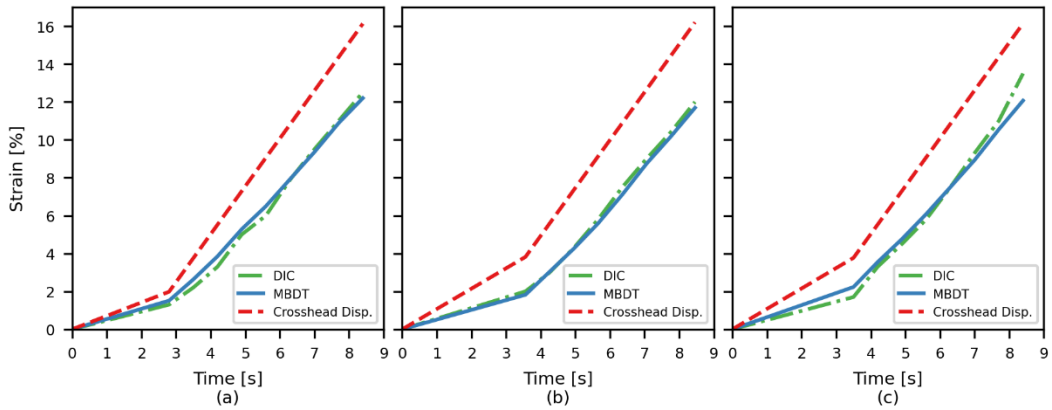

Figure 4.9. Strain – Time graphs for the tests (a) T-GMB_10, (b) T-GMB_11, (c) T-GMB_12. HDPE geomembrane samples are 1.5-mm-thick and one-sided textured. The samples are cut in the cross-machine direction. The test speed is set to 50 mm/min.

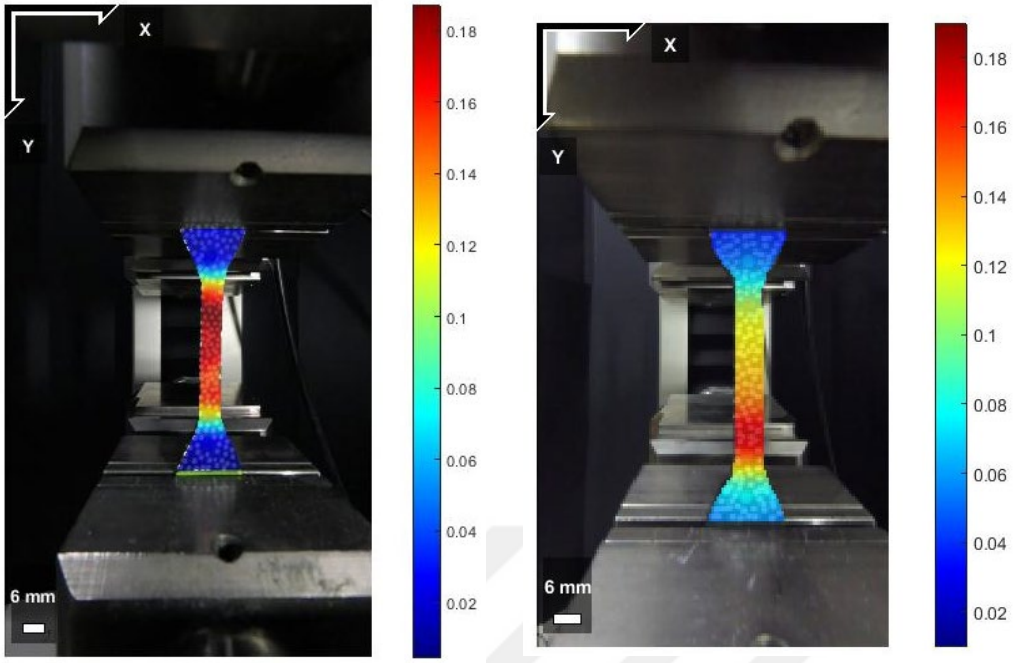

(a) (b)

Figure 4.10. Strain distribution comparison of (a) 1.5-mm smooth, (b) 1.5-mm one-sided textured geomembrane at yielding, produced by DIC.

4.2.1.2 Testing of Geotextiles

For evaluating the effectiveness of the MBDT technique on tensile testing of geotextiles, 12 samples were tested, consisting of three material types with different masses per unit area: (i) 300 g/m^2, (ii) 400 g/m^2, and (iii) 600 g/m^2. The non-woven geotextile samples were die-cut into square-shaped specimens measuring 200 by 200 mm. The relevant material properties are provided in Table 4.5.

The strains occurring in the geotextiles with the masses per unit area of 300 g/m^2 and 400 g/m^2 were continuously tracked until the samples ruptured. However, for the geotextiles with a mass per unit area of 600 g/m^2, strain tracking was limited due to sample slippage in the mechanical wedge grips, resulting in a significant loss in the measured tensile strength.

The validation tests were conducted in two separate test groups, aiming to assess the performance of the MBDT technique under different test speeds and variations in the geotextile mass per unit area. The details of these test groups and their respective parameters are summarized in Table 4.5.

Table 4.5. Geotextile mass per unit area and implemented test speeds.

Test ID	Mass Per Unit Area (g/m^2)	Test Speed (mm/min)
T-GTX_1 to T-GTX_3	400	10
GTX_4 to GTX_6	400	20
GTX_7 to T-GTX_9	600	20
T-GTX_10 to T-GTX_12	300	20

The geotextile tests followed the guidelines outlined in the ISO 10319 test standard. The nominal gauge length for the Crosshead Displacement technique, which can be employed under particular circumstances, is defined by this standard as the distance between the grips, which is 100 mm. On the other hand, for the MBDT technique, a

gauge length of 60 mm was selected as the test standard recommends when extensometers are utilized. Hence, there is a difference in gauge lengths between the MBDT and Crosshead Displacement techniques. In summary,

a) Strain at maximum load, $\varepsilon_t = \frac{\Delta L}{L_0}$, where L_0=60 mm (Extensometer). ΔL is the measured elongation in the gauge length.

b) Strain at maximum load, $\varepsilon_t = \frac{\Delta L_{CT}}{L_0}$, where L_0=100 mm (Crosshead Displacement). ΔL_{CT} is the crosshead travel distance.

The strain measurement techniques employed to validate the MBDT technique for testing of geotextiles are explained in detail below:

i. *MBDT:* Two color markers are placed at the start and end points of the initial gauge length (L_0=60 mm). These markers are continuously tracked throughout the test. The elongation of the gauge length is determined by finding the increase in the vertical distance between start and end markers. The elongation is divided by the initial gauge length for calculating the strain within the gauge length. This division measures the relative deformation or elongation of the material within the specified gauge length.

ii. *DIC:* The strains calculated for the whole region of interest, as shown in Figure 4.12b, are used to determine the average strains within the center of the specimen covering the gauge length (L_0 = 60 mm). Taking the average strains within the specimen's center helps eliminate any localized variations or irregularities outside the gauge length. This approach ensures that the strain measurements represent the deformation within the designated gauge length.

iii. *DIC Displacement-Derived:* Displacements calculated for the entire region of interest, as shown in Figure 4.12a, are used to determine the elongation of the gauge length. Similar to MBDT, the color marker are

tracked continuously, and the increase in the vertical distance between these markers represents the elongation. The elongation is then divided by the initial gauge length (L_0 = 60 mm) to calculate the strains. This methodology allows for measuring strains based on the displacement of the color markers within the designated gauge length. It provides a direct way to assess the success of MBDT, as both techniques are based on the tracking of color marker displacements.

iv. *Crosshead Displacement:* By defining a nominal gauge length (L_0 = 100 mm), it is assumed that the specimen elongation is equal to UTM crosshead travel distance. For calculating strains using the Crosshead Displacement technique, the elongation is divided by the nominal gauge length. As the Crosshead Displacement technique assumes uniform elongation within the gauge length and the technique does not account for localized deformations or non-uniform strain distribution. Therefore, it may not accurately capture the actual behavior of the specimen in certain situations.

Table 4.6. Key physical and mechanical properties of the geotextile samples. Technical specification limit values are indicated in square brackets.

	GTX-Type 1	GTX-Type 2	GTX-Type 3
Number of Samples	6	3	3
Mass Per Unit Area (g/m^2)	400	600	300
Tensile Strength (MD/CMD) (g/m^2)	25 / 28 [> 23.5 / > 23.5]	N/A* [> 30.0 / > 30.0]	15 / 14 [> 10.0 / > 8.0]
Static Puncture Strength, CBR (kN)	4.3 [> 4.2]	9.4 [> 6.0]	2.8 [> 1.8]

*Tensile strength could not be obtained as the sample slipped inside the wedge grips before rupturing.



(a) (b)

Figure 4.11. (a) Test sample with color markers designating the gauge length (L_0 = 60 mm) and speckles drawn for the DIC technique. (b) A mechanical wedge grip is testing the sample. The grips are covered with black cardboard to prevent any reflections of light.

Figure 4.11a illustrates the specimen marking scheme used for the tests. The green markers indicate the gauge length used for both MBDT and DIC Displacement-Derived techniques. The blue horizontal lines represent the boundaries of the nominal gauge length, which indicate the region where the specimen is clamped by the mechanical wedge grips as shown in Figure 4.11b. A speckle pattern is applied to the entire area of interest for the application of DIC technique.

Figure 4.12a displays the displacement field obtained using DIC, showing the computed displacements of speckles across the geotextile specimen. Figure 4.12b depicts the corresponding strain field. It can be observed that strain localization occurs on the geotextile, with strain values being uniform in the middle portion of the specimen and varying closer to the edges.

Figure 4.12c is a snapshot while MBDT technique is being used. The green markers are tracked as they displace. Unlike DIC, which requires the region of interest to be

defined before the test, MBDT is sensitive to the reflection of markers from polished wedge surfaces. Therefore, the surfaces are covered with matte black color, reducing unwanted reflections, and enhancing the accuracy of marker tracking.

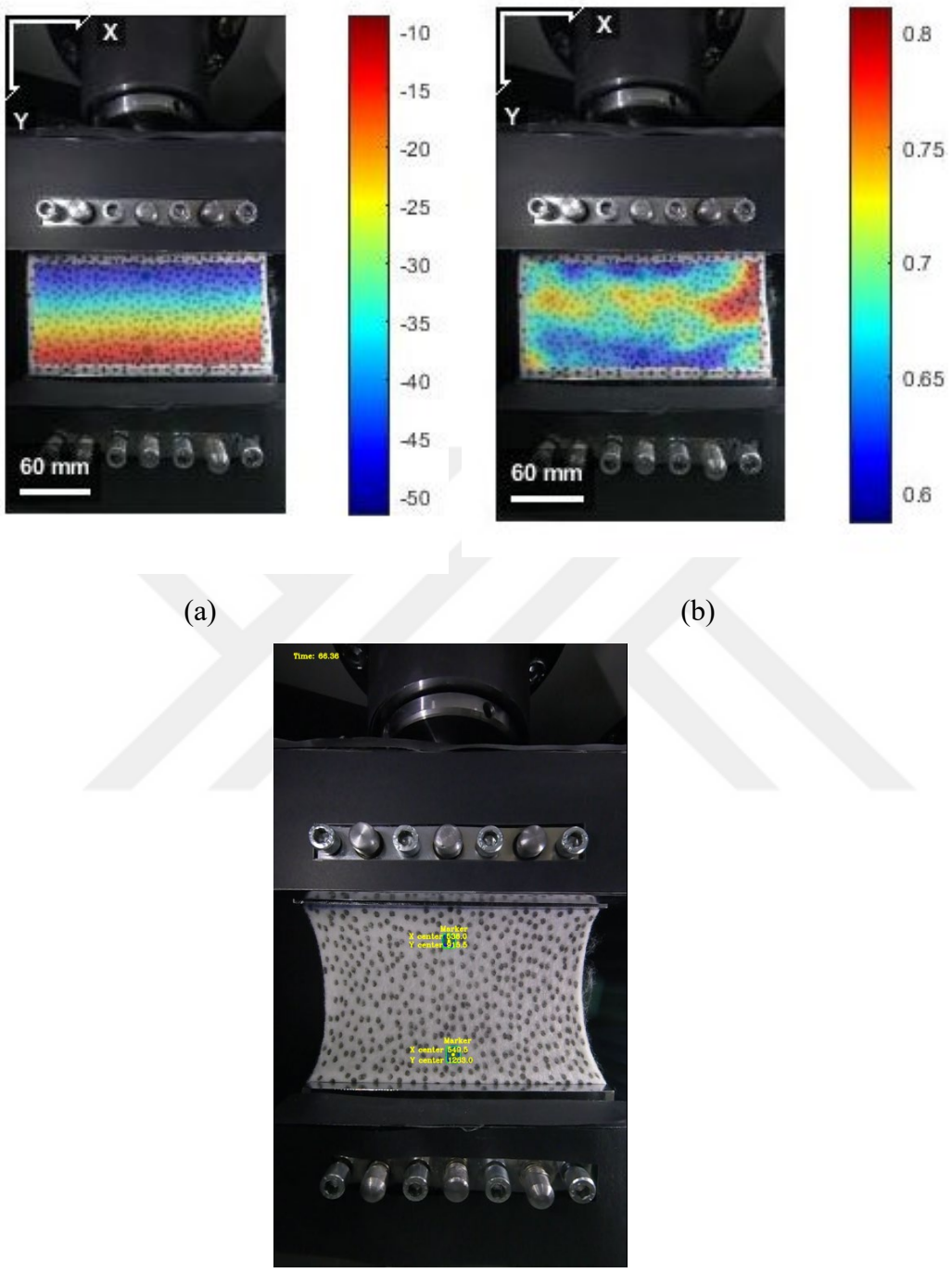

Figure 4.12. Different image-based methods are in use for the geotextile sample (T-GTX_1). (a) DIC, displacement distribution heat map (mm). (b) DIC, strain distribution heat map (Lagrangian-Green). (c) MBDT, identification of color markers.

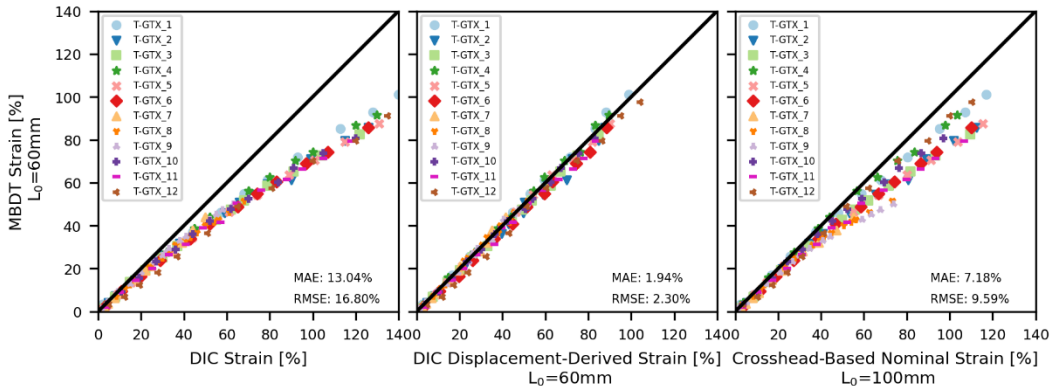

Figure 4.13. For each test, strains by MBDT are compared with DIC, DIC-Displacement Derived (L_0 = 60mm), and Crosshead Displacement techniques (L_0=100 mm). MAE and RMSE are calculated.

Figure 4.13 shows the 1-1 error graphs, highlighting the variations in strains calculated by MBDT, DIC, DIC Displacement-Derived, and Crosshead Displacement techniques. Compared to DIC, MBDT demonstrates MAE and RMSE values of 13.0% and 16.8%, respectively. However, when compared to DIC Displacement-Derived strains, MBDT exhibits significantly lower errors, with MAE and RMSE values of 1.9% and 2.3%, respectively. In comparison to strains determined by Crosshead Displacement, MBDT yields MAE and RMSE values of 7.2% and 9.6%, respectively.

These error values suggest that MBDT excels at accurately tracking displacements between two designated points, as indicated by the low errors when compared to DIC Displacement-Derived technique. However, the discrepancies between MBDT and DIC strains become more prominent after approximately 50% strain, potentially due to strain localizations that affect the average strain within the gauge length. Similarly, significant differences between MBDT and Crosshead Displacement strains emerge at around 70%. Possible factors contributing to this disparity include incomplete deformation of the specimen by crosshead movement and slippage of the sample in the mechanical wedge grips.

4.2.1.2.1 Effect of Test Speed on Geotextile Strains

This section investigates the effects of test speed on geotextile strains, along with a comparison of MBDT with different strain measurement techniques. The geotextile samples with a mass per unit area of 400 g/m^2 (GTX Type-1, Table 4.6) were divided into two groups, each consisting of three specimens. One group was tested at 10 mm/min, while the samples of the other group were tested at 20 mm/min.

Figure 4.14 and Figure 4.15 demonstrate that strains obtained by each technique reach to the similar ultimate values regardless of the test speed. When comparing the techniques, MBDT and DIC Displacement-Derived techniques yield almost identical strains over time, while DIC and Crosshead Displacement techniques produce higher strains. DIC provides the largest strains in all six tests, followed by the Crosshead Displacement technique.

Figure 4.16 and Figure 4.17 present Load-Strain plots for each test. Irrespective of the test speed, the tested geotextiles rupture at similar ultimate loads. Furthermore, these figures confirm the findings of the Poggiogalle et al. (2022) study on geotextiles, which suggested that image-based strain measurement techniques yield steeper Load-Strain slopes than the Crosshead Displacement technique. The results from the six tested geotextiles with a mass per unit area of 400 g/m^2 further support this conclusion.

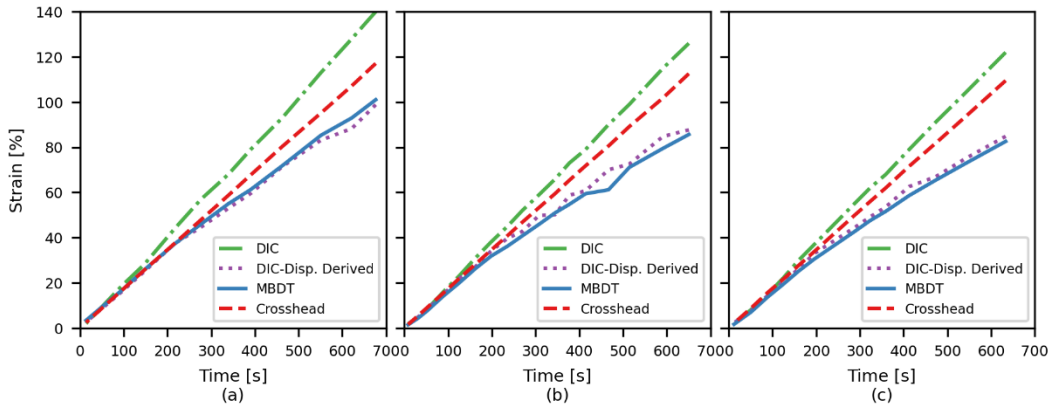

Figure 4.14. Strain – Time graphs for the tests (a) T-GTX_1, (b) T-GTX_2, (c) T-GTX_3. Geotextile samples have a mass per unit area of 400 g/m^2. The test speed is set to 10 mm/min.

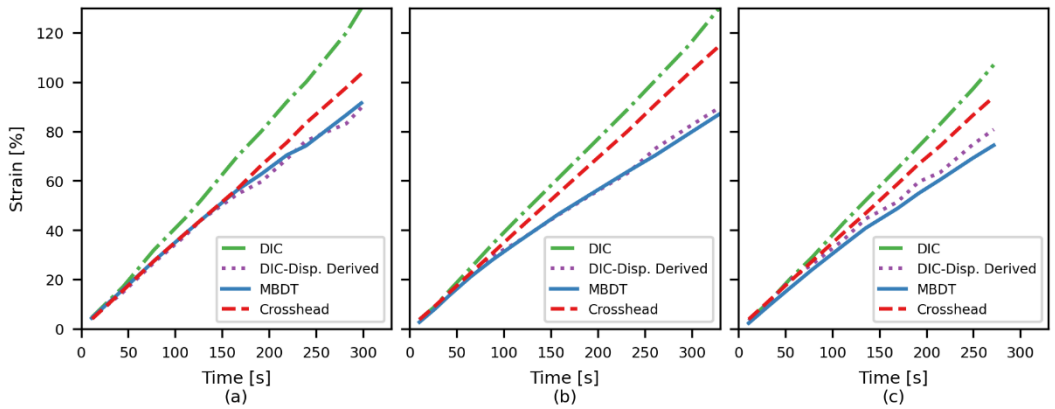

Figure 4.15. Strain – Time graphs for the tests (a) T-GTX_4, (b) T-GTX_5, (c) T-GTX_6. Geotextile samples have a mass per unit area of 400 g/m^2. The test speed is set to 20 mm/min.

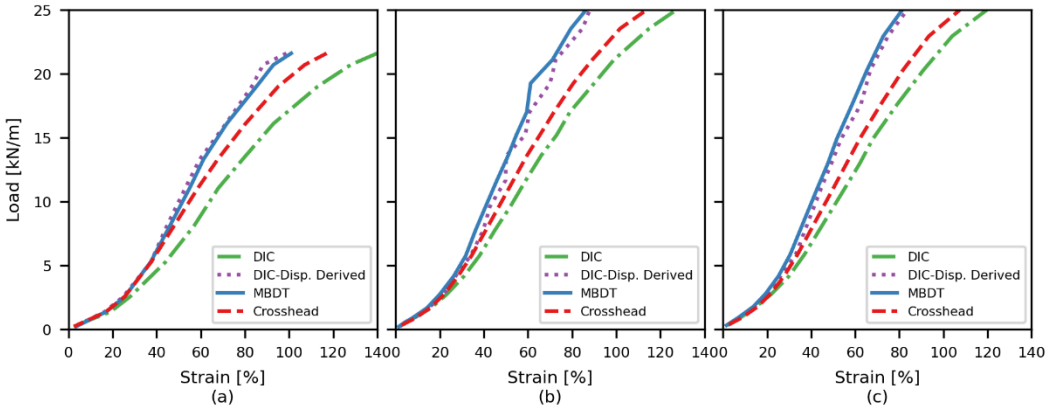

Figure 4.16. Load – Strain graphs for the tests (a) T-GTX_1, (b) T-GTX_2, (c) T-GTX_3. Geotextile samples have a mass per unit area of 400 g/m^2. The test speed is set to 10 mm/min.

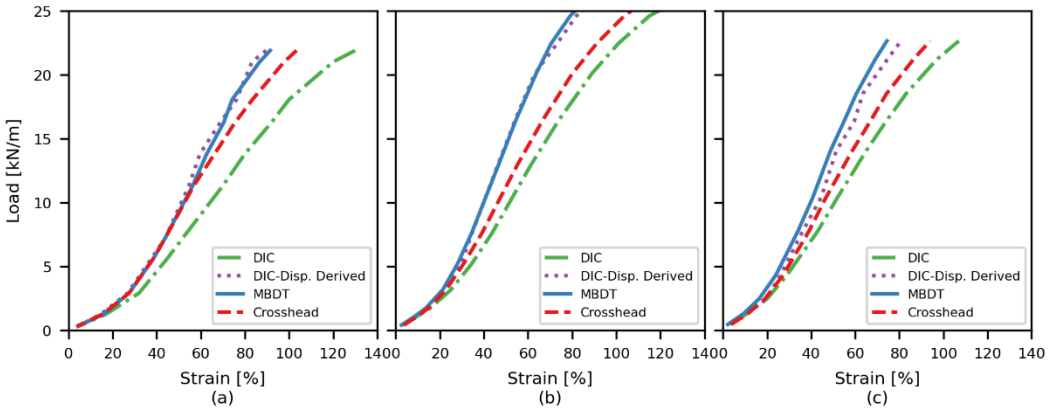

Figure 4.17. Load – Strain graphs for the tests (a) T-GTX_4, (b) T-GTX_5, (c) T-GTX_6. Geotextile samples have a mass per unit area of 400 g/m^2. The test speed is set to 20 mm/min.

4.2.1.2.2 Effect of Mass Per Unit Area on Geotextile Strains

This section focuses on assessing the applicability of MBDT on testing of non-woven geotextiles with different masses per unit area (300 g/m^2, 400 g/m^2, and 600 g/m^2) and investigating the potential effects of mass per unit area on geotextile strains. Three samples from each geotextile type (given in Table 4.6) were tested at a 20 mm/min test speed.

The geotextile with a mass of 400 g/m^2 (GTX Type-1) is taken as the reference material, as its Strain-Time and Load-Strain results were previously reported (Figure 4.15 and Figure 4.17) and are repeated in Figure 4.18 and Figure 4.21, respectively.

When testing a denser geotextile with a mass per unit area of 600 g/m^2 (GTX Type-2), significant slippage was observed within the mechanical wedge grips, as reported in the literature (Skochdopole et al., 2000), leading to the tests being stopped before reaching the ultimate tensile capacity, as shown in Figure 4.22. As inferred from Figure 4.22b, strain measurement techniques are split into two groups: (i) MBDT and DIC Displacement-Derived, and (ii) DIC and Crosshead Displacement. While MBDT and DIC Displacement-Derived strains still overlap to some extent, a significant distinction can be observed between DIC and Crosshead Displacement and the other two techniques, which may be attributed to the slippage issue. As expected, strains calculated by the Crosshead Displacement technique are the largest since the UTM continues to move, resulting in nominal strains without specimen deformation. Due to the unbalanced gripping force caused by slippage, strains start to localize to a specific region, causing DIC strains to become as high as the Crosshead strains. On the other hand, due to slippage, the specimen does not uniformly elongate within its gauge length, resulting in MBDT and DIC Displacement-Derived techniques producing lower strains for the same load, leading to a steeper load-strain slope.

For a less dense geotextile with a mass per unit area of 300 g/m^2 (GTX Type-3), no substantial difference was observed compared to GTX Type-1 (400 g/m^2), except for

a lower maximum load capacity, as shown in Figure 4.23. The ultimate strains (Figure 4.23) were similar to those observed with GTX Type-1. Once again, MBDT and DIC Displacement-Derived techniques yielded very close strains, while DIC calculated notably higher strains. The Crosshead Displacement technique followed DIC.

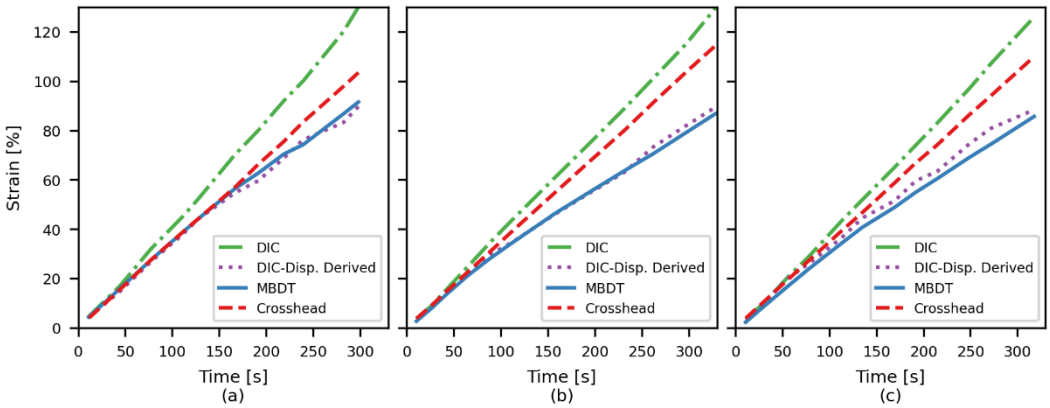

Figure 4.18. Strain – Time graphs for the tests (a) T-GTX_4, (b) T-GTX_5, (c) T-GTX_6. Geotextile samples have a mass per unit area of 400 g/m^2. The test speed is set to 20 mm/min.

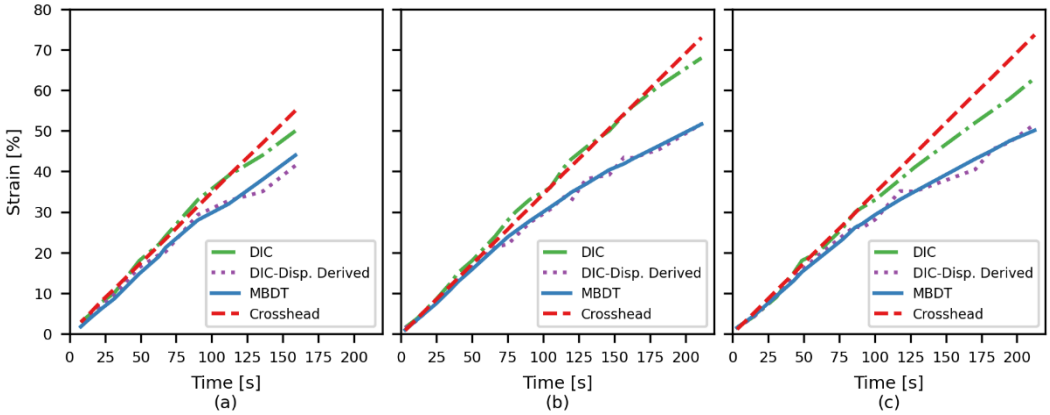

Figure 4.19. Strain – Time graphs for the tests (a) T-GTX_7, (b) T-GTX_8, (c) T-GTX_9. Geotextile samples have a mass per unit area of 600 g/m^2. The test speed is set to 20 mm/min.

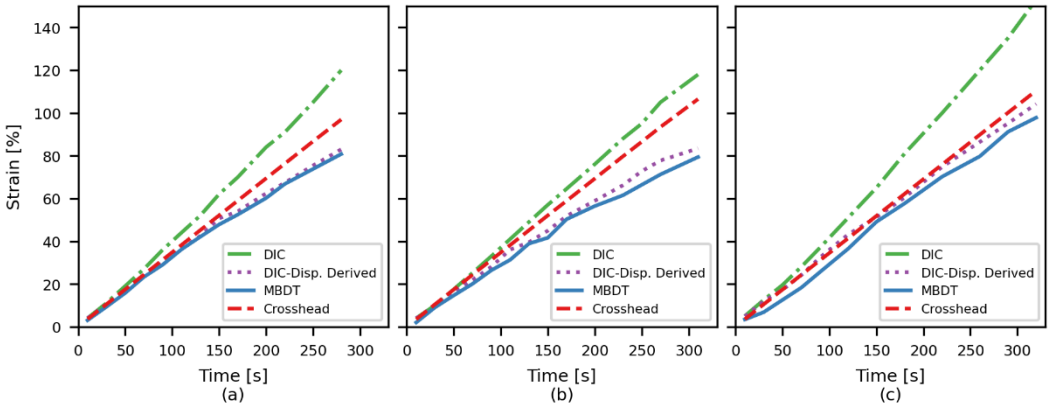

Figure 4.20. Strain – Time graphs for the tests (a) T-GTX_10, (b) T-GTX_11, (c) T-GTX_12. Geotextile samples have a mass per unit area of 300 g/m^2. The test speed is set to 20 mm/min.

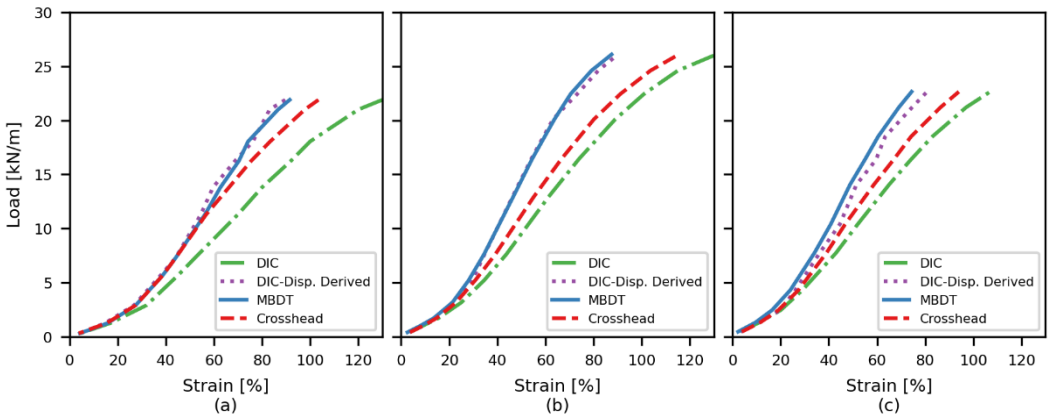

Figure 4.21. Load – Strain graphs for the tests (a) T-GTX_4, (b) T-GTX_5, (c) T-GTX_6. Geotextile samples have a mass per unit area of 400 g/m^2. The test speed is set to 20 mm/min.

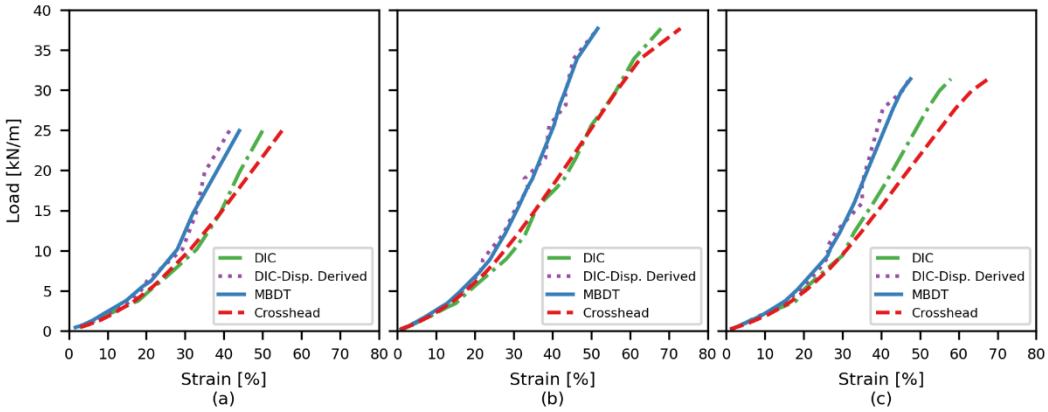

Figure 4.22. Load – Strain graphs for the tests (a) T-GTX_7, (b) T-GTX_8, (c) T-GTX_9. Geotextile samples have a mass per unit area of 600 g/m^2. The test speed is set to 20 mm/min.

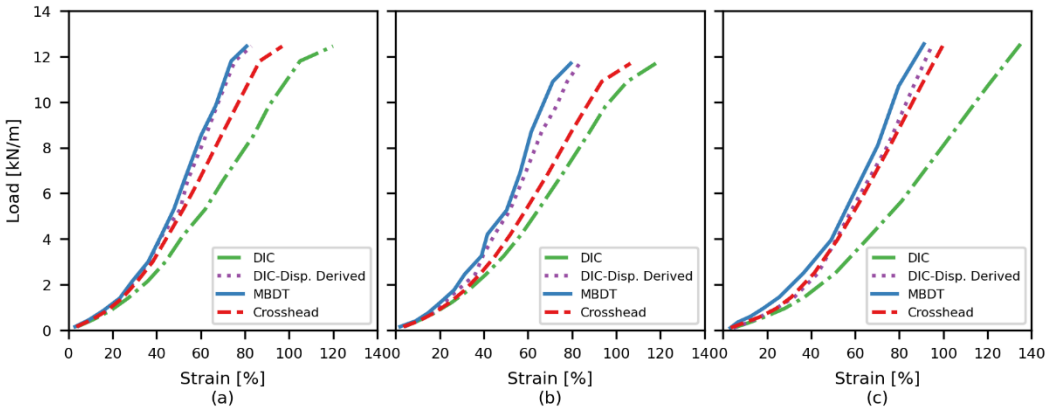

Figure 4.23. Load – Strain graphs for the tests (a) T-GTX_10, (b) T-GTX_11, (c) T-GTX_12. Geotextile samples have a mass per unit area of 300 g/m^2. The test speed is set to 20 mm/min.

4.2.1.3 Testing of Geosynthetic Clay Liners (GCL)

It was found after a review of the literature that whereas numerous studies use image-based strain measuring techniques for the tensile testing of geotextiles, only a small number of studies use these approaches for the testing of GCLs. Typically, a GCL consists of a woven geotextile at the bottom, a non-woven geotextile at the top, and a layer of bentonite in the middle. The purpose of incorporating these different materials is to achieve a high level of impermeability that would typically require compacting several meters of clay. However, with GCLs, this level of impermeability can be achieved in much thinner material, typically around 6 mm in thickness. This offers several advantages, including ease of installation, environmental friendliness, and sustainability.

While there may be limited studies applying image-based strain measurement techniques to test GCLs, applying these techniques in geotechnical engineering and geosynthetics research continues to expand. Image-based techniques allow for more accurate and detailed strain measurement, providing insights into the behavior and performance of geosynthetic materials like GCLs.

The physical and mechanical properties of the tested GCL samples are presented in Table 4.7. Before testing, 12 samples were prepared by die-cutting them into 200 by 200 mm square-shaped specimens. The testing of GCL samples followed the guidelines of ISO 10319, similar to the testing of geotextiles, but with a variation in the test speed. The 12 samples were divided into two groups, with six samples tested at a speed of 20 mm/min and the remaining six tested at 10 mm/min.

The same specimen preparation procedure used for geotextiles was followed for GCL samples, as illustrated in Figure 4.24a. The nominal gauge length boundaries, indicated by blue horizontal lines, determined the region where the specimen was clamped by the mechanical wedge grips shown in Figure 4.24b. During the testing, four different techniques were implemented to measure strains: (i) MBDT, (ii) DIC, (iii) DIC Displacement-Derived, and (iv) Crosshead Displacement. The objective

was to determine the strains taken by the GCL samples during tensile testing and investigate the applicability of MBDT for tensile testing of GCLs.

Table 4.7. Key physical and mechanical properties of the GCL samples. Technical specification limit values are indicated in square brackets.

Mass Per Unit Area (g/m^2)	4073 [> 4000]
Tensile Strength, MD-CMD (kN/m)	13 – 11 [> 11 – > 11]
Static Puncture Strength, CBR (kN)	2.5 [> 1.8]
Peel Strength (N/m)	464 [> 360]

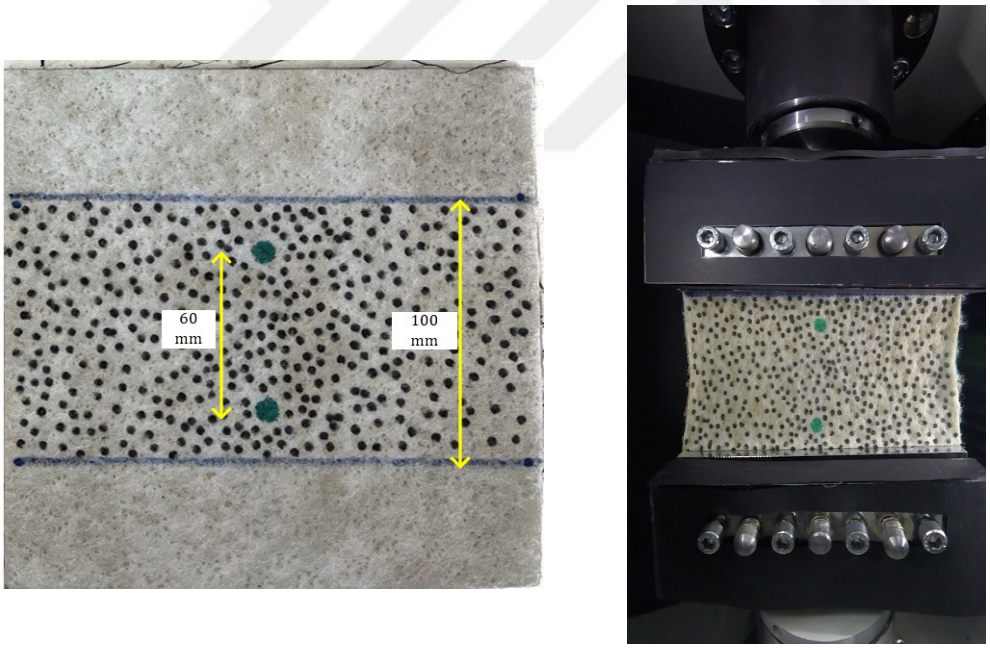

(a) (b)

Figure 4.24. (a) GCL test sample with color markers designating the gauge length (L_0 = 60 mm) and speckles drawn for the DIC technique. (b) A mechanical wedge grip is testing the sample. The grips are covered with black cardboard to prevent any undesired reflections of light.

Figure 4.24 illustrates the positioning of two green markers designating the gauge length used for MBDT and DIC Displacement-Derived techniques. In the case of the DIC technique, a speckle pattern is applied to the entire region of interest. The resulting displacement and strain fields, captured before the specimen ruptured, are presented in Figure 4.25a and Figure 4.25b, respectively. Figure 4.25b shows that the strains within the 60-mm gauge length in the center of the specimen are relatively uniform, while there is a significant increase in strains, reaching to 16%, at the bottom-left corner of the sample. On the specimen, there is a roughly 8% change in stresses from the left to the right side. Figure 4.25c displays a snapshot taken during MBDT technique is utilized, where the green markers are tracked to monitor the change in the gauge length.

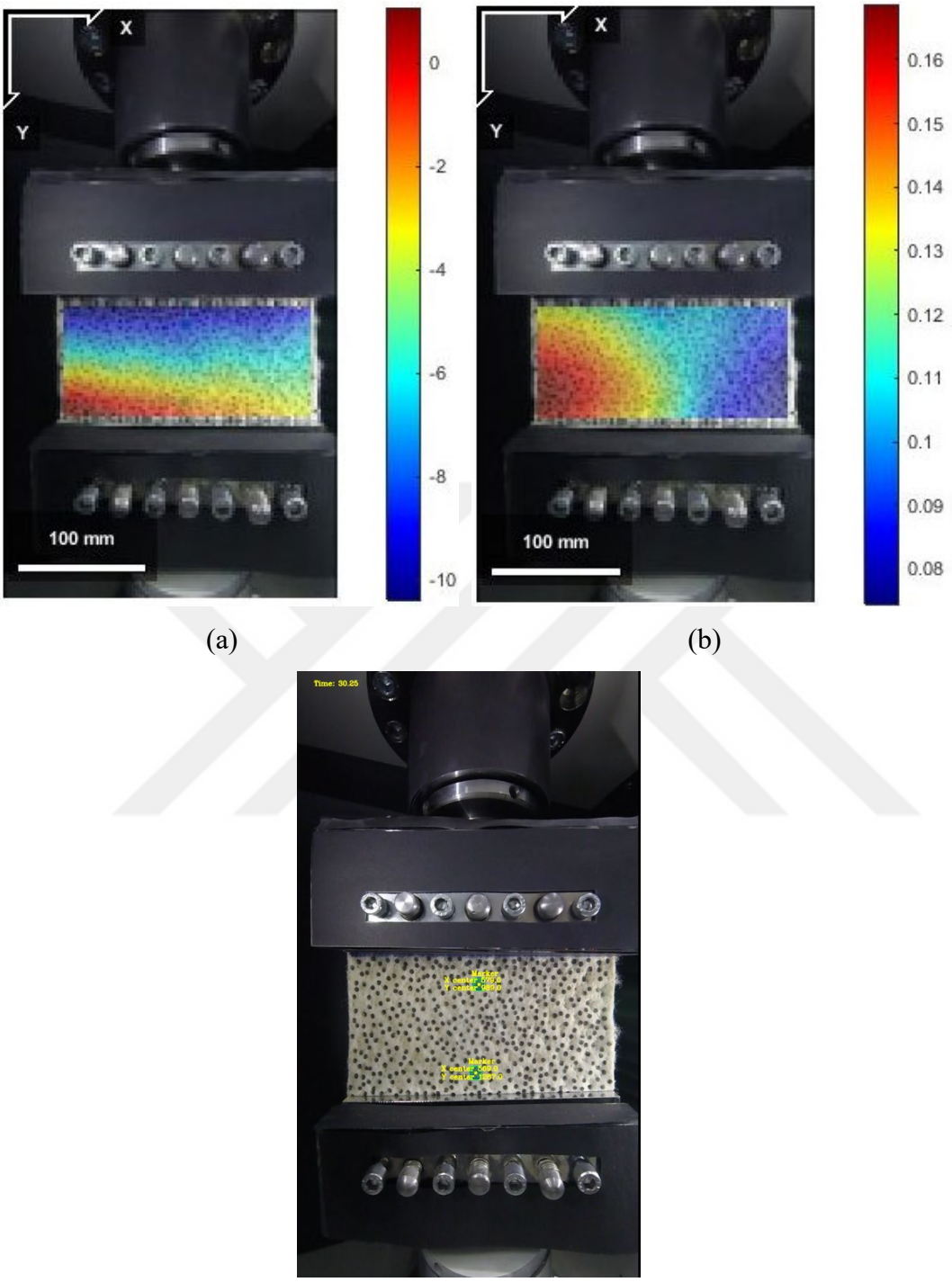

Figure 4.25. Different image-based methods are in use for the GCL sample (T-GCL_1). (a) DIC, displacement distribution heat map (mm). (b) DIC, strain distribution heat map (Lagrangian strains). (c) MBDT, identification of color markers.

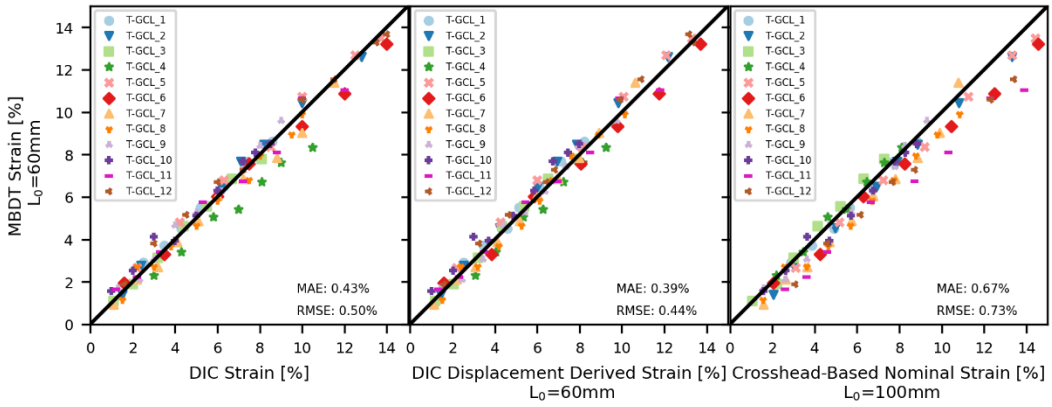

Figure 4.26. For each test, strains by MBDT are compared with DIC, DIC-Displacement Derived (L_0 = 60mm), and Crosshead Displacement techniques (L_0=100 mm). MAE and RMSE are calculated.

Figure 4.26 displays the 1-1 error graphs, illustrating the variation in strains calculated by MBDT, DIC, DIC Displacement-Derived, and Crosshead Displacement techniques. Overall, the errors between MBDT and the other techniques, namely DIC, DIC Displacement-Derived, and Crosshead Displacement, are below 1%. The MAE and RMSE results between MBDT and DIC strains are 0.4% and 0.5%, respectively. For the DIC Displacement-Derived technique, the MAE and RMSE values are both 0.4%. Finally, when comparing MBDT with the Crosshead Displacement technique, the MAE and RMSE values are 0.7%.

4.2.1.3.1 Effect of Test Speed on GCL Strains

This section aims to investigate the feasibility of using the MBDT technique on GCL specimens and observe the effects of test speed on GCL strain results. Two groups of samples, taken from the machine and cross-machine directions, were tested at 20 mm/min and 10 mm/min test speeds.

From Figure 4.27 to Figure 4.34, it can be observed that the samples taken in the machine direction exhibit higher tensile strength and strain capacity compared to those taken in the cross-machine direction. Moreover, regardless of the test speed, the specimens exhibited similar maximum load strain capacities when they were cut in the same direction (Figure 4.31 and Figure 4.33; Figure 4.32 and Figure 4.34).

In terms of strain measurement techniques, it was observed that the strain results were not substantially distinct from each other. The Crosshead Displacement technique consistently calculated higher strains compared to the other techniques, which becomes more apparent in Figure 4.30, Figure 4.33, and Figure 4.34. However, no considerable difference was observed between the MBDT, DIC, and DIC Displacement-Derived image-based techniques.

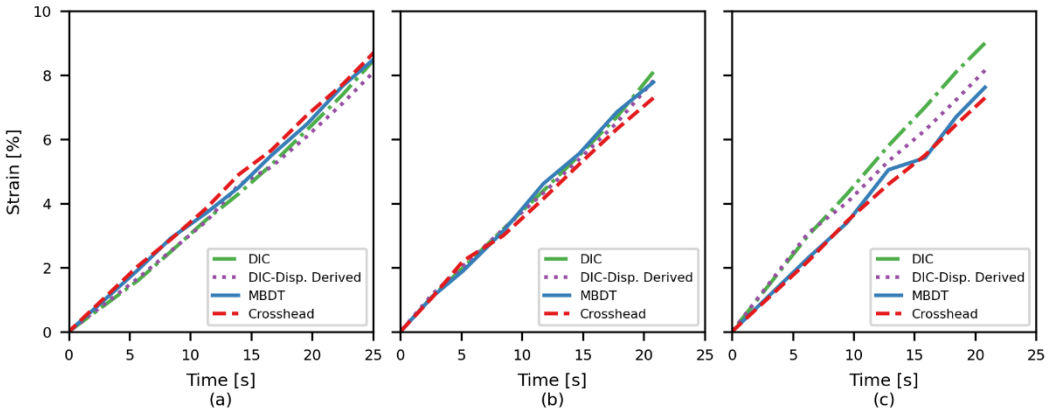

Figure 4.27. Strain – Time graphs for the tests (a) T-GCL_1, (b) T-GCL_3, (c) T-GCL_4. The samples are cut in cross-machine direction. The test speed is set to 20 mm/min.

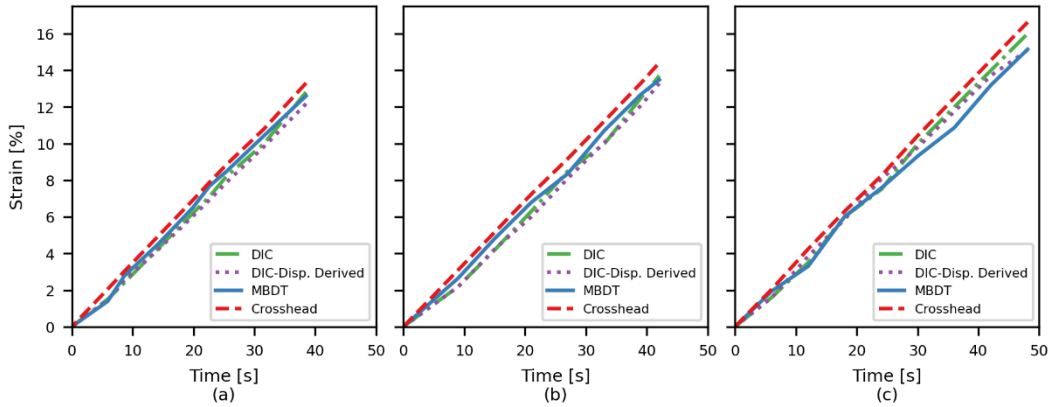

Figure 4.28. Strain – Time graphs for the tests (a) T-GCL_2, (b) T-GCL_5, (c) T-GCL_6. The samples are cut in the machine direction. The test speed is set to 20 mm/min.

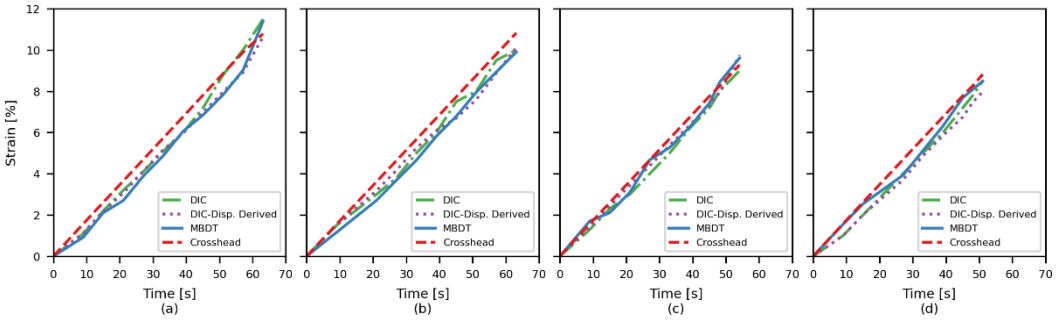

Figure 4.29. Strain – Time graphs for the tests (a) T-GCL_7, (b) T-GCL_8, (c) T-GCL_9, (d) T-GCL_10. The samples are cut in the cross-machine direction. The test speed is set to 10 mm/min.

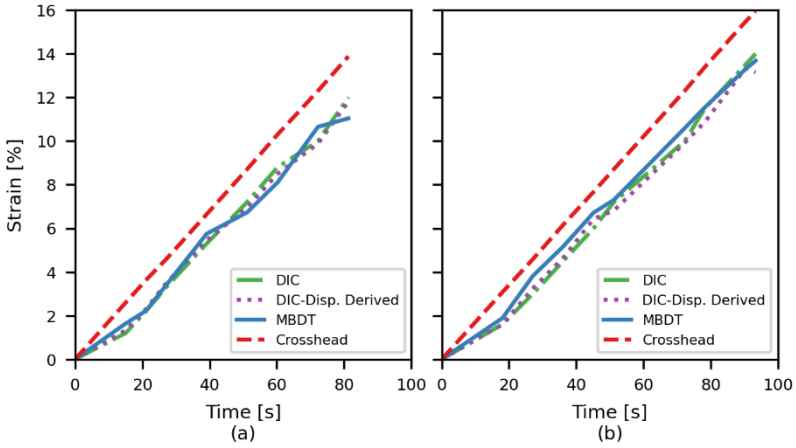

Figure 4.30. Strain – Time graphs for the tests (a) T-GCL_11, (b) T-GCL_12. The samples are cut in the machine direction. The test speed is set to 10 mm/min.

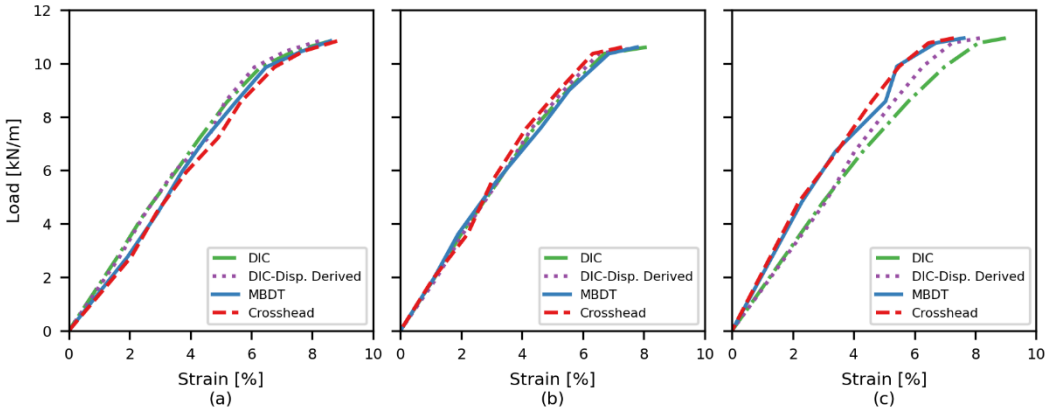

Figure 4.31. Load – Strain graphs for the tests (a) T-GCL_1, (b) T-GCL_3, (c) T-GCL_4. The samples are cut in the cross-machine direction. The test speed is set to 20 mm/min.

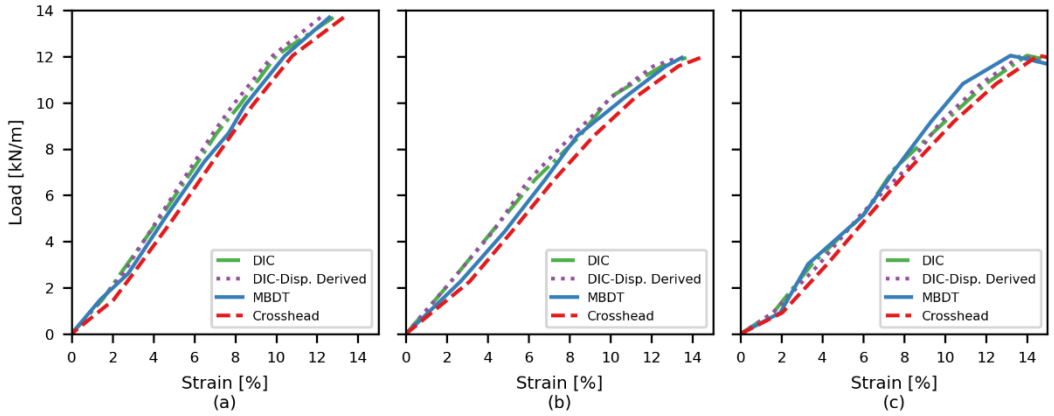

Figure 4.32. Load – Strain graphs for the tests (a) T-GCL_2, (b) T-GCL_5, (c) T-GCL_6. The samples are cut in the machine direction. The test speed is set to 20 mm/min.

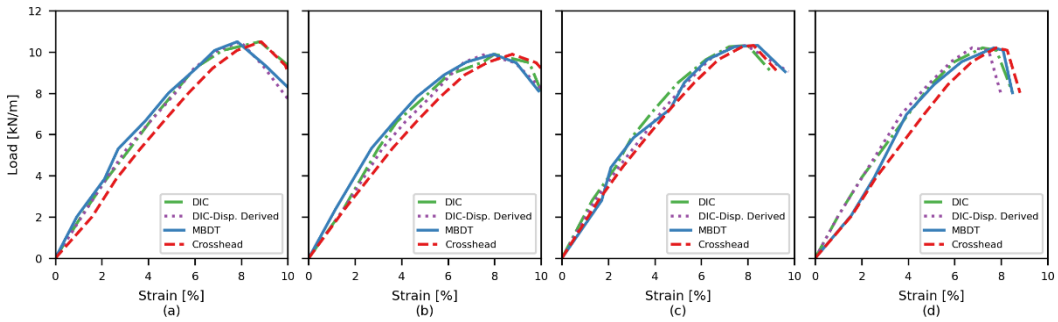

Figure 4.33. Load – Strain graphs for the tests (a) T-GCL_7, (b) T-GCL_8, (c) T-GCL_9, (d) T-GCL_10. The samples are cut in the cross-machine direction. The test speed is set to 10 mm/min.

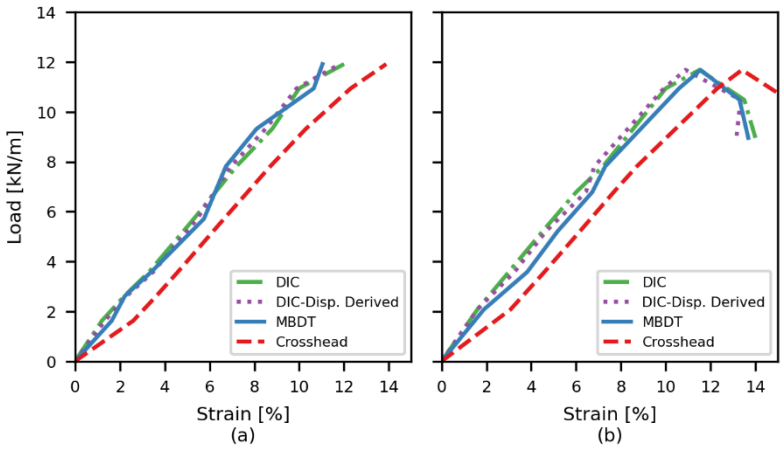

Figure 4.34. Load – Strain graphs for the tests (a) T-GCL_11, (b) T-GCL_12. The samples are cut in the machine direction. The test speed is set to 10 mm/min.

4.2.2 Validation of Camera Calibration

In this section, the MATLAB Camera Calibrator App, an add-in software provided in the Computer Vision Toolbox (The MathWorks Inc., 2023), was utilized to validate the camera calibration routine employed in the study. The calibration images were captured following the recommendations provided by MATLAB, which include:

- Having more than ten calibration images,
- Discarding highly blurred images,
- Ensuring sufficient coverage of the calibration board on the image frame,
- Including images with variations in the calibration board,
- Avoiding images where the calibration board has an angle of more than 45° with the camera's optical axis.
- Avoiding images with high reprojection errors, considering a mean error smaller than or equal to one pixel.

The MATLAB Camera Calibrator App also guides whether to use or discard images before starting the calibration, which was found to be a useful feature. In the following sections, the calibration routine employed in the study is demonstrated and validated through a brief comparison with the MATLAB Camera Calibrator App.

It is important to note that this study's calibration routine follows the code provided in OpenCV tutorials based on Zhang (2000). Some modifications were made to meet the specific requirements of this study, and functions and modules available in the Camera Calibration and 3D Reconstruction documentation were implemented (Bradski, 2000).

4.2.2.1 Normal Lens Calibration

A *normal lens* is designed to produce images without significant distortion. Most Digital Lens Single Reflex (DSLR) and smartphone cameras have normal lenses. These cameras often have the AutoFocus feature, which adjusts the lens configuration to capture the best possible field of view and sharpness. However, this feature can pose practical challenges regarding camera calibration.

Each time the camera lens configuration changes due to AutoFocus, the camera's intrinsic matrix and lens distortion coefficients may also change. This means that camera calibration needs to be performed separately each time the lens configuration is altered. It is recommended to disengage AutoFocus before taking calibration images and keep it off throughout the test session to avoid this problem. In practice, it is found that disabling the AutoFocus after finding the best lens configuration by focusing on the test specimen makes the calibration process easier and more consistent. This ensures that the camera settings remain fixed during the calibration procedure. Two example calibration images demonstrating the typical images used for camera calibration are provided in Figure 4.35.

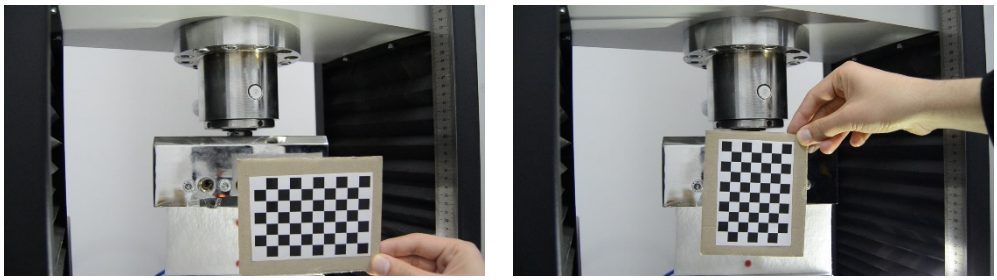

Figure 4.35. Calibration images taken by Nikon D5100 equipped with an 18-35mm normal lens (Cam-2).

During the validation test, 13 calibration images were input for OpenCV and MATLAB. These images were used to estimate the camera extrinsic matrix, representing the camera's position and orientation in the real scene. MATLAB provides a schematic view of the scene based on the estimated camera extrinsic matrix. This allows users to visualize and assess whether the estimated matrix accurately reflects the real scene.

Additionally, a graph of the reprojection errors was plotted, as shown in Figure 4.36. Reprojection error measures the discrepancy between the observed image points and the corresponding points reprojected from the estimated camera calibration. A smaller reprojection error indicates a better calibration result. In this case, the overall mean reprojection error was reported as 0.57 pixels, which is smaller than the threshold of 1 pixel. This suggests that the camera calibration achieved a satisfactory level of accuracy.

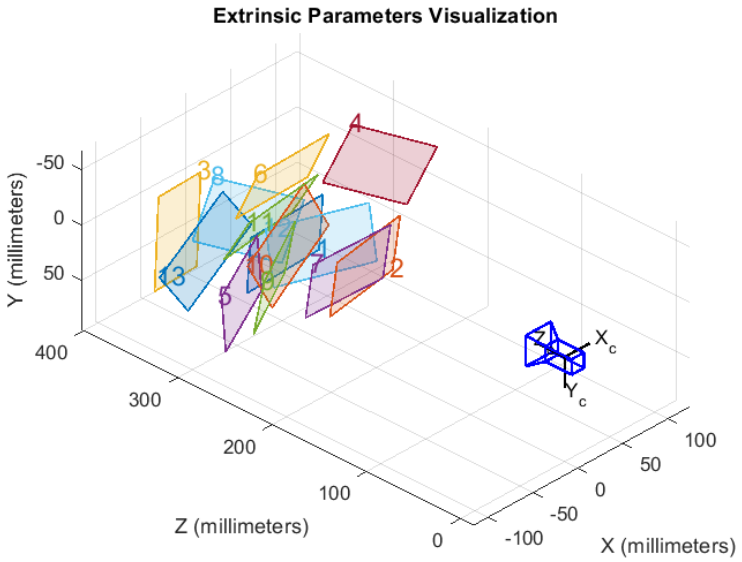

(a)

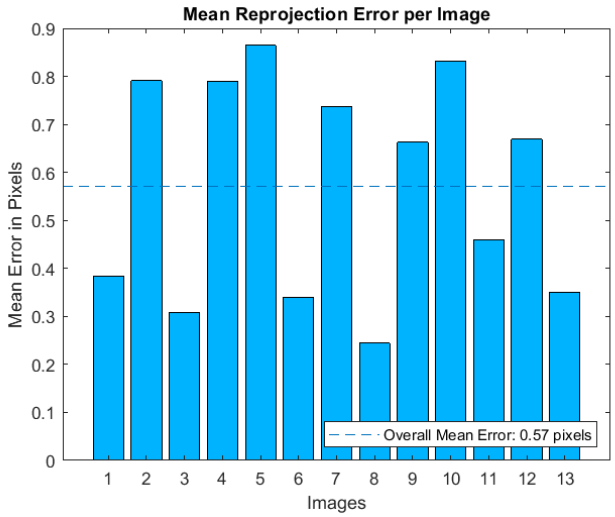

(b)

Figure 4.36. Camera calibration results for Cam-2, generated by MATLAB Camera Calibrator App. (a) Schematic plot showing the calibration board locations for each calibration image in real-world units. (b) Mean reprojection error graph.

Below is the mathematical summary of the results produced by OpenCV and MATLAB.

Image Dimensions (px): 1920 (h) x 1080 (v)

- OpenCV

  Camera Intrinsic Matrix (px) : $\begin{bmatrix} 1554.3586 & 0. & 1001.1686 \\ 0. & 1547.71383 & 557.2021 \\ 0. & 0. & 1. \end{bmatrix}$

  Lens Distortion Coefficients*: $\begin{bmatrix} -0.1169 & 0.0449 & 0. & 0. & 0. \end{bmatrix}$

  *Among the radial distortion coefficients of k_1, k_2 and k_3, only k_1 and k_2 were calculated. Tangential distortions (p_1 and p_2) with k_3 were assumed to be zero.

- MATLAB Camera Calibrator App

  Focal Length (px): $\begin{bmatrix} 1537.8080 \pm 10.0080 & 1531.8200 \pm 9.8980 \end{bmatrix}$

  Principle Point (px): $\begin{bmatrix} 1010.0735 \pm 3.2684 & 552.5686 \pm 3.8029 \end{bmatrix}$

  Radial Distortion: $\begin{bmatrix} -0.1139 \pm 0.0078 & 0.0322 \pm 0.0254 \end{bmatrix}$

Based on the above results, the following conclusions can be drawn:

- The intrinsic camera parameters show a maximum absolute error of 1% compared to the results obtained from MATLAB, indicating compatibility between the two methods.
- The radial distortion parameters also demonstrate compatibility between OpenCV and MATLAB.
- Based on these findings, it can be concluded that the calibration routine employed in this study is valid for normal lenses.

4.2.2.2 Fisheye Lens Calibration

An ultra-wide-angle lens, commonly known as a fisheye lens, is designed to capture a comprehensive view by inducing significant barrel distortion. These lenses are frequently used in action cameras for outdoor activities due to their panoramic view capability and enhanced optical features. Unlike normal lenses, fisheye lenses do not require lens adjustments or aperture configurations and usually does not have the AutoFocus feature. Additionally, action cameras are compact and versatile, allowing them to be easily mounted in various locations. While these characteristics make action cameras well-suited for outdoor and nature use, they are also considered suitable for laboratory applications due to their advantages.

Fisheye lenses are useful for calibration since the lens distortion coefficients are constant because the lens structure is fixed. Although the intrinsic camera matrix is valid only for specific image dimensions, it can be easily resized for other image sizes without needing a separate calibration session. Figure 4.37 shows a set of example calibration images for a fisheye lens camera.

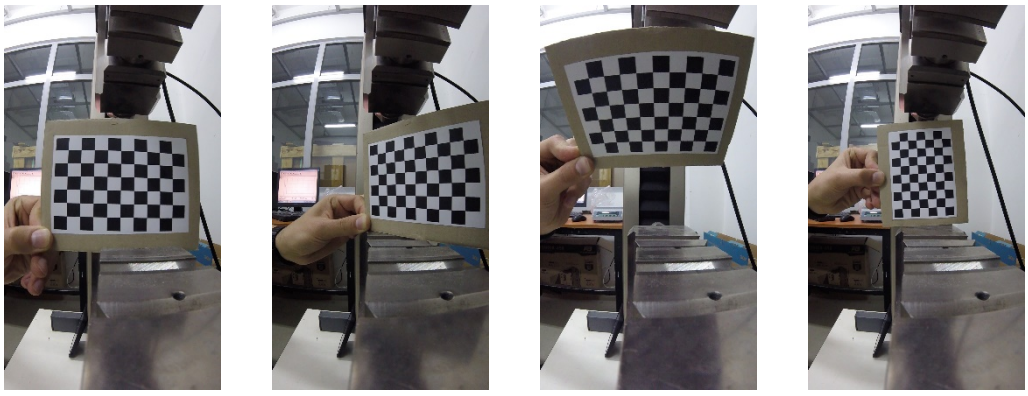

Figure 4.37. Calibration images taken by GoPro Hero 4 Session (Cam-1).

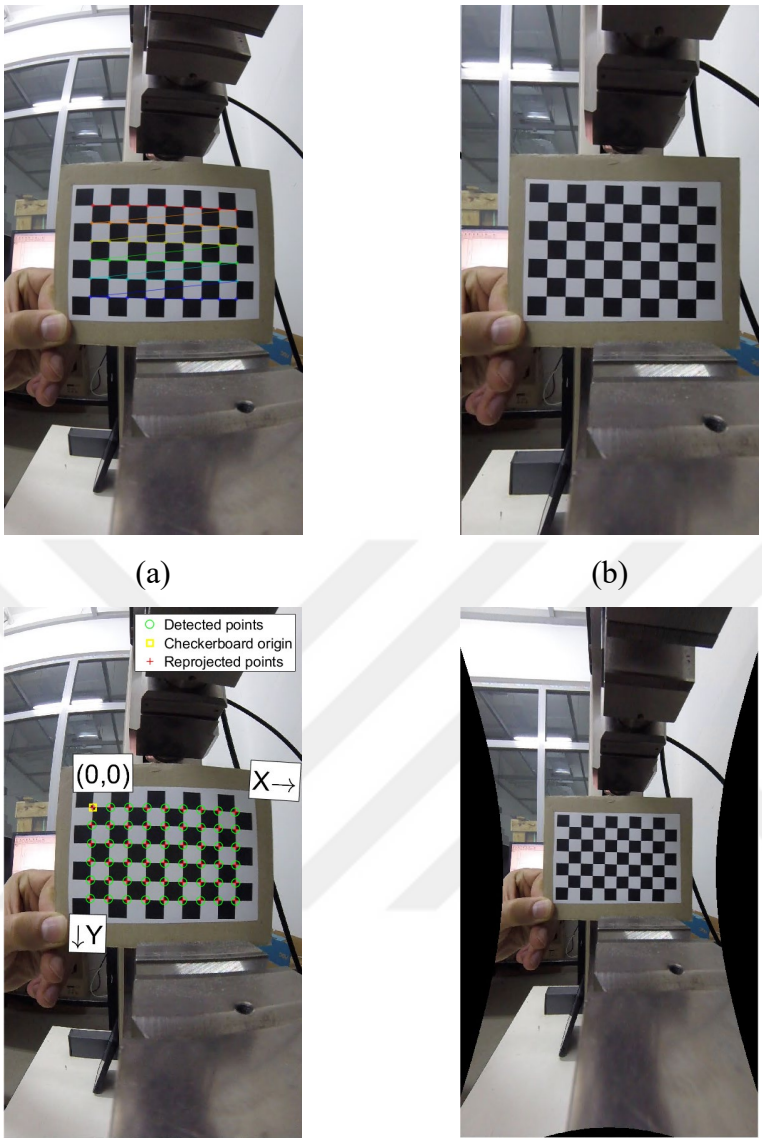

(a) (b)

(c) (d)

Figure 4.38. Images showing before and after calibration. (a) Automatic detection of the checkerboard pattern by OpenCV. (b) Corrected image produced by OpenCV. (c) Automatic detection of the checkerboard pattern by MATLAB. (d) Corrected image by MATLAB. While the OpenCV image is cropped, MATLAB image is left uncropped.

In Figure 4.38, both OpenCV and MATLAB display the original (distorted) calibration images alongside their respective corrected versions for the validation test. The calibration boards in Figure 4.39 demonstrate that the translational and

rotational configurations align well with the actual scenery. The overall mean reprojection error, calculated using the obtained camera matrix and lens distortion parameters, was below 1 pixel.

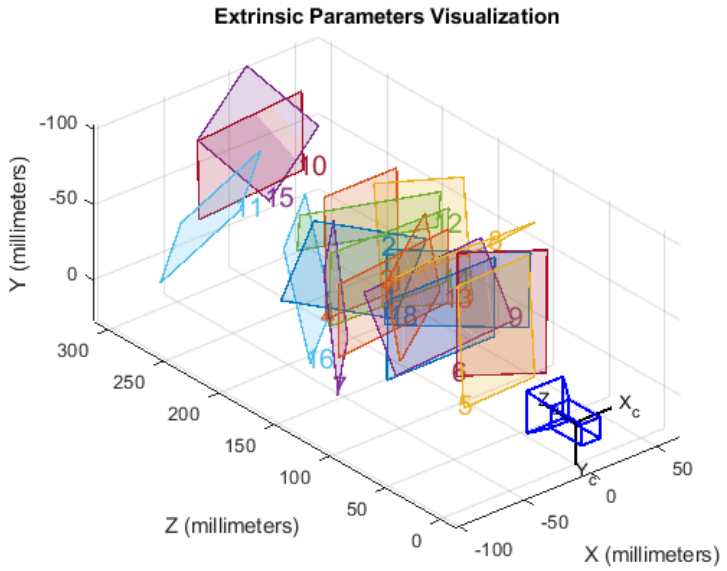

(a)

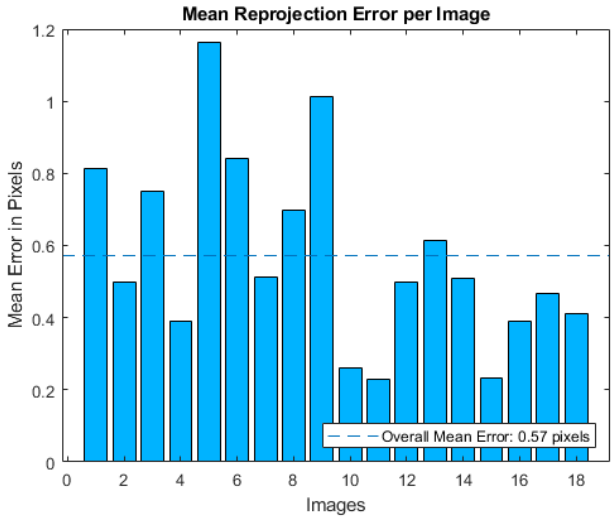

(b)

Figure 4.39. Camera calibration results of Cam-1 by MATLAB Camera Calibrator App. (a) Schematic plot showing the calibration board locations for each calibration image in real-world units. (b) Mean reprojection error graph.

The camera matrix and lens distortion coefficients reported at the end of calibration are summarized below:

Image Dimensions (px): 1080 (h) x 1920 (v)

- OpenCV

  Camera Intrinsic Matrix (px) : $\begin{bmatrix} 834.4727 & 0. & 538.1900 \\ 0. & 834.7905 & 967.8595 \\ 0. & 0. & 1. \end{bmatrix}$

  Lens Distortion Coefficients: $\begin{bmatrix} 0.0884581 \\ 0.13196017 \\ -0.36417396 \\ 0.26488411 \end{bmatrix}$

- MATLAB Camera Calibrator App

  Mapping Coefficients (px): $\begin{bmatrix} 836.1236 \pm 1.2715 \\ -0.0003 \pm 0.0000 \\ 0.0000 \pm 0.0000 \\ 0.0000 \pm 0.0000 \end{bmatrix}$

  Distortion Center (px): $\begin{bmatrix} 538.9259 \pm 1.3438 \\ 970.1419 \pm 1.3840 \end{bmatrix}$

  Stretch Matrix Parameters: $\begin{bmatrix} 1.0000 \pm 0.0000 \\ 0.0000 \pm 0.0000 \\ 0.0000 \pm 0.0000 \end{bmatrix}$

Based on the above findings, the following conclusions can be drawn:

- The camera's intrinsic parameters are accurate within a margin of 1 pixel.
- The calibration routine employed in this study can produce accurate results for images captured by a camera equipped with a fisheye lens.

4.2.2.3 Concluding Remarks on Calibration

- It is important to note that the intrinsic camera matrix obtained during calibration is specific to a particular image size, measured in pixels. However, this matrix can be adjusted to match different image sizes by scaling it accordingly. On the other hand, lens distortion coefficients remain unchanged regardless of the image size unless there are changes in the camera's lens configuration, such as zooming or focusing.
- OpenCV and MATLAB offer adjustable parameter values when calibrating a camera with a normal lens. For example, radial distortions can be represented by two or three coefficients, and tangential distortion can be assumed to be non-existent. These variations can have a significant impact on the success of the calibration process. In this study, different configurations were tested, and the ones resulting in the lowest reprojection errors were used.
- The calibration board should be printed with accurate scaling, ensuring that the grid is square and the edge length of one square is precisely measured. These dimensions are crucial inputs for the camera calibration routine.
- In cases where the same camera is used for recording videos and capturing images with different image sizes, it may be preferable to record a video and extract calibration images from it.
- Once the images have been corrected for lens distortions, image-based methods can be employed to obtain strains.

CHAPTER 5

SUMMARY, RESULTS, CONCLUSIONS, AND FUTURE WORK

5.1 Summary

Geosynthetic materials are commonly utilized in infrastructure projects, including railways, highways, pipelines, and mines, for various purposes such as reinforcement, stiffening, drainage, and separation. Different geosynthetic materials, including geotextiles, geomembranes, geosynthetic clay liners, and drainage geocomposites, can be employed individually or in combination. In their practical application, these materials must possess sufficient tensile strength and strain capacity to withstand different load requirements, highlighting the importance of accurately determining tensile strain capacities. This study introduces a computer vision-based technique designed to accurately and easily measure strains in geosynthetic materials during tensile testing.

Before being used in practical applications, the tensile strain capacity of geosynthetic materials is typically determined through index tests conducted in the laboratory. Although these tests do not precisely replicate field conditions or actual load demands, they provide valuable insights into material characteristics. Established testing standards recommend specific techniques for measuring strains during tensile testing, with two commonly used methods being (i) employing a contact-type extensometer device and (ii) utilizing the crosshead displacement of a Universal Testing Machine (UTM).

Using a contact extensometer involves calibrating the device and ensuring its smooth operation, which can be challenging due to its complex electromechanical systems. Additionally, these devices may not be compatible with different types of UTMs.

Determining the optimal clamping force for the extensometer, especially for materials with varying textures like geomembranes, can be tedious. Moreover, attaching the extensometer to a specimen, such as a geotextile, by creating holes can potentially alter the tensile characteristics of the material and lead to inaccurate results.

Utilizing the crosshead displacement of a UTM is a more straightforward approach. However, Crosshead Displacement technique may lack accuracy due to assumptions that the specimen elongates by the same amount as the crosshead travel distance. This assumption may not hold if the sample slips within the grips or if the inertia of UTM components causes machine compliance.

On the other hand, non-contact extensometers offer advantages over contact extensometers and the Crosshead Displacement technique. These devices utilize computer vision and optical principles to detect deformation on the specimen without clamping, attaching, or causing side effects on the test specimens. Non-contact techniques provide non-destructive and robust strain measurement capabilities, eliminating the complexities of calibration and the inaccuracies associated with slippage or inertial effects.

While commercial non-contact extensometers are available, they are often expensive and may not be adaptable to changing research needs. Therefore, this study aimed to develop an affordable, accurate, easy-to-use, non-contact strain measurement technique specifically for geosynthetic tensile testing. The study employed the OpenCV computer vision library (Bradski, 2000) and utilized the Python programming language for code development.

The Marker-Based Displacement Tracking (MBDT) technique was developed, which involves identifying color markers drawn on the specimen through image segmentation using color thresholding and edge detection algorithms. Additionally, the study incorporated the Digital Image Correlation (DIC) technique using the Ncorr software (Blaber et al., 2015). These techniques provide alternative and

reliable methods for measuring strains in geosynthetic materials during tensile testing.

Laboratory tests were conducted on different material types, including HDPE geomembrane, non-woven geotextile, and geosynthetic clay liner (GCL), to evaluate the accuracy and applicability of the MBDT technique for various geosynthetic types. Strains obtained using the DIC and Crosshead Displacement techniques were compared with those calculated using the MBDT technique. It was proven that this non-contact method could obtain accurate strain measurements for various geosynthetic material types by providing insights into the MBDT technique's performance and usability for geosynthetic testing.

5.2 Results Overview

Below are the conclusions for tests implementing MBDT, drawn for different geosynthetic types.

5.2.1 Geomembrane Tests

- 12 tests were carried out on two types of HDPE geomembrane samples to determine the suitability of MBDT for testing geomembranes: (i) 1.5-mm smooth and (ii) 1.5-mm one-sided textured, following ASTM D6693 guidelines. The results obtained are as follows:
    i. Comparison of MBDT strains with average DIC strains over the mid-portion covering the gauge length (L_0 = 33 mm) resulted in a Mean Absolute Error (MAE) of 0.6% and a Root of Mean Square Error (RMSE) of 0.7%.
    ii. When comparing MBDT strains with strains obtained from the Crosshead Displacement technique, the MAE and RMSE were found to be 2.4% and 2.5%, respectively.

iii. When testing smooth geomembrane samples, MBDT strains show negligible differences compared to either DIC or Crosshead Displacement strains.
iv. MBDT strains were compatible with DIC strains for one-sided textured geomembrane samples, while the Crosshead Displacement technique yielded higher strains than the other two techniques.
v. It is important to note that the comparison was conducted up to yielding (approximately 10% strain) due to marker disruptions occurring after that. Negligible differences were observed between MBDT and DIC techniques when measuring small strains up to yielding. This highlights the computational advantage of MBDT over DIC, as it offers a more straightforward approach. However, DIC allows for the determination of continuous strains across the specimen, providing a more precise understanding of strain distribution.

Overall, the results indicate that MBDT shows good accuracy for strain measurement in testing geomembranes, particularly for small strains up to yielding.

5.2.2 Geotextile Tests

- Following the guidelines of ISO 10319, 12 tests were carried out on non-woven geotextile samples with varying masses per unit area, including (i) 300 g/m^2, (ii) 400 g/m^2, and (iii) 600 g/m^2, at two different test speeds, (a) 10 mm/min and (b) 20 mm/min. The results can be summarized as follows:
    i. Comparison of MBDT strains with average DIC strains over the mid-portion covering the gauge length (L_0 = 60 mm) resulted in a MAE of 13.0% and RMSE of 16.8%.
    ii. When comparing MBDT strains with DIC Displacement-Derived strains, considering the gauge length (L_0 = 60 mm), the MAE and RMSE were found to be 1.9% and 2.3%, respectively.

iii. When comparing MBDT strains with strains obtained from the Crosshead Displacement technique, considering a nominal gauge length (L_0 = 100 mm), the MAE and RMSE were calculated as 7.2% and 9.6%, respectively.

iv. MBDT and DIC Displacement-Derived techniques yielded almost identical strains over time, while DIC and Crosshead Displacement techniques produced higher strains. Regardless of the test speed, each technique reached similar ultimate strain values.

v. When testing a denser geotextile with a mass per unit area of 600 g/m^2, significant slippage was observed within the mechanical wedge grips, leading to the premature termination of tests. To overcome the slippage issue and accurately determine the ultimate tensile strength of the tested geotextile samples, the wedge grips may be replaced with hydraulic or roller grips. The slippage caused non-uniform elongation of the specimen within its gauge length. Consequently, MBDT and DIC Displacement-Derived techniques yielded lower strain values for the same load, resulting in steeper load-strain slopes than those obtained from Crosshead Displacement and DIC techniques.

vi. For a less dense geotextile with a mass per unit area of 300 g/m^2, MBDT and DIC Displacement-Derived techniques produced strains very close to each other, which were lower than those calculated by DIC. The Crosshead Displacement technique followed DIC.

vii. When comparing MBDT and DIC techniques for the tested geotextile samples, it was observed that DIC calculated notably higher strains. This difference can be attributed to the ductile nature of geotextiles, causing local strains in certain areas influenced by their material structure. Considering this, DIC can be preferred when a continuous strain field needs to be quantified. On the other hand, MBDT can be preferred for a more straightforward computational solution by approximating a uniform strain distribution within the gauge length.

In this case, the strain at the maximum load would be lower, and the load-strain curve would have a steeper slope.

Overall, the results indicate that both MBDT and DIC approaches can be employed depending on the specific needs such as ease of computation or precision.

5.2.3 GCL Tests

- In order to investigate the applicability of MBDT in testing GCLs, 12 tests were conducted on GCL samples cut in two directions: (i) machine direction and (ii) cross-machine direction. Two different test speeds were employed: (a) 10 mm/min and (b) 20 mm/min, following the guidelines of ISO 10319. The results can be summarized as follows:
    i. When comparing MBDT strains with average DIC strains over the mid-portion covering the gauge length (L_0=60 mm), the MAE and RMSE values were calculated as 0.4% and 0.5%, respectively.
    ii. When comparing MBDT strains with DIC Displacement-Derived strains, considering the gauge length (L_0=60 mm), the MAE and RMSE were both calculated as 0.4%.
    iii. When comparing MBDT strains with strains obtained from the Crosshead Displacement technique, considering a nominal gauge length (L_0=100 mm), the MAE and RMSE were found to be 0.7%.
    iv. It was observed that the samples cut in the machine direction exhibited higher strain capacity than those cut in the cross-machine direction. However, when the specimens having the same cut direction ruptured at similar loads and strains, regardless of the test speed.
    v. The Crosshead Displacement technique calculated slightly higher strains than the image-based techniques, namely MBDT, DIC, and DIC Displacement-Derived. However, the differences observed among the image-based techniques were not substantially different.

vi. It is important to note that the strain capacity of the tested GCL samples was approximately 15%. Strain differences were negligible when comparing MBDT and DIC techniques for the GCL specimens within this relatively small strain range. This finding highlights the computational advantage of MBDT over DIC, as also observed with geomembranes. MBDT provides a more straightforward approach in terms of computations. However, DIC enables the determination of continuous strains across the specimen, offering a more precise understanding of strain distribution.

Overall, the findings show that, in comparison to DIC and Crosshead Displacement techniques, MBDT is applicable for testing GCLs and provides accurate strain values.

5.3 Conclusions

The general conclusions obtained from this study are listed below:

- When comparing the applicability of MBDT and DIC in geosynthetics testing, it is evident that both techniques involve similar specimen preparation and video recording steps. As shown in the tests carried out for this study, both techniques can be used concurrently in the same test, enabling a direct comparison of the results.
- MBDT and DIC techniques are sensitive to lighting conditions, and it is essential to ensure adequate illumination throughout the testing process for accurate measurements. Edge detection-based segmentation failed in tests that did not employ an external light source, such as LED lights, even though color-based segmentation was moderately successful in these tests. Image segmentation was also reported to be difficult to conduct in general. Marker identification is made easier by proper lighting, which also improves image quality.

- It is important to note that both MBDT and DIC techniques rely on image-based measurements, making them suitable for non-contact strain analysis in geosynthetics testing. The choice between the two techniques depends on the specific requirements of the test, the level of strain analysis needed, and the computational resources available. DIC offers more precise strain results, as the technique calculates strains on a test specimen's whole region of interest. With that, the accuracy of this technique relies on several parameters, such as the subset spacing, strain radius, correlation coefficient cutoff value, etc. Selection of these parameters may require particular expertise to get correct results.
- On the contrary, MBDT calculates strains by measuring the displacement between two marker points that define the gauge length of the specimen, which may result in slightly less precise strain measurements than DIC. However, the advantage of MBDT lies in its straightforward application, as it does not require extensive computational parameters that could impact the accuracy of the obtained strains. In practical terms, MBDT can serve as a simpler yet effective alternative to DIC.
- The camera calibration routine implemented in Python using the OpenCV library provided accurate camera intrinsic parameters and lens distortion coefficients. The results were compared with MATLAB Camera Calibrator App and found to be consistent. The calibration routine was effective for different camera types.
- Image processing techniques were applied to correct lens distortions and track the positions of color markers on the geosynthetic samples. Different marking techniques were tested, and using a color board marker on top of a white paint marker for geomembranes and just a color board marker for geotextiles yielded the best results. Colors with distinct hues and high saturation were chosen for marking the specimens. Proper illumination using LED sources was critical for accurate color thresholding in the HSV color model.

These findings demonstrate how the MBDT technique has been successfully applied using computer vision principles and open-source software solutions. The study confirmed the technique's applicability for strain measurement in various geosynthetic materials and validated the accuracy of the technique through comparisons with known techniques.

5.4 Future Work

The study effectively applied computer vision principles and investigated the use of images for geosynthetic strain monitoring utilizing free and open-source software tools. After developing the MBDT technique, its accuracy was tested using various geosynthetic types in tensile tests. The following are the main conclusions and recommendations for further research:

- *Real-time strain acquisition:* Currently, the MBDT technique requires simultaneous initiation of the UTM and camera, which hinders real-time strain measurement. Future research could focus on enabling real-time strain acquisition without this requirement.
- *Optimal image selection:* Instead of processing every frame, exploring methods to select a representative subset of images for strain calculation would enhance the efficiency and precision of the technique.
- *Automated parameter determination:* Developing algorithms or approaches to automatically determine parameters such as millimeters-to-pixels ratio, HSV color thresholds, and marker location limits would improve the user experience and streamline the implementation of the MBDT technique.
- *Advanced image segmentation techniques:* Investigating advanced edge detection techniques, including deep learning-based methods, could enhance the image segmentation process of MBDT and compare their performance with existing algorithms such as Canny edge detection.
- *Investigation of other geosynthetic types:* Extending the application of the MBDT technique to geosynthetics beyond geomembranes and geotextiles,

such as geonets, geogrids, and geocomposites, would provide insights into the strain measurement of these materials.

- *Optimal camera type and lens configuration:* Researching the most suitable camera types and lens configurations for accurate and reliable strain measurement using the MBDT technique would help identify the optimal equipment setup.

By addressing these research areas, further advancements can be made in geosynthetic strain measurement using image-based techniques.

REFERENCES

Adamo, F., Andria, G., Bottiglieri, O., Cotecchia, F., Di Nisio, A., Miccoli, D., Sollecito, F., Spadavecchia, M., Todaro, F., & Trotta, A. (2018). GeoLab, a measurement system for the geotechnical characterization of polluted submarine sediments. *Measurement*, *127*, 335–347.

Albostan, U., & Kurç, Ö. (2016). Application of 2D digital image correlation: Three points flexure test of reinforced concrete beam. *12th International Congress on Advances in Civil Engineering. Istanbul*.

ASTM Standard D4595. (2017). *Standard Test Method for Tensile Properties of Geotextiles by the Wide-Width Strip Method*. https://doi.org/10.1520/D4595-17

ASTM Standard D638. (2014). *Standard Test Method for Tensile Properties of Plastics*. https://doi.org/10.1520/D0638-14

ASTM Standard D6637. (2015). *Standard Test Method for Determining Tensile Properties of Geogrids by the Single or Multi-Rib Tensile Method*. https://doi.org/10.1520/D6637-11

ASTM Standard D6693. (2015). *Standard Test Method for Determining Tensile Properties of Nonreinforced Polyethylene and Nonreinforced Flexible Polypropylene Geomembranes*. https://doi.org/10.1520/D6693_D6693M-20

Aydilek, A. H., Guler, M., & Edil, T. B. (2004). Use of image analysis in determination of strain distribution during geosynthetic tensile testing. *Journal of Computing in Civil Engineering*, *18*(1), 65–74.

Baldner, F. de O., Costa, P. B., Gomes, J. F. S., & Leta, F. R. (2020). A review on computer vision applied to mechanical tests in search for better accuracy. *Advances in Visualization and Optimization Techniques for Multidisciplinary Research: Trends in Modelling and Simulations for Engineering Applications*, 265–281.

Belloni, V., Ravanelli, R., Nascetti, A., Di Rita, M., Mattei, D., & Crespi, M. (2018). Digital image correlation from commercial to fos software: A mature technique for full-field displacement measurements. *International Archives of the Photogrammetry, Remote Sensing & Spatial Information Sciences*, *42*(2).

Blaber, J, Adair, B., & Antoniou, A. (2015). Ncorr: Open-Source 2D Digital Image Correlation Matlab Software. *Experimental Mechanics*, *55*(6), 1105–1122. https://doi.org/10.1007/s11340-015-0009-1

Blaber, Justin, & Antoniou, A. (2017). *Ncorr Instruction Manual*. http://www.ncorr.com/download/ncorrmanual_v1_2_2.pdf

Bradski, G. (2000). The openCV library. *Dr. Dobb's Journal: Software Tools for the*

Professional Programmer, *25*(11), 120–123. https://www.elibrary.ru/item.asp?id=4934581

Bradski, G., & Kaehler, A. (2008). *Learning OpenCV*. O'Reilly Media, Inc. https://books.google.com.tr/books?hl=tr&lr=&id=seAgiOfu2EIC&oi=fnd&pg=PR3&dq=learning+opencv&ots=hVL05icFSa&sig=ejZuEZVe1R6LNFWJ0AW0Ot2liRo&redir_esc=y#v=onepage&q=learning opencv&f=false

Castleman, K. R. (1996). *Digital Image Processing*. Prentice Hall Press.

Correlated Solutions Inc. (2021). *Speckle Pattern Fundamentals*. https://correlated.kayako.com/article/38-speckle-pattern-fundamentals

Diez, J. M. (2010). *Thermoviscoplasticity of Glassy Polymers: Experimental Characterization, Parameter Identification and Model Validation*. Universitat Stuttgart.

e Silva, R. A., Negri, R. G., & de Mattos Vidal, D. (2019). A new image-based technique for measuring pore size distribution of nonwoven geotextiles. *Geosynthetics International*, *26*(3), 261–272.

Eichhorn, G. N., Bowman, A., Haigh, S. K., & Stanier, S. (2020). Low-cost digital image correlation and strain measurement for geotechnical applications. *Strain*, *56*(6), e12348.

Ferreira, J. A. Z., & Zornberg, J. G. (2015). A transparent pullout testing device for 3D evaluation of soil–geogrid interaction. *Geotechnical Testing Journal*, *38*(5), 686–707.

Giroud, J. P. (2005). Quantification of geosynthetic behavior. *Geosynthetics International*, *12*(1), 2–27.

Gonzalez, R. C., & Woods, R. E. (2002). *Digital Image Processing*.

Guler, M., Edil, T. B., & Bosscher, P. J. (1999). Measurement of Particle Movement in Granular Soils Using Image Analysis. *Journal of Computing in Civil Engineering*, *13*(2), 116–122. https://doi.org/10.1061/(ASCE)0887-3801(1999)13:2(116)

Hryciw, R. D., & Raschke, S. A. (1996). Development of computer vision technique for in situ soil characterization. *Transportation Research Record*, *1526*(1), 86–97.

Huang, T. (1996). *Computer vision: Evolution and promise*.

Ikehata, K., & Liu, Y. (2011). *Land Disposal of Wastes* (J. O. B. T.-E. of E. H. Nriagu (ed.); pp. 353–361). Elsevier. https://doi.org/https://doi.org/10.1016/B978-0-444-52272-6.00521-3

ISO Standard 10319. (2015). *Geosynthetics — Wide-width tensile test*. https://www.iso.org/standard/57696.html

ISO Standard 527-3. (2018). *Plastics — Determination of tensile properties — Part 3: Test conditions for films and sheets*. https://www.iso.org/standard/70307.html

Jayalath, C. P. G., & Wimalasena, K. D. (2020). Measuring strains on geogrid specimens under the laboratory tensile test. *GEOMATE Journal*, *18*(65), 86–93.

Jones, D. (2000). *Wide-width geotextile testing with video extensometry* (Issue STP 1379).

Kaklamanos, J. (2016). geotech: Development of Geotechnical Engineering Software Package in R. *USUCGER Board of Directors*.

Kim, D., & Frost, J. D. (2007). Investigation of filament distribution at geotextile/geomembrane interfaces. *Geosynthetics International*, *14*(3), 128–140.

Koerner, R. (2005). *Designing with Geosynthetics* (5th ed.). Pearson Prentice Hall.

Laraba-Abbes, F., Ienny, P., & Piques, R. (2003). A new 'tailor-made'methodology for the mechanical behaviour analysis of rubber-like materials: I. Kinematics measurements using a digital speckle extensometry. *Polymer*, *44*(3), 807–820.

Lenarduzzi, V., Taibi, D., Tosi, D., Lavazza, L., & Morasca, S. (2020). Open source software evaluation, selection, and adoption: a systematic literature review. *2020 46th Euromicro Conference on Software Engineering and Advanced Applications (SEAA)*, 437–444.

Leshchinsky, D., & Fowler, J. (1990). Laboratory measurement of load-elongation relationship of high-strength geotextiles. *Geotextiles and Geomembranes*, *9*(2), 145–164. https://doi.org/https://doi.org/10.1016/0266-1144(90)90011-Z

Li, S., Zhou, W.-H., Jing, X.-Y., & Zhu, H.-X. (2018). Evaluation of grain shape parameters of Fujian standard sand. *Proceedings of China-Europe Conference on Geotechnical Engineering: Volume 1*, 186–190.

Lomov, S. V, Boisse, P., Deluycker, E., Morestin, F., Vanclooster, K., Vandepitte, D., Verpoest, I., & Willems, A. (2008). Full-field strain measurements in textile deformability studies. *Composites Part A: Applied Science and Manufacturing*, *39*(8), 1232–1244.

M Madrigal, G. A., L Beltran, A., F Diaz, S. P. A., F Galos, R. R., H Roca, J. K., V Santos, C. A., M Amado, T., M Arago, N., Quijano, J. F., & Fernandez, E. (2021). USoil: Development of USCS-Based Soil Classifier Using Digital Image Processing and Convolutional Neural Network. *International Journal of Computing and Digital System*, 93–107.

Marx, D., Kumar, K., & Zornberg, J. (2022). Evaluation of particle motions in stabilized specimens of transparent sand using deep learning segmentation.

ArXiv Preprint ArXiv:2212.02939.

McCormick, N., & Lord, J. (2010). Digital image correlation. *Materials Today*, *13*(12), 52–54.

Mishra, S. R., Mohapatra, S. R., Sudarsanan, N., Rajagopal, K., & Robinson, R. G. (2017). A simple image-based deformation measurement technique in tensile testing of geotextiles. *Geosynthetics International*, *24*(3), 306–320.

Müller, W. W., & Saathoff, F. (2015). Geosynthetics in geoenvironmental engineering. *Science and Technology of Advanced Materials*, *16*(3), 34605. https://doi.org/10.1088/1468-6996/16/3/034605

Parsons, E., Boyce, M. C., & Parks, D. M. (2004). An experimental investigation of the large-strain tensile behavior of neat and rubber-toughened polycarbonate. *Polymer*, *45*(8), 2665–2684.

Parsons, E. M., Boyce, M. C., Parks, D. M., & Weinberg, M. (2005). Three-dimensional large-strain tensile deformation of neat and calcium carbonate-filled high-density polyethylene. *Polymer*, *46*(7), 2257–2265.

Peng, X., & Zornberg, J. G. (2019). Evaluation of soil-geogrid interaction using transparent soil with laser illumination. *Geosynthetics International*, *26*(2), 206–221.

Poggiogalle, T. M., Meehan, C. L., Clarke-Sather, A. R., & Talebi, M. (2022). A Digital Image Analysis Technique for Improved Strain Measurement in Geosynthetic Tensile Testing. *Geotechnical Testing Journal*, *45*(3).

Qu, S. (2007). *Temperature–Dependent Finite Viscoplasticity of Glassy Polymers: Experiments and Simulations*. Universitat Stuttgart.

Rowe, K. (2020). Protecting the Environment with Geosynthetics: 53rd Karl Terzaghi Lecture. *Journal of Geotechnical and Geoenvironmental Engineering*, *146*(9), 4020081. https://doi.org/10.1061/(ASCE)GT.1943-5606.0002239

Rowe, R. K., & Yu, Y. (2019). Magnitude and significance of tensile strains in geomembrane landfill liners. *Geotextiles and Geomembranes*, *47*(3), 439–458.

Skochdopole, T. R., Cassady, L., Pihs, D., & Stevenson, P. E. (2000). *Comparative Study of Roller and Wedge Grips for Tensile Testing of High Strength Fabrics with Laser Extensometry: Comparisons to LVDT and Crosshead Extension*.

Stanier, S. A., Blaber, J., Take, W. A., & White, D. J. (2015). Improved image-based deformation measurement for geotechnical applications. *Canadian Geotechnical Journal*, *53*(5), 727–739. https://doi.org/10.1139/cgj-2015-0253

Tang, X.-W., Tang, L., She, W., & Gao, B.-S. (2013). Prediction of pore size characteristics of woven slit-film geotextiles subjected to tensile strains. *Geotextiles and Geomembranes*, *38*, 43–50.

Termonia, Y., & Smith, P. (1987). Kinetic model for tensile deformation of polymers. *Macromolecules*, *20*(4), 835–838.

The MathWorks Inc. (2023). *Computer Vision Toolbox*. mathworks.com

Thomas, H., & Cantré, S. (2009). Applications of low-budget photogrammetry in the geotechnical laboratory. *The Photogrammetric Record*, *24*(128), 332–350.

Thorr, F., Drean, J. Y., & Adolphe, D. (1999). Image analysis tools to study nonwovens. *Textile Research Journal*, *69*(3), 162–168.

Uy, E. E. S., & Boonyatee, T. (2016). Image processing for geotechnical laboratory measurements. *GEOMATE Journal*, *10*(22), 1964–1970.

Vangla, P., & Gali, M. L. (2014). Image-segmentation technique to analyze deformation profiles in different direct shear tests. *Geotechnical Testing Journal*, *37*(5), 828–839.

Wiley, V., & Lucas, T. (2018). Computer vision and image processing: a paper review. *International Journal of Artificial Intelligence Research*, *2*(1), 29–36.

Xia, X., Zhang, X., & Mu, C. (2021). A multi-camera based photogrammetric method for three-dimensional full-field displacement measurements of geosynthetics during tensile test. *Geotextiles and Geomembranes*, *49*(5), 1192–1210.

Zangl, F., & Likos, W. J. (2016). Alternative methods for wet-dry cycling of geosynthetic clay liners. *Journal of Geotechnical and Geoenvironmental Engineering*, *142*(11), 4016063.

Zhang, Z. (2000). A flexible new technique for camera calibration. *IEEE Transactions on Pattern Analysis and Machine Intelligence*, *22*(11), 1330–1334. https://doi.org/10.1109/34.888718

Zhao, Y. J., Wang, Y. X., He, G., & Zhao, H. H. (2013). A New Image-Based Soil Deformation Measurement System. *Advanced Materials Research*, *629*, 488–492.

Zhu, D., Mobasher, B., & Rajan, S. D. (2012). Non-contacting strain measurement for cement-based composites in dynamic tensile testing. *Cement and Concrete Composites*, *34*(2), 147–155.

Zornberg, J. G., & Arriaga, F. (2003). Strain distribution within geosynthetic-reinforced slopes. *Journal of Geotechnical and Geoenvironmental Engineering*, *129*(1), 32–45.

Zornberg, J. G., & Gupta, R. (2010). Geosynthetics in pavements: North American contributions. *Theme Speaker Lecture, Proceedings of the 9th International Conference on Geosynthetics, Guarujá, Brazil, May*, *1*, 379–400.

APPENDICES

A. Geomembrane Tests

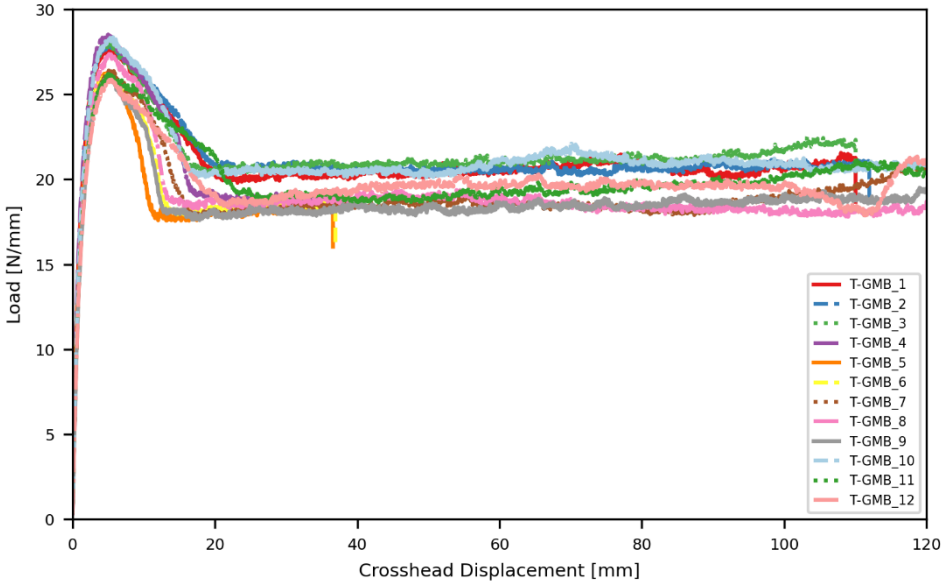

Figure 6.1. Load - Crosshead Displacement plot of the geomembrane tests.

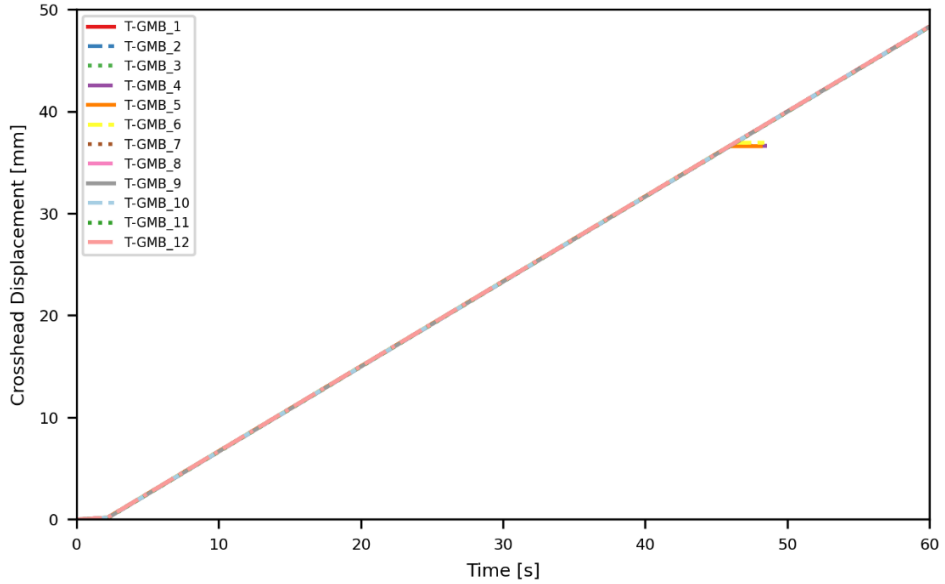

Figure 6.2. Crosshead Displacement - Time plot of the geomembrane tests.

B. Geotextile Tests

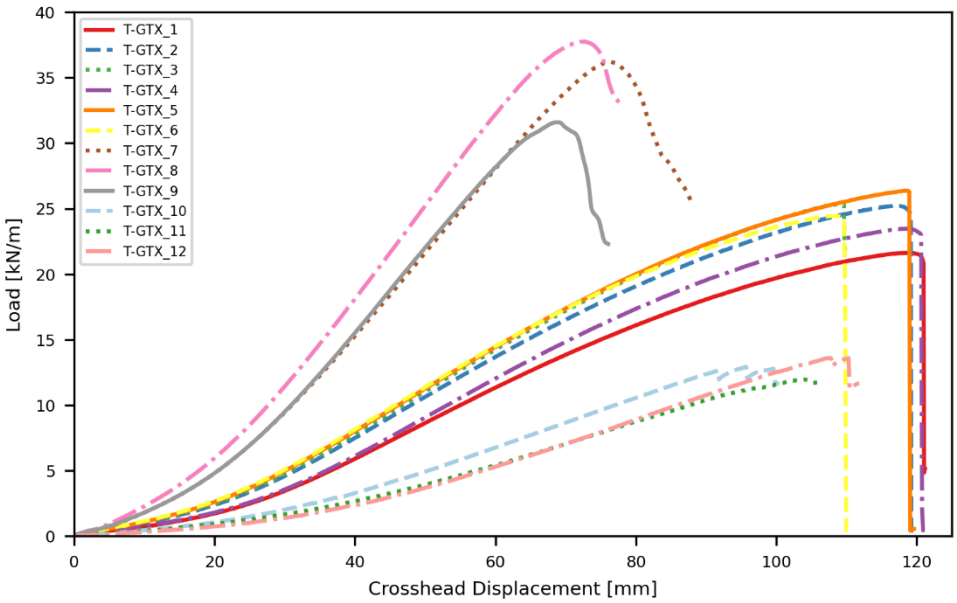

Figure 6.3. Load - Crosshead Displacement plot of the geotextile tests.

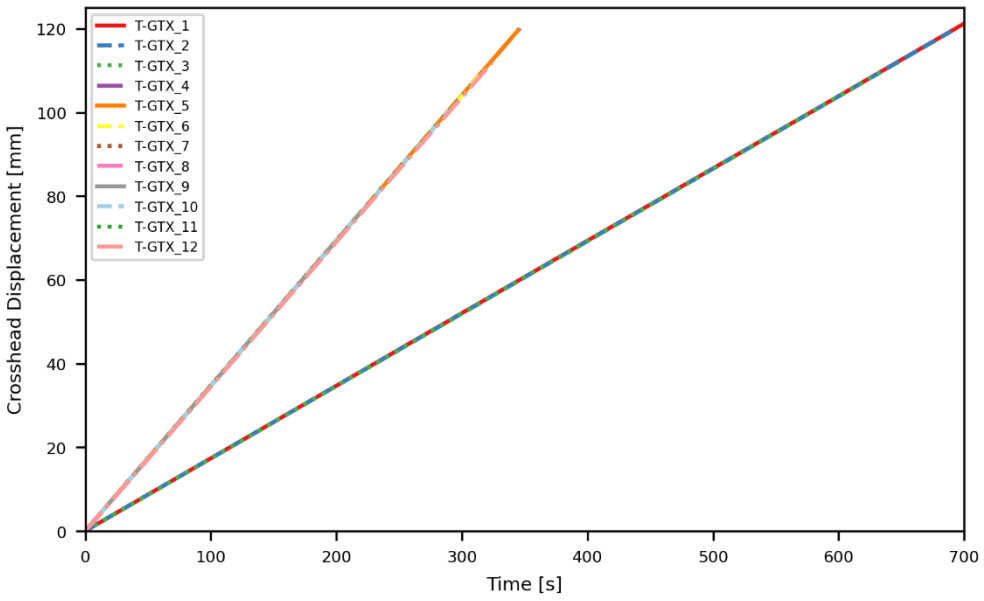

Figure 6.4. Crosshead Displacement - Time plot of the geotextile tests.

C. GCL Tests

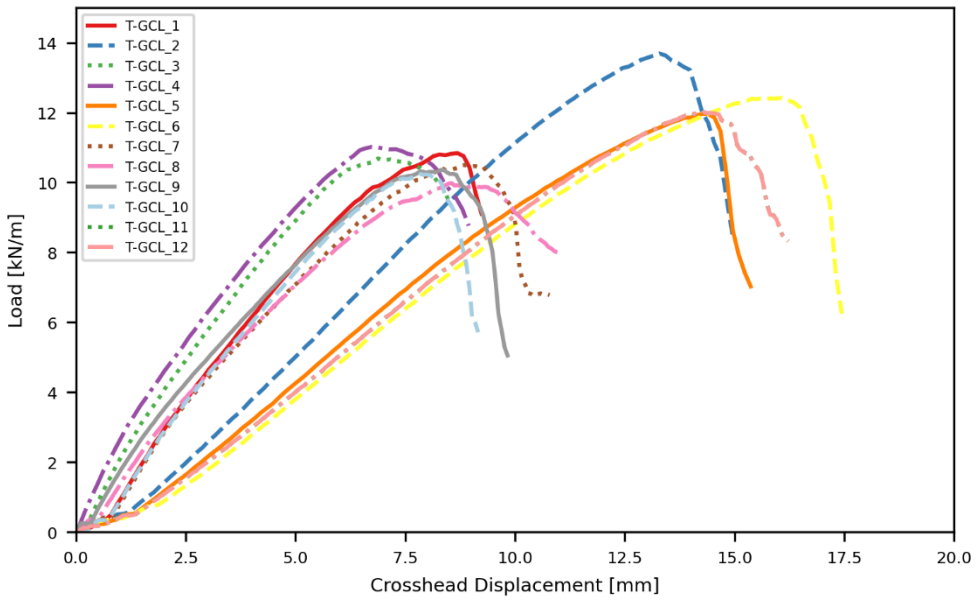

Figure 6.5. Load - Crosshead Displacement plot of the GCL tests.

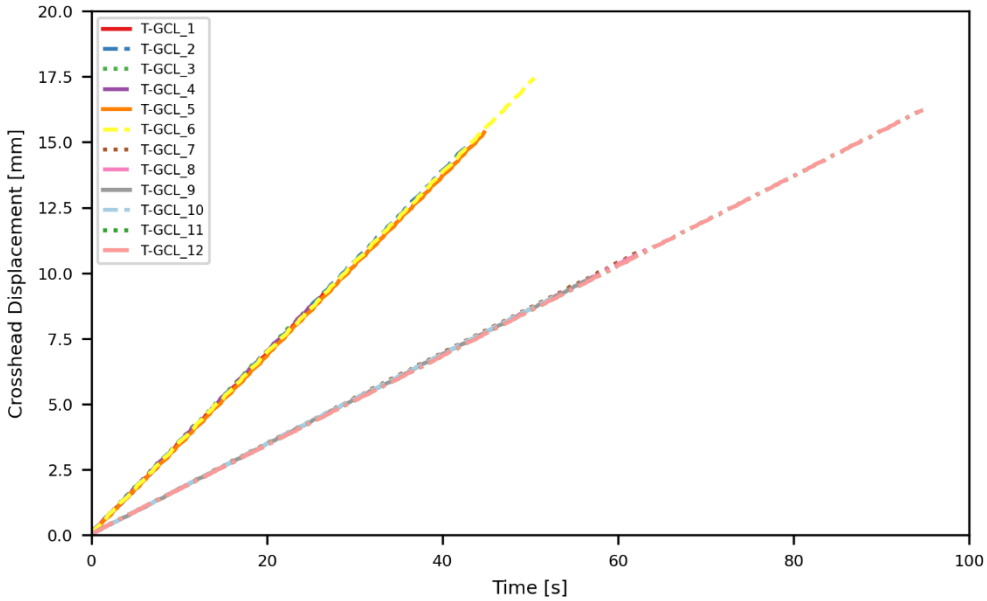

Figure 6.6. Crosshead Displacement - Time plot of the GCL tests.